UiO : University of Oslo

Christian Pedersen

Elastohydrodynamic and capillary thin film flows at small scales

Thesis submitted for the degree of Philosophiae Doctor

Department of Mathematics
The Faculty of Mathematics and Natural Sciences

2021

Series of dissertations submitted to the
Faculty of Mathematics and Natural Sciences, University of Oslo
No. 2439

ISSN 1501-7710

Cover: Hanne Baadsgaard Utigard.
Print production: Reprosentralen, University of Oslo.

Preface

This thesis is submitted in partial fulfillment of the requirements for the degree of *Philosophiae Doctor* at the University of Oslo. The research presented here was conducted at the University of Oslo and at the University of Bordeaux, under the supervision of Professor Andreas Carlson, Associate Professor Thomas Salez, Dr. Tak Shing Chan and Professor Kent-Andre Mardal.

The thesis is a collection of six articles, presented in practical order. The main theme of these articles is the mathematical modelling of interface dynamics in small scale systems. The articles are preceded by six chapters that provide relevant background information, motivation for the work and a perspective on future directions.

Christian Pedersen
Oslo, September 2021

Acknowledgements

First and foremost I would like to thank my main supervisor Andreas Carlson for giving me this opportunity and who has provided guidance through my doctoral studies. I would also like to thank my co-supervisor Thomas Salez for inviting me to the University of Bordeaux and for always offering a helping hand and providing me with new projects to work on. Also, thanks for the surfing lessons! My sincerest gratitude goes to my co-supervisors Tak Shing Chan and Kent-Andre Mardal for helpful and fruitful discussions and great collaborations. Furthermore I would like to thank all my excellent colleagues at the Mechanics Section, both present and former, for making these 4 years very enjoyable. A special thanks goes to Miroslav Kuchta who has helped me whenever needed, both at work and in the ski slopes. Also, a big thank you goes to Mathijs Janssen for your valuable feedback on my thesis and for always having time for a cup of coffee. I would also like to thank our lab engineer Olav Gundersen and our excellent IT staff Terje Kvernes and Lucy Karpen.

Last but most importantly, I want to thank Kristine and Albert for their unconditional love and support and for making my life as much fun as it is!

Christian Pedersen
Oslo, September 2021

List of Papers

Paper I

Pedersen, C. and Niven, J. F. and Salez, T. and Dalnoki-Veress, K. and Carlson, A. "Asymptotic regimes in elastohydrodynamic and stochastic leveling on a viscous film". In: *Physical Review Fluids*, (2019), DOI: 10.1103/PhysRevFluids.4.124003.

Paper II

Pedersen, C., Salez, T., Carlson, A. "Universal Self-Similar Attractor in the Bending-Driven Leveling of Thin Viscous Films". In review at *Proceedings of the Royal Society A*, Available at *Arxiv*: 2011.10297.

Paper III

Ren, S., Pedersen, C., Carlson, A., Salez, T., Wang, Y. "Capillary deformation of ultrathin glassy polymer films by air nanobubbles". In: *Physical Review Research*, (2020), DOI: 10.1103/PhysRevResearch.2.043166.

Paper IV

Pedersen, C., Ren, S., Wang, Y., Carlson, A., Salez, T. "Nanobubble-induced flow of immersed glassy polymer films". In review at *Physical Review Fluids*, Available at *Arxiv*: 2104.02948.

Paper V

Chan, T. S., Pedersen, C., Koplik, J., Carlson, A. "Film deposition and dynamics of a self-propelled wetting droplet on a conical fibre". In: *Journal of Fluid Mechanics*, (2020), DOI: 10.1017/jfm.2020.834.

Paper VI

Chan, T. S., Lee, C. L., Pedersen, C., Dalnoki-Veress, K., Carlson, A. "Film coating by directional droplet spreading on fibers". In: *Physical Review Fluids*, (2021), DOI: 10.1103/PhysRevFluids.6.014004.

Contents

List of Figures

Chapter 1

Introduction

Thin viscous films have been of great interest to mankind for centuries with a notable early application related to the invention of the wheel and axle and its need for lubricating films [1]. Although frequently used in everyday applications, it was not until the experiments of Tower [2] and the subsequent analytical treatment by Reynolds [3] in 1886 that an understanding of the dynamic properties of thin films arose. Its ability to reduce friction forces between moving objects and to reduce wear on a supporting substrate has made thin films indispensable in modern industrial applications through lubrication, coating and paints [4, 5, 6] and more recently in semiconductors [7] and soft robotics [8]. Although our understanding of thin film dynamics is historically rather new, Nature is notoriously known to exploit the properties of thin films. Notable examples being water harvest through capillary rise [9] and the formation of laccoliths from magmatic intrusion in the earths crust [10, 11]. Also in human biology we find thin films that serve many purposes through lubrication of joints by articular cartilage [12], peristaltic flow in arteries [13] and around the brain [14] and for cleaning purposes such as the lacrimal fluid that covers the human eye [15]. See figure 1.1 for examples.

At the core of thin film dynamics lies the coupling between the viscous forces in the fluid and the forces acting on its interfaces. A general theoretical description of thin film dynamics can therefore be found by solving the Navier-Stokes equations in the bulk using boundary conditions at the film interfaces. A solution to a given problem can then be found by direct numerical simulations [16]. However, a characteristic feature of thin film systems is that they have one length scale that is significantly smaller than the others, thereof the name *thin* film. By utilizing this scale separation we can find a leading order theoretical description of the film dynamics within the framework of lubrication theory [4, 6, 17, 18]. By combining the leading order velocity profile solution with conservation of mass, this approximation yields a scalar evolution equation for the spatiotemporal evolution of the film thickness which is more amenable to traditional mathematical analysis. A particular type of thin film problems to which lubrication theory has been successfully applied is the one of spreading of a viscous fluid on top of a solid substrate. For a completely wetting fluid [19] at scales below the capillary length [17] this process is driven by surface tension forces acting on the film interface that wants to minimize the systems free energy. This is achieved by reducing the curvature of the film profile by levelling any perturbations into a flat film of homogenous thickness. An emblematic example of this is the capillary spreading of a viscous droplet on a flat rigid substrate. From the Young-Laplace law we know that surface tension forces make the droplet adopt the shape of a spherical cap before reaching its final flat

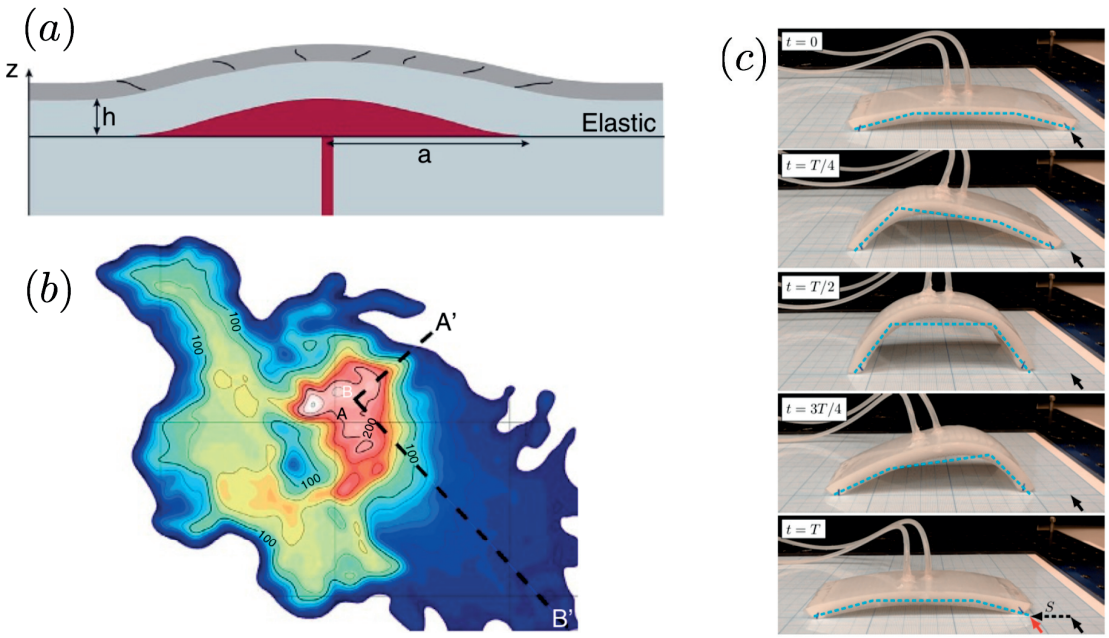

Figure 1.1: Examples of thin films found in Nature and industry. (a) Schematic of how magmatic intrusion in the earths crust bends the crust like an elastic plate and spreads underneath it. (b) Contour plot of the surface elevation after the formation of a laccolith due to magmatic intrusion. Figures (a)-(b) are adapted form [11] which is licenced under CC BY 4.0. (c) Locomotion in soft robotics is driven by pressurized fluid flow in thin interior channels inside the robot. The figure show how the robot can move in four steps. Figure adapted from [8] © 2020 IEEE.

equilibrium profile, when it is smaller than the capillary length. Experimental observations show that the radius of the spherical cap increases in time with a power-law behaviour as the droplet spreads out on the substrate [20, 21, 22]. This power-law behaviour and its exponent was found in an analysis of the thin film equation and are known as Tanner's law. This spreading law is valid for any capillary-driven spreading droplets that wets a substrate due to the existence of a thin pre-wetted layer that spreads out ahead of the droplet caused by the molecular interactions between the liquid and the solid substrate [19]. This pre-wetted layer offers an explanation to how a droplet spreading can overcome the diverging viscous stress at the contact line [20] and it is thus an important feature when modelling droplet spreading. Further experiments on droplet spreading highlighted the effect of the thickness of the pre-wetted layer on the spreading dynamics [23, 24]. The spreading dynamics transitions from the nonlinear Tanner's regime into a linear spreading regime as the ratio between the droplet height and the pre-wetted layer thickness decreases.

When capillary levelling is studied at the nanoscale, experiments are often performed using fluids of complex rheology such as polystyrene due to its favourable material properties such as a low glass transition temperature,

$T_G \approx 100°C$ [25]. Thin polymer films can then be prepared with pre-existing gradients in the interface curvature that lead to capillary driven flow when the film is heated above the glass transition temperature. Such pre-manufactured films are important tools when studying interface dynamics and the rheological properties of polymer films close to the glass transition [26, 27]. Moreover, the pre-manufacturing of surface patterns in thin films has enabled studies of many capillary flow problems that can be encountered in engineering processes such as nanopatterning [28], viscous filling of holes [29, 30] and step relaxation [31].

An elastohydrodynamic analogue to the capillary-driven droplet spreading is the spreading of a viscous fluid under an elastic plate that rests on a thin pre-wetted film [32]. When injecting additional fluid underneath the elastic plate, the spreading liquid peels the elastic plate from the pre-wetted film and causes it to bend and stretch. The coupling between the elastic interface stress and the viscous stress in the fluid bulk is given by the Föppel–von-Kármán equations [33]. Notoriously difficult to solve, these equations are therefore often simplified and the two stress contributions are considered separately [34] or with assumptions of isotropic in-plane compression [35]. However, there are recent studies that utilize the full model equations in order to study instabilities in blistering [36] such as elastic fingering in soft walled channels [37, 38, 39], see figure 1.2e-f. Under the assumption of small plate deflections the Föppel–von-Kármán plate equations are reduced to a linear bending contribution in the hydrodynamic pressure. The elastohydrodynamic analogue to Tanner's law for the spreading of the viscous liquid is in this limit found by an asymptotic matching procedure of the quasi-static bulk profile and a traveling wave solution at the peeling front [40].

Another important aspect to consider in elastohydrodynamic flow is the one of boundary conditions. A simplified one-dimensional study using isotropic in-plane tension demonstrated that spatial confinement of the elastic plate can lead to the formation of wrinkles [35]. In this scenario the wrinkle wavelength grows as a power-law with a logarithmic contribution in time until bending effects dominate the dynamics and the plate buckles. There are however reasons to assume that localized compression will effect the dynamics as shown for morphogenesis of biological materials [41].

A crucial aspect of thin films is the stability. The stability of a flat free surface thin film of uniform thickness is maintained by the capillary force that minimizes the surface area of the film, thus flattening any perturbation to the film interface. Additional mechanisms are needed to destabilize the film which can rupture by attractive van der Waals forces [42] where the interface dynamics at the point of rupture has been studied in great detail [43, 44]. By combining the effects of surface tension and van der Waals forces into a one-dimensional thin film equation, an analysis of its numerical solution found that the film thickness at the point of rupture behaves with a power law in time [45]. Further studies extended the theoretical models to axisymmetric coordinates where similarity solutions were found by an asymptotic-matching procedure, assuming a quasi-static far-field solution to the thin film profile [46, 47]. Instabilities in thin films can also lead to droplet formation [48]. This is visualized in figure 1.2a where

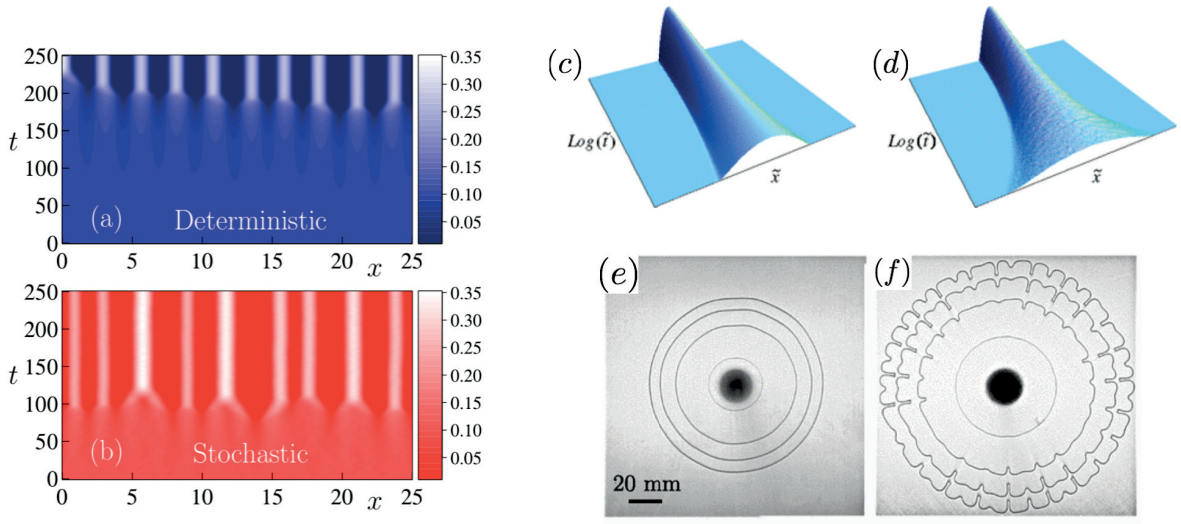

Figure 1.2: (a)-(b) Kymographic representation of the height of a thin viscous film during a de-wetting process with the y-axis representing time. Surface instabilities grow in time and lead to film rupture and the formation of droplets. (a) Deterministic de-wetting driven by van der Waals forces. After the film has ruptured, all droplets have similar size. (b) Stochastic de-wetting driven by van der Waals forces and accelerated by thermal fluctuations. The de-wetting process if much faster and the generated droplets have varying sizes. Reprinted with permission from [52] © 2015 by the American Physical Society. (c)-(d) A viscous droplet spreading on top of a thin viscous film. (c) The spreading is driven by surface tension forces which gives a smooth droplet profile. (d) The droplet spreading are influenced by thermal fluctuations to which the spreading rate is accelerated. Reprinted with permission from [53] © 2005 by the American Physical Society. (e)-(f) A lubricated elastic membrane delaminates from its supporting substrate by injecting air from underneath. (e) The flux of air that is injected is small and the spreading process is smooth. (f) When the flux of injected air is increased, fingering patterns emerge in the delamination process. Reprinted with permission from [37] © 2012 by the American Physical Society.

we see an unstable thin film that breaks up into a distribution of droplets. The rupture dynamics of thin films has also been studied for elastohydrodynamic flows [49].

Beyond the deterministic effects discussed so far there are other forces that come into play when we consider systems at the nanoscale. At these length scales thermal fluctuations can cause perturbations to a thin film that can grow in time subsequently leading to film rupture. A phenomenological model of fluctuating hydrodynamics was introduced by Landau and Lifshitz [50] by adding a stochastic stress to the flow momentum equation, which can be derived from the Boltzmann equation [51]. Thermal fluctuations can accelerate the de-wetting process by enhancing the perturbation of a thin film [54, 55]. Linear approximation of the thin film equation shows that thermal fluctuations can

change the capillary wave spectrum of the film perturbations from showing exponential decay in time to a power law [56]. As the fluctuations are random this can have great effects on the distribution of droplets during spinodal dewetting [52, 57] as illustrated in figure 1.2b. One way to stabilize the instabilites caused by fluctuations is to impose a shear flow at the film interface. This has been studied for confined flows with a liquid-liquid interface where a Couette flow is imposed. Analytical analysis and Brownian dynamics simulations show that shear can stabilize film perturbations [58, 59].

Morover, thermal fluctuations have been studied in the context of droplet spreading [53, 60]. In figure 1.2c-d the difference between the deterministic and stochastic spreading for a one-dimensional droplet is illustrated. It is clear that thermal fluctuations accelerate the rate at which the droplet spreads. A similar study has also been conducted in the stochastic elastohydrodynamic case of the levelling of a blister [61], combining numerical simulations and a scaling analysis with similar results. Besides their apparent influence on the interface dynamics it has also been shown that thermal fluctuations can enhance the bulk diffusion and transport of particles in soft nanochannels due to fluctuations of the channel walls [62, 63].

This thesis is a collection of articles that explore the dynamics of different thin film systems to which the lubrication approximation is applicable. The thesis is structured as follows; in chapter 2 we define the relevant forces acting on a thin film interface and show the derivation of the associated mathematical expressions, which are often omitted in the published literature. In chapter 3 we present the viscous flow equations, *i.e.* the Navier-Stokes equations, and utilize the lubrication approximation to obtain the thin film equations for the forces described in chapter 2. In chapter 4 we discuss the numerical methods we have used and derive the variational formulation of the thin film equations used in our finite element analysis before we summarise our article findings in chapter 5. Finally, in chapter 6 we conclude the introductory part of this thesis with a future perspective on the research.

References

[1] Anderson, K. J. “A History of Lubricants”. *MRS Bulletin* vol. 16, no. 10 (1991), pp. 69–69.

[2] Tower, B. “First report on friction experiments”. *Proceedings of the institution of mechanical engineers* vol. 34, no. 1 (1883), pp. 632–659.

[3] Reynolds, O. “IV. On the theory of lubrication and its application to Mr. Beauchamp Tower’s experiments, including an experimental determination of the viscosity of olive oil”. *Philosophical transactions of the Royal Society of London*, no. 177 (1886), pp. 157–234.

[4] Oron, A., Davis, S. H., and Bankoff, S. G. “Long-scale evolution of thin liquid films”. *Reviews of modern physics* vol. 69, no. 3 (1997), p. 931.

[5] Hamrock, B. J., Schmid, B. J., and Jacobson, B. O. *Fundamentals of fluid film lubrication*. Vol. 169. CRC press, 2004.

[6] Blossey, R. *Thin liquid films: dewetting and polymer flow*. Springer Science & Business Media, 2012.

[7] Fortunato, E., Barquinha, P., and Martins, R. "Oxide semiconductor thin-film transistors: a review of recent advances". *Advanced materials* vol. 24, no. 22 (2012), pp. 2945–2986.

[8] Gamus, B. et al. "Understanding inchworm crawling for soft-robotics". *IEEE Robotics and Automation Letters* vol. 5, no. 2 (2020), pp. 1397–1404.

[9] Jurin, J. "II. An account of some experiments shown before the Royal Society; with an enquiry into the cause of the ascent and suspension of water in capillary tubes." *Philosophical Transactions of the Royal Society of London* vol. 30, no. 355 (1718), pp. 739–747.

[10] Michaut, C. "Dynamics of magmatic intrusions in the upper crust: Theory and applications to laccoliths on Earth and the Moon". *Journal of Geophysical Research: Solid Earth* vol. 116, no. B5 (2011).

[11] Castro, J. M. et al. "Rapid laccolith intrusion driven by explosive volcanic eruption". *Nature Communications* vol. 7, no. 1 (2016), pp. 1–7.

[12] Jahn, S., Seror, J., and Klein, J. "Lubrication of articular cartilage". *Annual review of biomedical engineering* vol. 18 (2016), pp. 235–258.

[13] Takagi, D. and Balmforth, N. "Peristaltic pumping of viscous fluid in an elastic tube". *Journal of Fluid mechanics* vol. 672 (2011), p. 196.

[14] Rasmussen, M. K., Mestre, H., and Nedergaard, M. "Fluid Transport in the Brain". *Physiological Reviews* (2021).

[15] Botelho, S. Y. "Tears and the lacrimal gland". *Scientific American* vol. 211, no. 4 (1964), pp. 78–87.

[16] Pihler-Puzovic, D. et al. "Displacement flows under elastic membranes. Part 1. Experiments and direct numerical simulations". *Journal of Fluid Mechanics* vol. 784 (2015), p. 487.

[17] Batchelor, G. K. *An introduction to fluid dynamics*. Cambridge university press, 1967.

[18] Stillwagon, L. and Larson, R. "Fundamentals of topographic substrate leveling". *Journal of applied physics* vol. 63, no. 11 (1988), pp. 5251–5258.

[19] De Gennes, P.-G. "Wetting: statics and dynamics". *Reviews of modern physics* vol. 57, no. 3 (1985), p. 827.

[20] Huh, C. and Scriven, L. E. "Hydrodynamic model of steady movement of a solid/liquid/fluid contact line". *Journal of colloid and interface science* vol. 35, no. 1 (1971), pp. 85–101.

[21] Voinov, O. "Hydrodynamics of wetting". *Fluid dynamics* vol. 11, no. 5 (1976), pp. 714–721.

[22] Tanner, L. "The spreading of silicone oil drops on horizontal surfaces". *Journal of Physics D: Applied Physics* vol. 12, no. 9 (1979), p. 1473.

[23] Cormier, S. L. et al. "Beyond Tanner's law: Crossover between spreading regimes of a viscous droplet on an identical film". *Physical review letters* vol. 109, no. 15 (2012), p. 154501.

[24] Bergemann, N., Juel, A., and Heil, M. "Viscous drops on a layer of the same fluid: from sinking, wedging and spreading to their long-time evolution". *Journal of Fluid Mechanics* vol. 843 (2018), pp. 1–28.

[25] Martienssen, W. and Warlimont, H. *Springer handbook of condensed matter and materials data*. Springer Science & Business Media, 2006.

[26] Forrest, J. A. et al. "Effect of Free Surfaces on the Glass Transition Temperature of Thin Polymer Films". *Phys. Rev. Lett.* Vol. 77 (10 Sept. 1996), pp. 2002–2005.

[27] Chai, Y. et al. "A direct quantitative measure of surface mobility in a glassy polymer". *Science* vol. 343, no. 6174 (2014), pp. 994–999.

[28] Rognin, E., Landis, S., and Davoust, L. "Viscosity measurements of thin polymer films from reflow of spatially modulated nanoimprinted patterns". *Physical Review E* vol. 84, no. 4 (2011), p. 041805.

[29] Backholm, M. et al. "Capillary levelling of a cylindrical hole in a viscous film". *Soft Matter* vol. 10, no. 15 (2014), pp. 2550–2558.

[30] Bertin, V. et al. "Symmetrization of Thin Freestanding Liquid Films via a Capillary-Driven Flow". *Physical review letters* vol. 124, no. 18 (2020), p. 184502.

[31] McGraw, J. D., Jago, N. M., and Dalnoki-Veress, K. "Capillary levelling as a probe of thin film polymer rheology". *Soft Matter* vol. 7, no. 17 (2011), pp. 7832–7838.

[32] Karan, P., Chakraborty, J., and Chakraborty, S. "Small-scale flow with deformable boundaries". *Journal of the Indian Institute of Science* vol. 98, no. 2 (2018), pp. 159–183.

[33] Landau, L. D. and Lifshitz, E. M. *Course of Theoretical Physics Vol 7: Theory and Elasticity*. Pergamon Press, 1959.

[34] Peng, G. G. and Lister, J. R. "Viscous-fingering mechanisms under a peeling elastic sheet". *Journal of Fluid Mechanics* vol. 864 (2019), pp. 1177–1207.

[35] Kodio, O., Griffiths, I. M., and Vella, D. "Lubricated wrinkles: Imposed constraints affect the dynamics of wrinkle coarsening". *Physical Review Fluids* vol. 2, no. 1 (2017), p. 014202.

[36] Juel, A., Pihler-Puzović, D., and Heil, M. "Instabilities in blistering". *Annual Review of Fluid Mechanics* vol. 50 (2018), pp. 691–714.

[37] Pihler-Puzović, D. et al. "Suppression of complex fingerlike patterns at the interface between air and a viscous fluid by elastic membranes". *Physical review letters* vol. 108, no. 7 (2012), p. 074502.

[38] Pihler-Puzović, D. et al. “Viscous fingering in a radial elastic-walled Hele-Shaw cell”. *Journal of Fluid Mechanics* vol. 849 (2018), pp. 163–191.

[39] Fontana, J. V. et al. “Modelling finger propagation in elasto-rigid channels”. *Journal of Fluid Mechanics* vol. 916 (2021).

[40] Lister, J. R., Peng, G. G., and Neufeld, J. A. “Viscous control of peeling an elastic sheet by bending and pulling”. *Physical review letters* vol. 111, no. 15 (2013), p. 154501.

[41] Dervaux, J., Ciarletta, P., and Amar, M. B. “Morphogenesis of thin hyperelastic plates: a constitutive theory of biological growth in the Föppl–von Kármán limit”. *Journal of the Mechanics and Physics of Solids* vol. 57, no. 3 (2009), pp. 458–471.

[42] Israelachvili, J. N. *Intermolecular and surface forces*. Academic press, 2015.

[43] Williams, M. B. and Davis, S. H. “Nonlinear theory of film rupture”. *Journal of Colloid and Interface Science* vol. 90, no. 1 (1982), pp. 220–228.

[44] Craster, R. V. and Matar, O. K. “Dynamics and stability of thin liquid films”. *Reviews of modern physics* vol. 81, no. 3 (2009), p. 1131.

[45] Ida, M. P. and Miksis, M. J. “Thin film rupture”. *Applied Mathematics Letters* vol. 9, no. 3 (1996), pp. 35–40.

[46] Zhang, W. W. and Lister, J. R. “Similarity solutions for van der Waals rupture of a thin film on a solid substrate”. *Physics of Fluids* vol. 11, no. 9 (1999), pp. 2454–2462.

[47] Witelski, T. P. and Bernoff, A. J. “Stability of self-similar solutions for van der Waals driven thin film rupture”. *Physics of Fluids* vol. 11, no. 9 (1999), pp. 2443–2445.

[48] Xie, R. et al. “Spinodal dewetting of thin polymer films”. *Physical Review Letters* vol. 81, no. 6 (1998), p. 1251.

[49] Carlson, A. and Mahadevan, L. “Similarity and singularity in adhesive elastohydrodynamic touchdown”. *Physics of Fluids* vol. 28, no. 1 (2016), p. 011702.

[50] Landau, L. D. and Lifshitz, E. M. *Course of theoretical physics*. Elsevier, 2013.

[51] Mashiyama, K. T. and Mori, H. “Origin of the Landau-Lifshitz hydrodynamic fluctuations in nonequilibrium systems and a new method for reducing the Boltzmann equation”. *Journal of Statistical Physics* vol. 18, no. 4 (1978), pp. 385–407.

[52] Nesic, S. et al. “Fully nonlinear dynamics of stochastic thin-film dewetting”. *Physical Review E* vol. 92, no. 6 (2015), p. 061002.

[53] Davidovitch, B., Moro, E., and Stone, H. A. “Spreading of viscous fluid drops on a solid substrate assisted by thermal fluctuations”. *Physical review letters* vol. 95, no. 24 (2005), p. 244505.

[54] Grün, G., Mecke, K., and Rauscher, M. "Thin-film flow influenced by thermal noise". *Journal of Statistical Physics* vol. 122, no. 6 (2006), pp. 1261–1291.

[55] Durán-Olivencia, M. A. et al. "Instability, rupture and fluctuations in thin liquid films: Theory and computations". *Journal of statistical physics* vol. 174, no. 3 (2019), pp. 579–604.

[56] Mecke, K. and Rauscher, M. "On thermal fluctuations in thin film flow". *Journal of Physics: Condensed Matter* vol. 17, no. 45 (2005), S3515.

[57] Hennequin, Y. et al. "Drop formation by thermal fluctuations at an ultralow surface tension". *Physical review letters* vol. 97, no. 24 (2006), p. 244502.

[58] Thiébaud, M. and Bickel, T. "Nonequilibrium fluctuations of an interface under shear". *Physical Review E* vol. 81, no. 3 (2010), p. 031602.

[59] Thiébaud, M., Amarouchene, Y., and Bickel, T. "Nonlinear Brownian dynamics of interfacial fluctuations in a shear flow". *Journal of Statistical Mechanics: Theory and Experiment* vol. 2014, no. 12 (2014), P12011.

[60] Nesic, S. et al. "Dynamics of thin fluid films controlled by thermal fluctuations". *The European Physical Journal Special Topics* vol. 224, no. 2 (2015), pp. 379–387.

[61] Carlson, A. "Fluctuation assisted spreading of a fluid filled elastic blister". *Journal of Fluid Mechanics* vol. 846 (2018), pp. 1076–1087.

[62] Marbach, S., Dean, D. S., and Bocquet, L. "Transport and dispersion across wiggling nanopores". *Nature Physics* vol. 14, no. 11 (2018), pp. 1108–1113.

[63] Sarfati, R., Calderon, C. P., and Schwartz, D. K. "Enhanced diffusive transport in fluctuating porous media". *ACS nano* vol. 15, no. 4 (2021), pp. 7392–7398.

Chapter 2

Liquid and elastic interfaces

2.1 Surface Tension

We consider the case of a thin viscous film of height $h(x, y, t)$ in the z-direction, as depicted in figure 2.1, with x, y are the horisontal spatial coordinates and t is time. The characteristic horisontal length scale of our film is L and by a thin film we mean that $h(x, y, t)/L \ll 1$. The film shares its upper boundary with a gas of negligible viscosity compared to the viscosity of the liquid, effectively yielding zero shear at the interface. At length scales below the capillary length, $L_c = [\gamma/(\Delta\rho g)]^{1/2}$ with γ the surface tension coefficient, $\Delta\rho$ the density difference between the two phases and g the gravitational acceleration, the flow dynamics is governed by surface tension forces. The coupling between the capillary stresses at the liquid-gas interface and the hydrodynamic pressure in the fluid is given by the Young–Laplace equation [1]

$$p(x, y, t) - p_0 = \gamma\,(\nabla \cdot \mathbf{n}) \tag{2.1}$$

with p_0 the ambient pressure and $\mathbf{n}$ the normal vector to the liquid-gas interface which is given as

$$\mathbf{n} = \frac{\nabla(z - h(x, y, t))}{|\nabla(z - h(x, y, t))|}. \tag{2.2}$$

As such, and when omitting the constant ambient pressure, we can substitute Eq.(2.2) in Eq.(2.1) to express the coupling between the hydrodynamic pressure and the capillary stress as a function of the film height

$$\begin{aligned} p(x, y, t) &= \gamma(\nabla \cdot \mathbf{n}) \\ &\simeq -\gamma\nabla^2 h(x, y, t). \end{aligned} \tag{2.3}$$

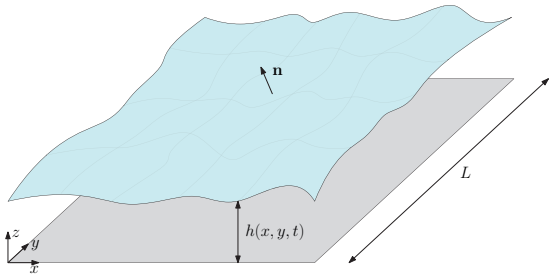

Figure 2.1: Schematic of a thin film with an interface located at $z = h(x, y, t)$, where the liquid film is supported by a rigid substrate at $z = 0$ and exposed to air at $z = h(x, y, t)$.

In the last line we have considered the small-slope approximation, *i.e.* $(\nabla h)^2 \ll 1$. Beside free surface flow, there are flows with a liquid-liquid interface where the shear stress is non-negligible. In some cases the shear stress applied to a surface can even be the main contributor to flow dynamics in a film, but we will not consider such films here. Furthermore, there are flows for which all the liquid surfaces are shared with solid materials. One such flow problem is the one encountered in elastohydrodynamics. Here, the liquid shares an interface with an elastic plate or membrane.

2.2 Elasticity

The coupling between an applied load and the deformations of a thin elastic plate is often obtained by considering the minimization of the Helmholtz free energy [2]. Here, we will show the same by considering the balance of forces and moments acting on a thin elastic plate [3, 4, 5]. We consider the infinitesimal plate element depicted in figure 2.2 that is of length Δx, width Δy and thickness d. In figure 2.2(a) we plot the resultant in-plane forces T_{ij}, out-of-plane forces

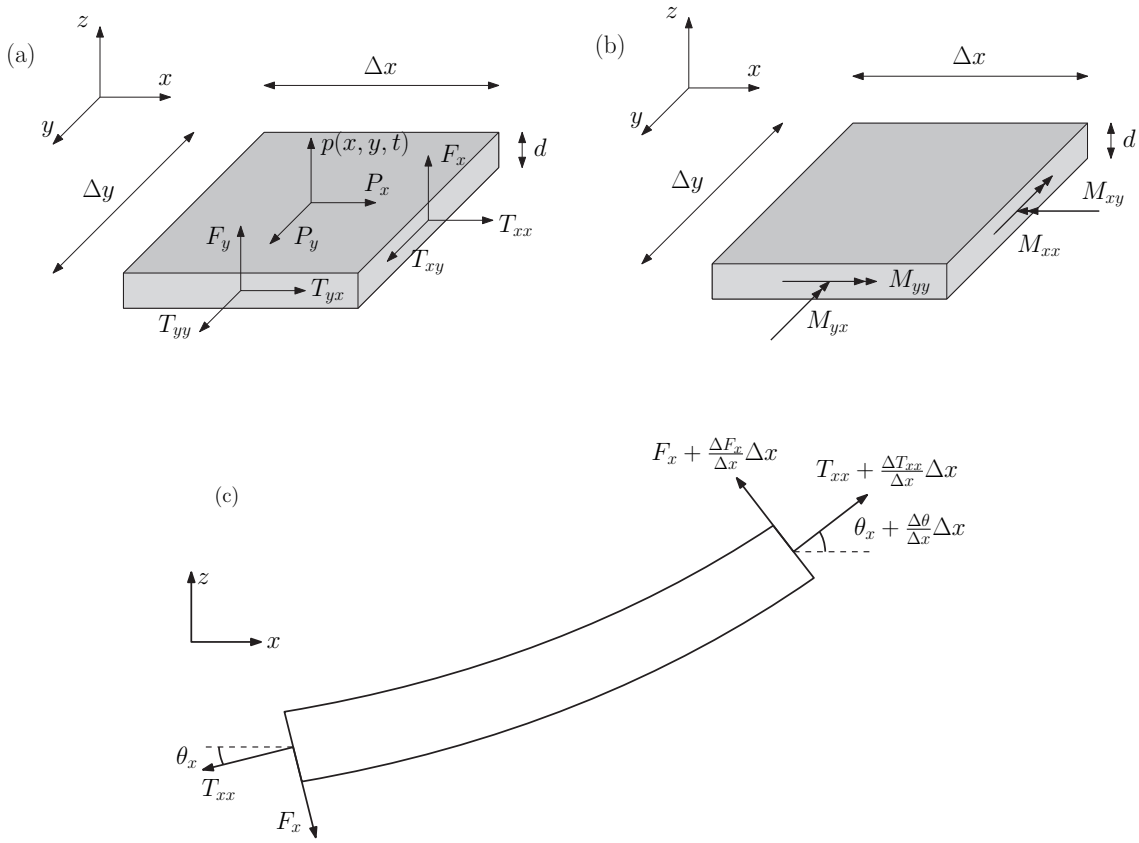

Figure 2.2: (a) Resultant forces acting on an elastic plate element. (b) Resultant moments acting on an elastic plate element. (c) Two dimensional cross section of a slightly-bent plate element. The angle θ are assumed to be small and are exaggerated in the figure for clarity.

F_i and shearing surface stress P_i where i, j indicates summation over $1, 2$ with $x_1 = x$ and $x_2 = y$. In contact with a liquid there will be a load per unit area acting on the plate, from the hydrodynamic pressure. In figure 2.2(b) we plot the resultant moments M_{ij}. Furthermore, the deformations make the plate deflect a length $h(x, y, t)$ from its flat equilibrium shape resulting in an angle θ_i appearing between the plate and the horizontal plane as depicted in figure 2.2(c). However, the deflections are assumed to be small such that the approximations $\theta_i \simeq \partial h/\partial x_i$, $\sin\theta_i \simeq \theta_i$, $\cos\theta_i \approx 1$ are valid. We therefore assume that any thickness variations of the plate is negligible and we thus define the resultant forces and moments as

$$T_{ij} = \int_{-d/2}^{d/2} \sigma_{ij} dz \ , \tag{2.4}$$

$$M_{ij} = \int_{-d/2}^{d/2} z\sigma_{ij} dz \ , \tag{2.5}$$

with σ_{ij} the Cauchy stress tensor [2]. The dimension of the resultant forces is force per unit length and the dimension of the resultant moments is moment per unit length. We now consider the case of zero shear on the plate surface, $P_x = P_y = 0$. We assume the response time of the elastic material is small compared to the observation time such that any change in the pressure yields an instantaneous response in the elastic deformation of the plate. Therefore we consider the plate to be at equilibrium and we obtain six equations of equilibrium, three for the force resultants and three for the moment resultants. In the limit $\Delta x, \Delta y \to 0$ and to leading order we get the three force equations [3]

$$x : \quad \frac{\partial T_{xx}}{\partial x} + \frac{\partial T_{xy}}{\partial y} = 0, \tag{2.6}$$

$$y : \quad \frac{\partial T_{yy}}{\partial y} + \frac{\partial T_{yx}}{\partial x} = 0, \tag{2.7}$$

$$z : \frac{\partial F_x}{\partial x} + \frac{\partial}{\partial x}\left(T_{xx}\frac{\partial h}{\partial x} + T_{xy}\frac{\partial h}{\partial x}\right) + \frac{\partial}{\partial y}\left(T_{yy}\frac{\partial h}{\partial y} + T_{xy}\frac{\partial h}{\partial y}\right) + \frac{\partial F_y}{\partial y} = -p, \tag{2.8}$$

and the three moment resultants equations

$$x : \quad \frac{\partial M_{yy}}{\partial y} + \frac{\partial M_{xy}}{\partial x} = F_y, \tag{2.9}$$

$$y : \quad \frac{\partial M_{xx}}{\partial x} + \frac{\partial M_{yx}}{\partial y} = F_x, \tag{2.10}$$

$$z : \quad T_{xy} - T_{yx} = 0. \tag{2.11}$$

In Eq.(2.8)(c) the notation $h = h(x, y, t)$ was used due to spatial constraints. The last equation points out the fact that the elastic stress tensor is symmetric. In the following derivation we assume plane stress conditions [2], *i.e.* $\sigma_{iz} = 0$ and that the deformations are of such order that the normal vector is parallel with the vertical axis. A displacement vector $\mathbf{u}_d = [u_d, v_d, w_d]$ can then be defined as

$$u_d(x, y, z, t) = u_d(x, y, t) - z\frac{\partial h(x, y, t)}{\partial x}, \tag{2.12a}$$

$$v_d(x, y, z, t) = v_d(x, y, t) - z\frac{\partial h(x, y, t)}{\partial y}, \tag{2.12b}$$

$$w_d(x, y, z, t) = h(x, y, t). \tag{2.12c}$$

Furthermore, due to the plane-stress conditions the stress-strain relation is given by [2]

$$\sigma_{xx} = \frac{E}{1-\nu^2}\left(u_{xx} + \nu u_{yy}\right), \tag{2.13a}$$

$$\sigma_{yy} = \frac{E}{1-\nu^2}\left(u_{yy} + \nu u_{xx}\right), \tag{2.13b}$$

$$\sigma_{xy} = \frac{E}{1+\nu}u_{xy}, \tag{2.13c}$$

with the strain defined as

$$u_{ij} = \frac{1}{2}\left(\frac{\partial u_i}{\partial x_j} + \frac{\partial u_j}{\partial x_i}\right) + \frac{1}{2}\frac{\partial h(x, y, t)}{\partial x_i}\frac{\partial h(x, y, t)}{\partial x_j}. \tag{2.14}$$

By combining Eqs.(2.12),(2.13),(2.14) and inserting into Eq.(2.5) we find that the resultant moments are purely functions of $h(x, y, t)$:

$$M_{xx} = -\frac{Ed^3}{12(1-\nu^2)}\left[\frac{\partial^2 h(x, y, t)}{\partial x^2} + \nu\frac{\partial^2 h(x, y, t)}{\partial y^2}\right], \tag{2.15}$$

$$M_{yy} = -\frac{Ed^3}{12(1-\nu^2)}\left[\nu\frac{\partial^2 h(x, y, t)}{\partial x^2} + \frac{\partial^2 h(x, y, t)}{\partial y^2}\right], \tag{2.16}$$

$$M_{yx} = -\frac{Ed^3}{24(1+\nu)}\left[\frac{\partial}{\partial y}\left(\frac{\partial h(x, y, t)}{\partial x}\right) + \frac{\partial}{\partial x}\left(\frac{\partial h(x, y, t)}{\partial y}\right)\right], \tag{2.17}$$

with E the Young's modulus of the elastic material and ν the Poisson ratio. Inserting the resultant moments into Eqs.(2.9)-(2.10), which subsequently are inserted into Eq.(2.8) we get the coupling between the applied load and elastic stresses, here expressed in vector notation [2, 6]

$$p(x, y, t) = \frac{Ed^3}{12(1-\nu^2)}\nabla^4 h(x, y, t) - \frac{\partial}{\partial x_i}\left(T_{ij}\frac{\partial h(x, y, t)}{\partial x_j}\right). \tag{2.18}$$

This equation combined with Eqs.(2.6)-(2.7) are collectively known as the Föppl-von Kármán equations.

In the literature, there are two commonly used simplifications of this model. The first being the case of no in-plane stress which yields a pure bending-driven equation [7, 8, 9]

$$p(x, y, t) = B\nabla^4 h(x, y, t) \tag{2.19}$$

where we have defined the plate bending rigidity B as

$$B = \frac{Ed^3}{12(1-\nu^2)}. \tag{2.20}$$

The second simplification is the one of isotropic in-plane tension, *i.e.* $T_{ij} = T$ is a constant in the entire plate which gives [10, 11]

$$p(x, y, t) = B\nabla^4 h(x, y, t) - T\nabla^2 h(x, y, t) \tag{2.21}$$

The latter equation is often solved with conservation of the plate area as an integral constraint, replacing Eqs.(2.6)-(2.7), to obtain a value for T [10].

As we have now defined the coupling between the hydrodynamic pressure in the liquid and the forces acting on the liquid-gas and liquid-elastic interface we need to describe how the hydrodynamic pressure is coupled to the viscous flow in the thin film. In order to do so we must first provide a description of the motion of a viscous liquid.

References

[1] Batchelor, G. K. *An introduction to fluid dynamics*. Cambridge university press, 1967.

[2] Landau, L. D. and Lifshitz, E. M. *Course of Theoretical Physics Vol 7: Theory and Elasticity*. Pergamon Press, 1959.

[3] Timoshenko, S. P. and Woinowsky-Krieger, S. *Theory of plates and shells*. McGraw-hill, 1959.

[4] Mansfield, E. H. *The bending and stretching of plates*. Cambridge university press, 2005.

[5] Love, A. E. H. *A treatise on the mathematical theory of elasticity*. Cambridge university press, 2013.

[6] Huang, R. and Suo, Z. "Instability of a compressed elastic film on a viscous layer". *International Journal of Solids and Structures* vol. 39, no. 7 (2002), pp. 1791–1802.

[7] Al-Housseiny, T. T., Christov, I. C., and Stone, H. A. "Two-phase fluid displacement and interfacial instabilities under elastic membranes". *Physical review letters* vol. 111, no. 3 (2013), p. 034502.

[8] Lister, J. R., Peng, G. G., and Neufeld, J. A. "Viscous control of peeling an elastic sheet by bending and pulling". *Physical review letters* vol. 111, no. 15 (2013), p. 154501.

[9] Tulchinsky, A. and Gat, A. D. "Transient dynamics of an elastic Hele-Shaw cell due to external forces with application to impact mitigation". *Journal of Fluid Mechanics* vol. 800 (2016), pp. 517–530.

[10] Kodio, O., Griffiths, I. M., and Vella, D. "Lubricated wrinkles: Imposed constraints affect the dynamics of wrinkle coarsening". *Physical Review Fluids* vol. 2, no. 1 (2017), p. 014202.

[11] Peng, G. G. and Lister, J. R. "Viscous-fingering mechanisms under a peeling elastic sheet". *Journal of Fluid Mechanics* vol. 864 (2019), pp. 1177–1207.

Chapter 3

Thin film dynamics

3.1 Navier-Stokes equations

The continuum description of the motion of a Newtonian viscous fluid is given by the Navier-Stokes equations [1]. It is a set of partial differential equations for which the first equation corresponds to conservation of momentum

$$\frac{\partial \mathbf{u}}{\partial t} + (\mathbf{u}\cdot\nabla)\mathbf{u} = -\frac{1}{\rho}\nabla p + \mu\nabla^2\mathbf{u} + \nabla\cdot\underline{\underline{\mathcal{S}}} \tag{3.1}$$

with $\mathbf{u} = [u, v, w]$ being the fluid velocity vector, ρ the fluid density, p the hydrodynamic pressure and μ the dynamic viscosity. The unusual last term in Eq.(3.1) accounts for thermal fluctuations in the liquid for which $\underline{\underline{\mathcal{S}}}$ is the symmetric fluctuating stress tensor with zero mean [2]. We neglect any gravitational effect as we only consider flows for which the characteristic capillary length and the elastogravity length $L_{\mathrm{e}} = (B/\rho g)^{1/4}$ [3] are small. The second equation describes conservation of mass, which for an incompressible Newtonian fluid of constant density is formulated as

$$\nabla\cdot\mathbf{u} = 0. \tag{3.2}$$

3.2 Lubrication theory

Lubrication theory [1] is the theory that describes viscous fluid flow in a geometry where one length scale is much smaller than the remaining two. Here we consider a thin film where the vertical length scales as a characteristic film thickness $\bar{h}$ and the two horizontal coordinates, x, y, scales as a characteristic system width L, with the ratio between the two $\epsilon = \bar{h}/L \ll 1$. Lubrication theory is valid for small film Reynold numbers which is defined as $\mathrm{Re}_f = \epsilon^2\mathrm{Re}$ where $\mathrm{Re} = \rho U\bar{h}/\mu$ is the Reynolds number and U a characteristic horizontal flow velocity. Thus, lubrication theory is valid for any finite Reynolds number as long as ϵ is sufficiently small. From a scaling analysis of the continuity equation, Eq.(3.2), we find that the vertical velocity component scales as $w \sim U\epsilon$. From this, to leading order in ϵ, Eq.(3.1) becomes

$$\frac{\partial p}{\partial x} = \mu\frac{\partial^2 u}{\partial z^2} + \frac{\partial \mathcal{S}_{xz}}{\partial z}, \tag{3.3}$$

$$\frac{\partial p}{\partial y} = \mu\frac{\partial^2 v}{\partial z^2} + \frac{\partial \mathcal{S}_{yz}}{\partial z}, \tag{3.4}$$

$$\frac{\partial p}{\partial z} = 0. \tag{3.5}$$

As the hydrodynamic pressure $p(x, y, t)$ is not a function of the vertical coordinate z we can integrate Eq.(3.3) and Eq.(3.4) with respect to z over the height of the film to obtain the horizontal flow components

$$u(x, y, t) = \frac{1}{2\mu}\frac{\partial p}{\partial x}z^2 + A_1 z + B_1 + \int_0^z dz' \mathcal{S}_{xz}(z'), \tag{3.6}$$

$$v(x, y, t) = \frac{1}{2\mu}\frac{\partial p}{\partial y}z^2 + A_2 z + B_2 + \int_0^z dz' \mathcal{S}_{yz}(z'). \tag{3.7}$$

The four coefficients A_1, A_2, B_1 and B_2 are determined from the boundary conditions at the two interfaces of the liquid phase. An illustration of the three thin film geometries that are relevant to this thesis are depicted in figure 3.1 for which the different dynamics are discussed below. At the solid interface we employ the no-slip boundary condition and at the free surface we can assume that the shear stress from the air is negligible due to its small viscosity. After the coefficients are found we can obtain the thin film equation by integrating the continuity equation over the film thickness

$$\int_0^{h(x,y,t)} dz \left(\frac{\partial u}{\partial x} + \frac{\partial v}{\partial y} + \frac{\partial w}{\partial z}\right) = 0. \tag{3.8}$$

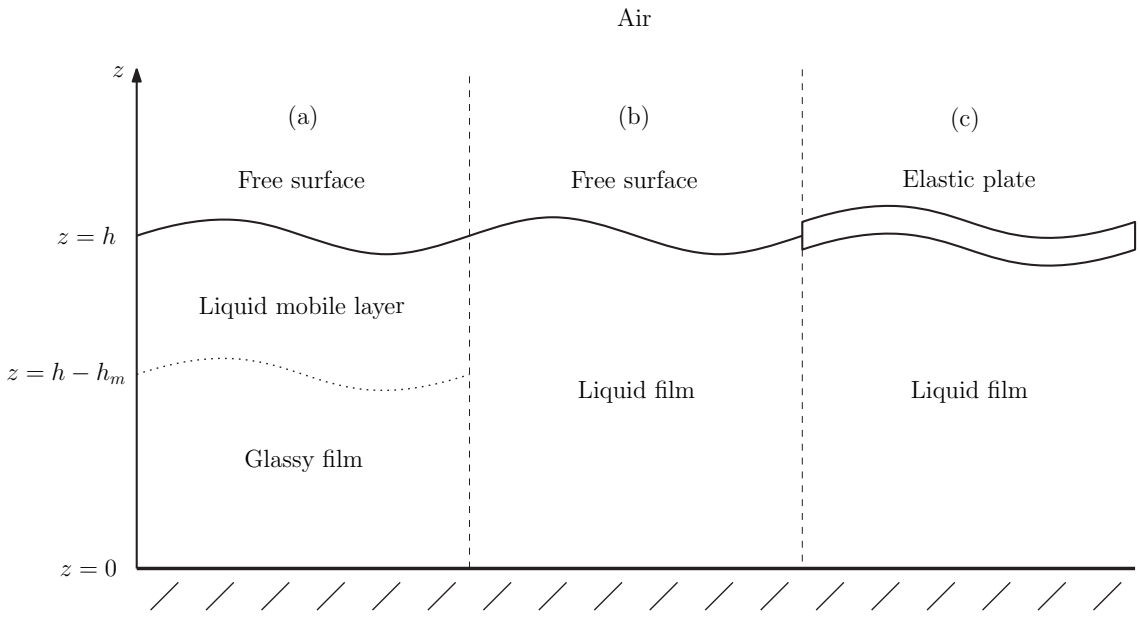

Figure 3.1: A schematic of the three thin film geometries at stake in this thesis. (a) A glassy material with a thin mobile layer of thickness h_m at the free surface with the glassy film considered to be solid, (b) a liquid film with a free surface, (c) a liquid film covered with an elastic plate.

3.3 Deterministic thin film regimes

In the so-called deterministic regime we neglect any effect from thermal fluctuations, i.e. $\underline{\underline{\mathcal{S}}} = \underline{\underline{0}}$. The molecular scale at which thermal fluctuation appear make this approximation valid for flows of greater thickness than a few nanometers.

3.3.1 Capillary-driven flow

The capillary-driven thin film equation describes the dynamics in a thin viscous film supported by a solid substrate and with a free interface to a gaseous phase of negligible viscosity as illustrated in figure 3.1b. A characteristic parameter describing flows that are driven by the balance of viscous and surface tension forces is the capillary number $\mathrm{Ca} = \mu U/\gamma$ [4] for which a small value indicates a surface tension dominated regime. We find the coefficients in Eqs.(3.6)-(3.7) by applying a no-slip condition at the solid substrate, $z = 0$, and a zero shear condition at the free surface $z = h(x, y, t)$. Applying the Leibniz integral rule [1] to Eq.(3.8), combined with Eq.(2.3), we find the capillary-driven thin film equation

$$\frac{\partial h(x,y,t)}{\partial t} + \frac{\gamma}{3\mu}\nabla \cdot \left[h^3(x,y,t)\nabla\nabla^2 h(x,y,t)\right] = 0. \tag{3.9}$$

From a modelling perspective, this equation has been essential to describe many dynamical processes [5]. By balancing the viscous forces in the fluid and the surface tension forces acting on the free interface it reproduces the canonical results of Tanner [6, 7], demonstrating that the baseline radius of a completely wetting droplet displays a power-law behaviour in time ($R(t) \sim t^{1/10}$).

The nonlinearity of the equation comes from the cubic amplitude term. By considering the film thickness to consist of two parts, one equilibrium thickness of constant thickness h_0 and one spatiotemporal perturbation amplitude $\hat{h}$, we see from Eq.(3.9) that for a droplet spreading on a pre-wetted layer of the same viscosity, the nonlinear effects should be decreasing for an increasing pre-wetted layer thickness. A mathematical analysis of the thin film equation [8] demonstrated the existence of two asymptotic spreading regimes determined by the ratio between the droplet height and the pre-wetted layer thickness. One is the nonlinear regime of Tanner's law that is valid for large ratio values, and the other is a linear regime for small ratio values for which the spreading rate of the droplet is significantly increased.

Similar to the capillary-driven thin film equation, the flow dynamics in the mobile layer of a glassy material is driven by the surface tension forces acting on the free interface. However, due to the existence of the mobile layer (see figure 3.1(a)) of constant thickness h_m, Eq.(3.8) is here linear by nature, and reads [9, 10]

$$\frac{\partial h(x,y,t)}{\partial t} + \frac{\gamma h_m^3}{3\mu}\nabla^4 h(x,y,t) = 0. \tag{3.10}$$

The form of this equation is reminicent of the linearized capillary-driven thin film equation but with a different prefactor called the mobility parameter [10].

However, the linearity of this equation is purely due to the boundary conditions and should not be confused with the existence of a thick supporting film as we in fact are in the opposite regime. A particular way to obtain values for the mobility parameter is by mathcing numerical solutions to experimental data [10]. A novel observation is that a scaling analysis of Eq.(3.10) suggest that a droplet spreading on the mobile layer should follow a $R(t) \sim t^{1/8}$ behaviour. This is different from capillary-driven spreading behaviour suggested by Tanner's law and is yet to be experimentally confirmed.

3.3.2 Elastohydrodynamic flow

The last geometry to consider is the one of a liquid film which is capped by an elastic membrane, see figure 3.1(c). As there is a liquid-solid interface at $z = h(x, y, t)$ we employ the no-slip boundary condition at both liquid-solid interfaces. Eq.(3.8), combined with Eq.(2.18), then becomes

$$\frac{\partial h(x,y,t)}{\partial t} = \frac{1}{12\mu}\nabla \cdot \left[h^3(x,y,t)\nabla \left(B\nabla^4 h(x,y,t) + \frac{\partial}{\partial x_i}\left(T_{ij}\frac{\partial h(x,y,t)}{\partial x_j} \right) \right) \right]. \tag{3.11}$$

Lister et al. [3] used an asymptotic matching procedure to derive an elastohydrodynamic equivalent to Tanner's law. For a fluid filled elastic blister spreading on top of a very thin pre-wetted layer, the dynamics can be divided into a bending-driven regime and a tension-driven regime. As the blister spreads, the elastic sheet is peeled off from the pre-wetted layer. For thin films this process is very slow and the pressure in the bulk of the blister can be considered to be uniform. Further analysis on the levelling of a viscous bump, capped by an elastic sheet [11, 12], found the elastohydrodynamic Tanner exponent to be $R(t) \sim t^{1/11}$. A transition from the nonlinear regime to the linear regime is also found for elastohydrodynamic flows using scaling analysis [12], see figure 3.2a.

Effects from spatial confinement on an elastic plate have been studied in a one-dimensional geometry with a large pre-wetted layer thickness and isotropic in-plane tension, $T_{ij} = T$ [13]. Analysis revealed that when compressing the plate, initial wrinkles are formed with a wave length that grows as $\lambda \sim (t/\log(t))^{1/6}$. Result from [13] are reproduced and plotted in figure 3.2(b). Starting with a random initial condition for the height perturbation $\hat{h}$ on top of a film with equilibrium thickness $h_0 = 1$, wrinkles form immediately and grow in width until they merge. Towards the end, the number of wrinkles is reduced before the entire plate buckles into a final equilibrium shape where the plate energy is at a minimum. Preliminary investigations into the effects of confinement in the nonlinear regime, for a very thin pre-wetted layer, are displayed in figure 3.2c. Here the initial film thickness is $h_0 = 0.01$. Using the similar random initial condition as in the thick film regime we see that the dynamics change. It takes longer time before the wrinkles form and instead of a homogenous merging of wrinkles, there seems to be one wrinkle that initiates a buckling-like process.

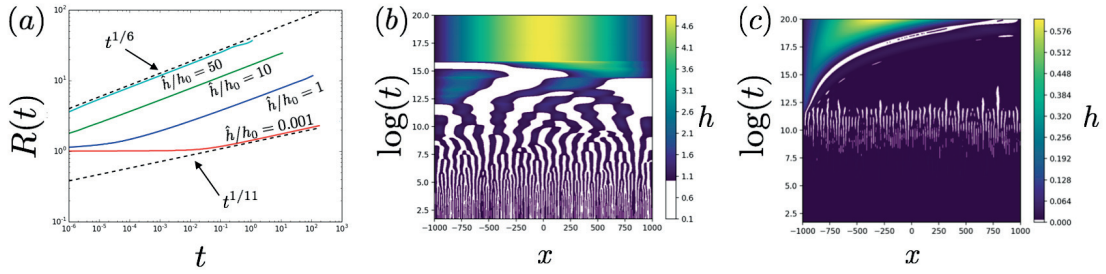

Figure 3.2: (a) Temporal evolution of the radius, $R(t)$, of an axisymmetric fluid filled blister spreading on top of viscous films of different equilibrium thickness h_0. (b)-(c) Wrinkle formation in spatially compressed thin elastic plates resting on viscous films of different thickness. The figures show the one-dimensional height contours of the film profiles over time. The white color indicate film thickness less than the equilibrium thickness h_0. (b) Linear regime, the supporting film thickness is unity, (c) Nonlinear regime, supporting film thickness is $h_0 = 0.01$.

A studied problem that highlight the importance of including the full Föppl-von Kármán equations is the one of instabilities that occur at the advancing front of a spreading blister and fingering instabilites in confined elastohydrodynamic flows [14, 15, 16, 17, 18, 19].

3.4 Stochastic thin film regimes

Traditionally, fluctuations dynamics such as Brownian motion have been studied using molecular dynamics simulations or phase separation in binary mixtures using phase field models. A phenomenological fluctuating hydrodynamical model was developed by Landau and Lifshitz [20] by adding a fluctuating symmetric stress to the Navier-Stokes momentum equation (Eq.(3.1)). Further studies on the origin of the fluctuating stress showed that it can be derived from the Boltzmann equation [21], and in the last decades the fluctuating stress have been included in coarse-grained continuum models [11, 22, 23, 24]. The stochastic elastohydrodynamic thin film equation associated with the Eqs.(3.3)-(3.5) is

$$\frac{\partial h(x,y,t)}{\partial t} = \nabla \cdot \left[\frac{h^3(x,y,t)}{12\mu} \nabla p(x,y,t) + \Gamma h^{3/2}(x,y,t) \eta(x,y,t) \right] \tag{3.12}$$

with $\Gamma = (k_\mathrm{B} T_\mathrm{a}/6\mu)^{1/2}$ the noise amplitude term with k_B the Boltzmann constant and T_a the ambient temperature. $\eta(x,y,t)$ is the gaussian white noise with zero mean and delta correlated in space and time as $\langle \eta(x,y,t)\eta(x',y',t') = \delta(x-x')\delta(y-y')\delta(t-t') \rangle$ with δ the Dirac delta function. The last term in Eq.(3.12) is obtained by averaging the stochastic terms in Eqs.(3.6)-(3.7) over the height when integrating Eq.(3.8) in the z-direction. A recent study show that this formulation fulfils the condition of detailed balance [25].

The effect of thermal fluctuations on droplet spreading dynamics, and its elastohydrodynamic analogue, have been studied with analytical and numerical tools [11, 23]. Both studies highlight a crossover from the nonlinear Tanner's regime to a stochastic driven regime.

References

[1] Batchelor, G. K. *An introduction to fluid dynamics*. Cambridge university press, 1967.

[2] Landau, L. D. and Lifshitz, E. M. *Course of theoretical physics*. Elsevier, 2013.

[3] Lister, J. R., Peng, G. G., and Neufeld, J. A. "Viscous control of peeling an elastic sheet by bending and pulling". *Physical review letters* vol. 111, no. 15 (2013), p. 154501.

[4] De Gennes, P.-G. "Wetting: statics and dynamics". *Reviews of modern physics* vol. 57, no. 3 (1985), p. 827.

[5] Oron, A., Davis, S. H., and Bankoff, S. G. "Long-scale evolution of thin liquid films". *Reviews of modern physics* vol. 69, no. 3 (1997), p. 931.

[6] Tanner, L. "The spreading of silicone oil drops on horizontal surfaces". *Journal of Physics D: Applied Physics* vol. 12, no. 9 (1979), p. 1473.

[7] Eggers, J. "Nonlinear dynamics and breakup of free-surface flows". *Reviews of modern physics* vol. 69, no. 3 (1997), p. 865.

[8] Cormier, S. L. et al. "Beyond Tanner's law: Crossover between spreading regimes of a viscous droplet on an identical film". *Physical review letters* vol. 109, no. 15 (2012), p. 154501.

[9] Salez, T. et al. "Capillary-driven flow induced by a stepped perturbation atop a viscous film". *Physics of Fluids* vol. 24, no. 10 (2012), p. 102111.

[10] Chai, Y. et al. "A direct quantitative measure of surface mobility in a glassy polymer". *Science* vol. 343, no. 6174 (2014), pp. 994–999.

[11] Carlson, A. "Fluctuation assisted spreading of a fluid filled elastic blister". *Journal of Fluid Mechanics* vol. 846 (2018), pp. 1076–1087.

[12] Pedersen, C. et al. "Asymptotic regimes in elastohydrodynamic and stochastic leveling on a viscous film". *Physical Review Fluids* vol. 4, no. 12 (2019), p. 124003.

[13] Kodio, O., Griffiths, I. M., and Vella, D. "Lubricated wrinkles: Imposed constraints affect the dynamics of wrinkle coarsening". *Physical Review Fluids* vol. 2, no. 1 (2017), p. 014202.

[14] Pihler-Puzovic, D. et al. "Displacement flows under elastic membranes. Part 1. Experiments and direct numerical simulations". *Journal of Fluid Mechanics* vol. 784 (2015), p. 487.

[15] Pihler-Puzović, D. et al. “Viscous fingering in a radial elastic-walled Hele-Shaw cell”. *Journal of Fluid Mechanics* vol. 849 (2018), pp. 163–191.

[16] Juel, A., Pihler-Puzović, D., and Heil, M. “Instabilities in blistering”. *Annual Review of Fluid Mechanics* vol. 50 (2018), pp. 691–714.

[17] Peng, G. G. and Lister, J. R. “Viscous-fingering mechanisms under a peeling elastic sheet”. *Journal of Fluid Mechanics* vol. 864 (2019), pp. 1177–1207.

[18] Heil, M. and Hazel, A. L. “Fluid-structure interaction in internal physiological flows”. *Annual review of fluid mechanics* vol. 43 (2011), pp. 141–162.

[19] Fontana, J. V. et al. “Modelling finger propagation in elasto-rigid channels”. *Journal of Fluid Mechanics* vol. 916 (2021).

[20] Landau, L. D. and Lifshitz, E. M. *Course of Theoretical Physics Vol 7: Theory and Elasticity*. Pergamon Press, 1959.

[21] Mashiyama, K. T. and Mori, H. “Origin of the Landau-Lifshitz hydrodynamic fluctuations in nonequilibrium systems and a new method for reducing the Boltzmann equation”. *Journal of Statistical Physics* vol. 18, no. 4 (1978), pp. 385–407.

[22] Mecke, K. and Rauscher, M. “On thermal fluctuations in thin film flow”. *Journal of Physics: Condensed Matter* vol. 17, no. 45 (2005), S3515.

[23] Davidovitch, B., Moro, E., and Stone, H. A. “Spreading of viscous fluid drops on a solid substrate assisted by thermal fluctuations”. *Physical review letters* vol. 95, no. 24 (2005), p. 244505.

[24] Grün, G., Mecke, K., and Rauscher, M. “Thin-film flow influenced by thermal noise”. *Journal of Statistical Physics* vol. 122, no. 6 (2006), pp. 1261–1291.

[25] Durán-Olivencia, M. A. et al. “Instability, rupture and fluctuations in thin liquid films: Theory and computations”. *Journal of statistical physics* vol. 174, no. 3 (2019), pp. 579–604.

Chapter 4

Numerical methods

The main challenge when solving thin film equations with numerical tools is that they are partial differential equations (PDEs) with higher order derivatives of the film profile height $h(x, y, t)$ and a cubic nonlinearity in the film height. But there are well developed methods that ease the numerical implementation which we will discuss below.

4.1 Finite element method

At the core of the finite element method lies the variational formulation of a PDE [1]. This is convenient when studying equations containing higher order derivatives as it reduces the order of the equation. We now turn our attention to the elastohydrodynamic thin film equation, Eq.3.11. As the following procedure is general for all problems studied in this thesis we limit our scope in the following to the case of bending-driven flow, i.e. $T_{ij} = T = 0$. It is desired when discretizing our numerical domain to use piecewise linear finite elements. This is mainly due to the increased computational cost when choosing higher order polynomials. There are also constraints related to the smoothness and regularity of the solution in order to benfit from higher order polynomials, which will not be discussed here. We refer the reader to the cited literature for additional information regarding such questions. To be able to use piecewise linear elements we introduce an auxiliary function $f(x, y, t) = \nabla^2 h(x, y, t)$ such that the pressure term reads $p(x, y, t) = B\nabla^2 f(x, y, t)$. By doing this we can split our PDE into three coupled equations:

$$\frac{\partial h}{\partial t} = \frac{1}{12\mu}\nabla \cdot \left(h^3 \nabla p\right), \tag{4.1a}$$

$$p = B\nabla^2 f, \tag{4.1b}$$

$$f = \nabla^2 h. \tag{4.1c}$$

Thus, we can seek a solution for all three variables in the Sobolev space H_0^1 [1]. We multiply Eqs.(4.1)(a-c) with the test functions ϕ, ψ and φ and perform integration by parts over the spatial domain Ω to obtain the variational formulation of the problem: find $h, f, p \in H^1(\Omega)$ such that

$$\int_\Omega \frac{\partial h}{\partial t}\phi \, dx + \frac{1}{12\mu}\int_\Omega h^3 \nabla p \cdot \nabla \phi \, dx - \frac{1}{12\mu}\int_{\partial\Omega} h^3 \nabla p \cdot \mathbf{n}\phi \, dx = 0, \qquad \forall \, \phi \in H^1(\Omega), \tag{4.2a}$$

$$\int_\Omega p\psi \, dx + B \int_\Omega \nabla f \cdot \nabla \psi \, dx - B \int_{\partial\Omega} \nabla f \cdot \mathbf{n} \psi \, dx = 0, \qquad \forall \, \psi \in H^1(\Omega), \tag{4.2b}$$

$$\int_\Omega f\varphi \, dx + \int_\Omega \nabla h \cdot \nabla \varphi \, dx - \int_{\partial\Omega} \nabla h \cdot \mathbf{n} \varphi \, dx = 0, \qquad \forall \, \varphi \in H^1(\Omega). \tag{4.2c}$$

with $\mathbf{n}$ the boundary normal vector in this context. To solve Eqs.(4.2) we must apply boundary conditions at the boundary $\partial\Omega$. Relevant conditions for the problems in this thesis are Dirichlet or Neuman conditions, *i.e.* setting a value for the function we are solving for or its derivative, respectively [1]. The type of boundary condition we choose depends on the physical system we are interested in. To solve the temporal problem in Eq.(4.2)(a) we discretize the time derivative with a backward Euler scheme

$$\left(\frac{\partial h}{\partial t}\right)^{n+1} \approx \frac{h^{n+1} - h^n}{\Delta t}. \tag{4.3}$$

with n being the time step. We solve the coupled set of equations in Eq.(4.2) implicitly in a mixed function space using a Newton solver from the open-source finite element library FEniCS [2]. The Newton solver is an iterative solver that iterates until a pre-set residual is reached. When the desired residual is obtained we assign the solution h^{n+1} to h^n before we start the Newton iteration procedure over again.

For further details regarding implementation, theory or the FEniCS library in general we refer the reader to the cited literature [1, 2].

References

[1] Brenner, S. C., Scott, L. R., and Scott, L. R. *The mathematical theory of finite element methods*. Vol. 3. Springer, 2008.

[2] Logg, A., Mardal, K.-A., and Wells, G. *Automated solution of differential equations by the finite element method: The FEniCS book*. Vol. 84. Springer Science & Business Media, 2012.

Chapter 5

Summary of papers

5.1 Paper I: Asymptotic regimes in elastohydrodynamic and stochastic leveling on a viscous film

An elastic sheet that deforms near a solid substrate in a viscous fluid is a situation relevant to various dynamical processes in biology, geophysics, and engineering. Here, we study the relaxation dynamics of an elastic plate resting on a thin viscous film that is supported by a solid substrate. By combining scaling analysis, numerical simulations, and experiments, we identify asymptotic regimes for the elastohydrodynamic leveling of a surface perturbation of the form of a bump, when the flow is driven by either the elastic bending (figure 5.1a) of the plate or thermal fluctuations (figure 5.1b). In both cases, two distinct regimes are identified when the bump height is either much larger or much smaller than the thickness of the prewetted viscous film. Our analysis reveals a distinct crossover between the similarity exponents with the ratio of the perturbation height to the film height.

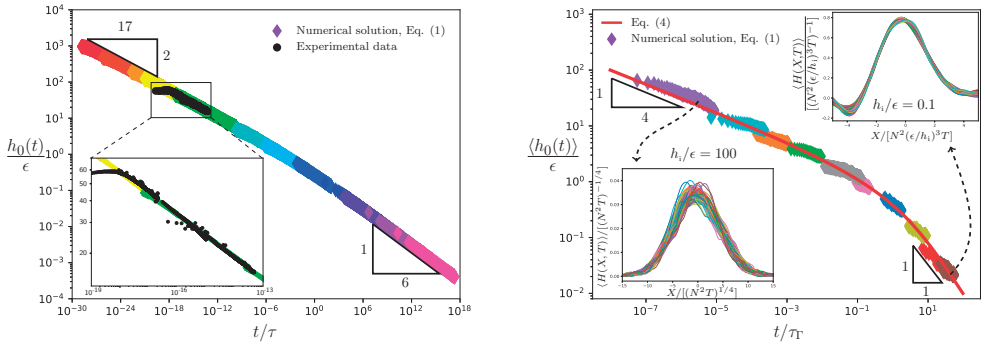

Figure 5.1: Nondimensional bump height as a function of dimensionless time. The colored diamond-shaped markers are rescaled data points from the numerical solutions of the dimensionless elastohydrodynamic thin film equation. The black circle-shaped marker are scaled experimental data points. (a) Deterministic bending-driven regime (b) Stochastic regime.

5.2 Paper II: Universal Self-Similar Attractor in the Bending-Driven Leveling of Thin Viscous Films

We study theoretically and numerically the bending-driven leveling of thin viscous films within the lubrication approximation. We derive the Green's function of

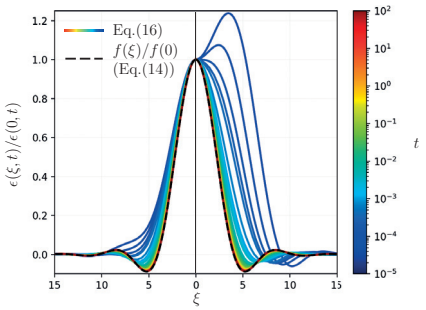

Figure 5.2: Rescaled film profiles as a function of a similarity variable. The two panes show the numerical solution to the bending-driven thin film equation starting from different initial conditions. Both profiles converge in time towards the universal self-similar attractor, represented by the black dashed line.

the linearized thin-film equation and further show that it represents a universal self-similar attractor at long times. As such, the rescaled perturbation of the film profile converges in time towards the rescaled Green's function, for any summable initial perturbation profile, see figure 5.2. In addition, for stepped axisymmetric initial conditions, we demonstrate the existence of another, short-term and one-dimensional-like self-similar regime. Besides, we characterize the convergence time towards the long-term universal attractor in terms of the relevant physical and geometrical parameters, and provide the local hydrodynamic fields and global elastic energy in the universal regime as functions of time. Finally, we extend our analysis to the non-linear thin-film equation through numerical simulations.

5.3 Paper III: Capillary deformation of ultrathin glassy polymer films by air nanobubbles

Confined glasses and their anomalous interfacial rheology raise important questions in fundamental research and numerous practical applications. In this work, we study the influence of interfacial air nanobubbles on the free surface of ultrathin high-molecular-weight glassy polystyrene films immersed in water, in ambient conditions (see figure 5.3a). In particular, we reveal the counterintuitive fact that a soft nanobubble is able to deform the surface of a rigid glass, forming a nanocrater with a depth that increases with time. By combining in situ atomic-force-microscopy measurements and a modified lubrication model for the liquidlike layer at the free surface of the glass, we demonstrate that the capillary pressure in the nanobubble together with the liquidlike layer at the free surface of the glass determine the spatiotemporal growth of the nanocraters. Finally, from the excellent agreement between the experimental profiles and the numerical solutions of the governing glassy thin-film equation (figure 5.3c), we are able to precisely extract the surface mobility of the glass. In addition to revealing and quantifying how surface nanobubbles deform immersed glasses,

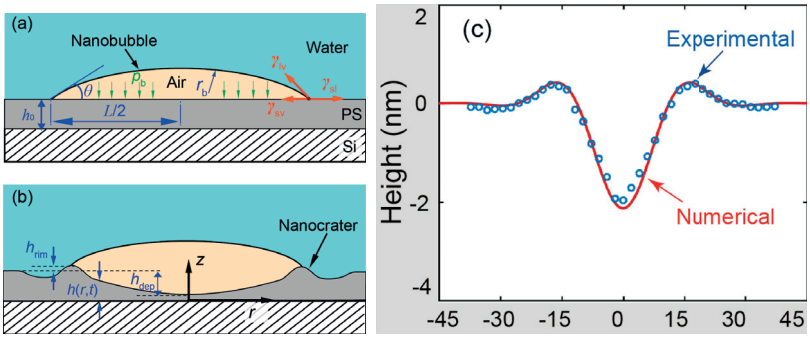

Figure 5.3: (a) Schematic of a nanobubble placed on top of a thin film of polystyrene. (b) The thin film flows due to the large Laplace pressure inside the nanobubble. (c) Comparing the numerical solution of the glassy thin film equation with experimental data.

until the latter eventually dewet from their substrates, our work provides a novel, precise, and simple measurement of the surface nanorheology of glasses.

5.4 Paper IV: Nanobubble-induced flow of immersed glassy polymer films

We study the free-surface deformation dynamics of an immersed glassy thin polymer film supported on a substrate, induced by an air nanobubble at the free surface. We combine analytical and numerical treatments of the glassy thin film equation, resulting from the lubrication approximation applied to the surface mobile layer of the glassy film, under the driving of an axisymmetric step function in the pressure term accounting for the nanobubble's Laplace pressure. Using the method of Green's functions, we derive a general solution for the film

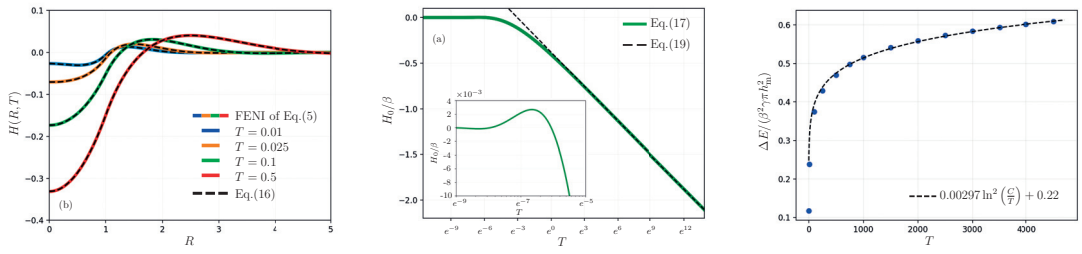

Figure 5.4: (a) Evolution of the surface profile of a glassy thin film in the presence of a nanobubble. The solid lines are the numerical solution to the glassy thin film equation and the dashed line are the numerical estimate of the profile integral solution. (b) Normalized central height of the bubble-induced perturbation of the film profile as a function of time. (c) Normalized excess surface energy of the film as a function of time. The circle-shaped points are calculated using the numerical estimate of the surface profile and the dashed line is the theoretical prediction.

profile (figure 5.4a). We show that the lateral extent of the surface perturbation follows an asymptotic viscocapillary power-law behaviour in time, and that the film's central height decays logarithmically in time in this regime, see figure 5.4b. This process eventually leads to film rupture and dewetting at finite time, for which we provide an analytical prediction exhibiting explicitly the dependencies in surface mobility, film thickness and bubble size, among others (see figure 5.4c). Finally, using finite-element numerical integration, we discuss how non-linear effects induced by the curvature and film profile can affect the evolution.

5.5 Paper V: Film deposition and dynamics of a self-propelled wetting droplet on a conical fibre

A viscous droplet placed on a conical structure will spontaneously move towards the thicker part of the structure. The spontaneous motion occurs because there is a difference of the contact angles at the advancing front and the receding part of the droplet due to the conical structure.

We study the dynamic wetting of a self-propelled viscous droplet using the time-dependent lubrication equation on a conical-shaped substrate for different cone radii, cone angles and slip lengths. The droplet velocity is found to increase with the cone angle and the slip length, but decrease with the cone radius. We show that a film is formed at the receding part of the droplet, much like the classical Landau–Levich–Derjaguin film. The film thickness h_f is found to decrease with the slip length λ. By using the approach of matching asymptotic profiles in the film region and the quasi-static droplet, we obtain the same film thickness as the results from the lubrication approach for all slip lengths. We identify two scaling laws for the asymptotic regimes: $h_f h_o'' \sim \mathrm{Ca}^{2/3}$ for $\lambda \ll h_f$ and $h_f h_o \sim (\mathrm{Ca}/\lambda)^2$ for $\lambda \gg h_f$; here, $1/h_o''$ is a characteristic length at the receding contact line and Ca is the capillary number. We compare the position and the shape of the droplet predicted from our continuum theory with molecular dynamics simulations, which are in close agreement. Our results show that manipulating the droplet size, the cone angle and the slip length provides different schemes for guiding droplet motion and coating the substrate with a film.

5.6 Paper VI: Film coating by directional droplet spreading on fibers

Plants and insects use slender conical structures to transport and collect small droplets, which are propelled along the conical structures due to capillary action. These droplets can deposit a fluid film during their motion, but despite its importance to many biological systems and industrial applications, the properties of the deposited film are unknown. We characterize the film deposition by developing an asymptotic analysis together with experimental measurements and numerical simulations based on the lubrication equation. We show that the deposited film thickness depends significantly on both the fiber radius and

the droplet size, highlighting that the coating is affected by finite-size effects relevant to film deposition on fibers of any slender geometry. We demonstrate that by changing the droplet size, while the mean fiber radius and the capillary number are fixed, the thickness of the deposited film can change by an order of magnitude or more. We show that self-propelled droplets have significant potential to create passively coated structures.

Chapter 6

Future perspective

This thesis is a collection of articles that use lubrication theory to describe a variety of flow phenomena driven by different mechanisms. Below I outline some interesting future problems for which thin film models can contribute towards understanding the underlying physics that dictate the dynamics as well as some thoughts on natural extensions of this work.

With increasing accuracy and resolution in experimental measurements the scale on which we can observe dynamical systems are ever decreasing. This has enabled the study of fluctuating molecular dynamics such as brownian motion of particles in confinement. However, for fluctuations to dominate the dynamics in previously discussed spreading processes there is need for liquids with vanishingly small surface tension coefficients. One way to possibly omit this is to study fluctuation assisted spreading of droplet in critical binary mixtures close to the critical temperature. When approaching the critical temperature surface tension vanishes. Experiments conducted by our collaborators in the group of Dr. Jean-Pierre Delville at the University of Bordeaux show that a spreading droplet deviates from the predictions of Tanner's law when approaching the critical temperature. This is interesting because it can enable us to study the effect of thermal fluctuations on thin film flows above the nanoscale.

It is well known that a thin fluid film can rupture and dewet a solid substrate if the film surface is perturbed from its equilibrium state, a process which is governed by the balance between surface tension forces and a disjoining pressure. At the sub-micron scale, such destabilising perturbations can naturally be caused, and enhanced, by thermal fluctuations and it is therefore difficult to control the stability of thin films at these scales. However, it is also known that a shear flow can reduce the amplitude of the thermal capillary rugosity [1]. Thus, combining the effects from thermal fluctuations, disjoining pressure and surface tension with an imposed shear flow can lead to a new proposal of shear stabilisation of thin films at the nanoscale.

As discussed in section 3.3.2, local compression effects can influence the dynamics of spatially confined elastic plates. It is therefore needed to extend the elastic plate model to a Föppl-von Kármán model to investigate how localized compression affect the flow dynamics, *e.g.* wrinkling in spatial confinement. Dr. Joel Marthelot (Aix-Marseille University) and Dr. Jérome Gaudin (Univeristy of Bordeaux) have performed a series of experiments where they study a thin film of germanium telluride (GeTe) which is capped with a thin layer of silicon nitrade (SiN). They heat the GeTe film into a viscous film using a focused laser beam and they subsequently observe wrinkles on the SiN surface. This is an ideal setup to further study wrinkle formation and the evolution of wrinkle wavelength in confined elastic membranes.

All the problems outlined here are natural extensions of the work already conducted during my doctoral studies but they also raise challenging new question. There are several interesting small scale features that go beyond the thin film models we have discussed here. A particular problem related to plate dynamics when the supporting film is heated is how the increased temperature can lead to thermal expansion of the elastic plate. We have here only considered elastic plates of constant thickness. An interesting question is how thermaly induced thickness variations in the plate can affect the flow dynamics. Also, could thermal expansion of the plate affect other properties such as the bending rigidity? With new questions like this comes also the need for new models that can answer them. Thus, the inclusion of additional physical effects in thin film models have the potential to give new insight into small scale flow systems that are still not fully understood in the near future.

References

[1] Thiébaud, M. and Bickel, T. "Nonequilibrium fluctuations of an interface under shear". *Physical Review E* vol. 81, no. 3 (2010), p. 031602.

Papers

Paper I

Asymptotic regimes in elastohydrodynamic and stochastic leveling on a viscous film

Christian Pedersen, John F. Niven, Thomas Salez, Kari Dalnoki-Veress, Andreas Carlson

Published in Physical Review Fluids 4, 124003 (2019). DOI: https://doi.org/10.1103/PhysRevFluids.4.124003.

Asymptotic regimes in elastohydrodynamic and stochastic leveling on a viscous film

Christian Pedersen,[1] John F. Niven,[2] Thomas Salez,[3,4]
Kari Dalnoki-Veress,[2] and Andreas Carlson[1,*]

[1]*Mechanics Division, Department of Mathematics, University of Oslo, 0316 Oslo, Norway*
[2]*Department of Physics and Astronomy, McMaster University, 1280 Main Street West, Hamilton, Ontario L8S 4M1, Canada*
[3]*Univ. Bordeaux, CNRS, LOMA, UMR 5798, F-33405 Talence, France*
[4]*Global Station for Soft Matter, Global Institution for Collaborative Research and Education, Hokkaido University, Sapporo, Hokkaido 060-0808, Japan*

(Received 21 February 2019; published 19 December 2019)

An elastic sheet that deforms near a solid substrate in a viscous fluid is a situation relevant to various dynamical processes in biology, geophysics, and engineering. Here, we study the relaxation dynamics of an elastic plate resting on a thin viscous film that is supported by a solid substrate. By combining scaling analysis, numerical simulations, and experiments, we identify asymptotic regimes for the elastohydrodynamic leveling of a surface perturbation of the form of a bump, when the flow is driven by either the elastic bending of the plate or thermal fluctuations. In both cases, two distinct regimes are identified when the bump height is either much larger or much smaller than the thickness of the prewetted viscous film. Our analysis reveals a distinct crossover between the similarity exponents with the ratio of the perturbation height to the film height.

DOI: 10.1103/PhysRevFluids.4.124003

I. INTRODUCTION

The motion of an elastic sheet supported by a thin layer of viscous fluid is a phenomenon that manifests itself in processes spanning wide ranges of time and length scales, from, e.g., magmatic intrusion in the Earth's crust [1,2], to fracturing and crack formation in glaciers [3], to pumping in the digestive and arterial systems [4–6], or the construction of two-dimensional (2D) crystals for electronic engineering [7]. Elastohydrodynamic flows have been studied in model geometries in order to understand their generic features and the inherent coupling between the driving force from the elastic deformations of the material and the viscous friction force resisting motion [8–16].

The investigation of an initially flat elastic membrane that is subsequently subjected to an applied deformation has helped disclose how system size, magnitude, and direction of elastic deformations [17] and spatial confinement [18,19] affect the membrane dynamics. When a membrane, resting on a fluid, is either compressed or stretched it can generate wrinkles, where the spatiotemporal dynamics of these folds couple to the fluid flow [18–21]. Wrinkles can be avoided by a slow out-of-plane deformation of an elastic plate by means of injecting additional fluid into the thin prewetted film, which leads to a peeling front driven by bending [22,23]. As the fluid blister grows in size, stretching of the plate generates a tension that starts to dominate over bending. Once the blister is larger than the elasto-gravity length [8], the peeling dynamics again alter character as gravity starts to dominate, giving three distinct regimes for the propagating front [22]. If the supporting film is

*acarlson@math.uio.no

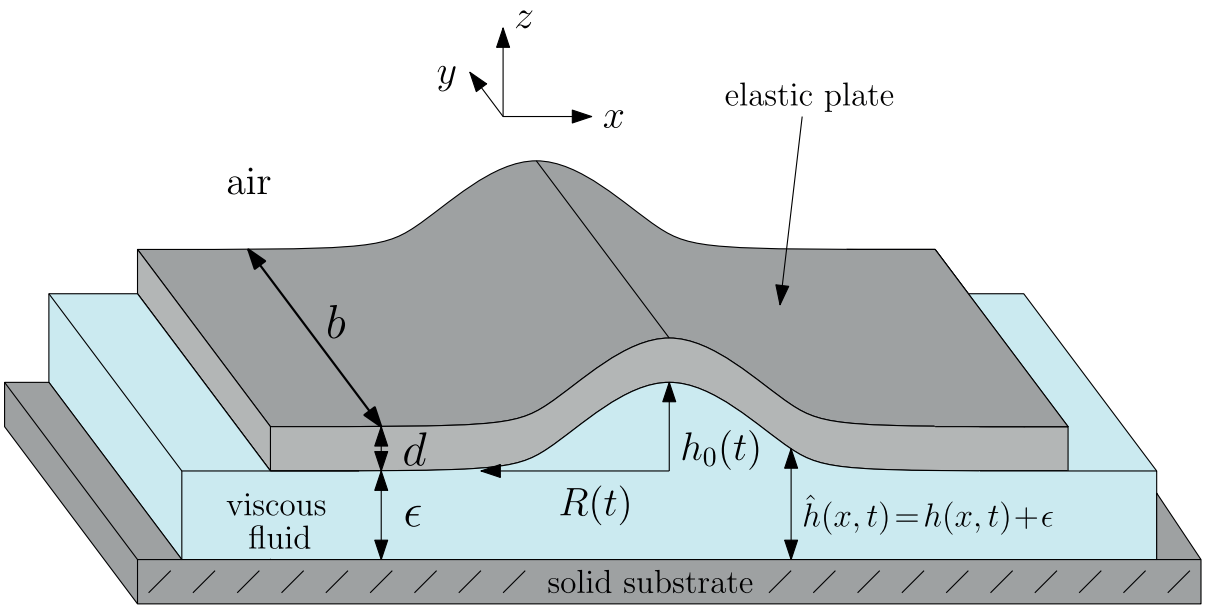

FIG. 1. Schematic of the system we are studying, where an elastic plate is supported by a viscous film on a solid substrate, surrounded by ambient air. The elastic plate has a thickness d and a width b. Initially, the overall profile presents a localized bump, whose profile is invariant in the y direction, i.e., quasi two dimensional. Far away from the perturbation, the viscous film has a constant thickness ϵ. In the bump region, the height profiles $\hat{h}(x,t)$ and $h(x,t)=\hat{h}(x,t)-\epsilon$ of the viscous film and the bump, respectively, vary with the horizontal position x and time t, and remain symmetric about $x=0$. At $x=0$, we define the characteristic height $h(x=0,t)=h_0(t)$ of the bump and its typical radius $R(t)$, with initial values given as $h_0(t=0)=h_\mathrm{i}$ and $R(t=0)=R_\mathrm{i}$.

instead of nanoscopic thickness, elastic bending generates a restoring force trying to oppose the van der Waals force that pulls the plate towards the wall and can lead to an elastohydrodynamic touchdown [24] similar to the dewetting of a liquid film [25]. One way to approach a theoretical description of elastohydrodynamics is to solve the Navier-Stokes equations for the fluid flow using boundary conditions at the elastic interface given by the solution of the Föppl-von Kármán equation [26], using, e.g., the immersed-boundary method [27]. Viscous flow in thin films can be described by the lubrication theory [28] that has been widely used to study different elastohydrodynamic flow phenomena [8,22–24,26,29]. However, not much is known about how elastohydrodynamic flows are affected by the ratio between the geometric parameters that characterize the system as it undergoes large changes while the driving force remain the same.

For instance, when an elastic sheet deforms onto a wall prewetted by a thin viscous film, the dynamics of the advancing front is dictated by the local curvature of the interface [16,22]. This elastohydrodynamic relaxation is reminiscent of capillary spreading of a viscous drop onto a solid substrate [30–33]. Similar to capillary flows, elastohydrodynamic relaxation processes are not only limited to very thin prewetted films. In fact, an elastic sheet with zero spontaneous curvature but with an initial shape of a bump (Fig. 1) with a height much larger than the prewetted viscous film will relax towards a flat equilibrium state. Inevitably, the system must then crossover from a situation where the bump height is larger than the prewetted film height to a situation where instead the prewetted film becomes thicker than the bump. Here we investigate how the elastohydrodynamic leveling changes with the ratio between the bump height and the prewetted film thickness. In particular, are there different asymptotic regimes, and how does the system transition from one to another? At the nanoscale, thermal fluctuations are expected to contribute and may even dominate the dynamics [29,34–37], which we quantify in the leveling dynamics. To answer these questions, we combine numerical solutions of a mathematical model based on the lubrication theory [28] with scaling analysis and experiments.

II. MATHEMATICAL MODEL AND NUMERICAL PROCEDURE

We consider the system depicted in Fig. 1, where we focus on a system where any influence of gravity can be neglected, i.e., the bump height is smaller than the elasto-gravity length [8]. The film height is defined as $\hat{h}(x,t) = h(x,t) + \epsilon$, where $h(x,t)$ is the bump height measured from the height ϵ of the pre-wetted layer. Only situations where the bump height $h(x,t)$ is small compared with its horizontal extent and where the film slopes are small, i.e., $\partial\hat{h}(x,t)/\partial x \ll 1$, are considered. We describe the viscous flow between the plate and the solid substrate using lubrication theory [28]. When the initial deflection h_i of the elastic plate is small compared with its thickness d, we can neglect stretching and the pressure reduces to $p(x,t) = B\partial^4\hat{h}(x,t)/\partial x^4$, where $B = Ed^3/[12(1-\nu^2)]$ is the bending rigidity of the plate, E is the Young's modulus, and ν is Poisson's ratio [38]. In addition, the system is a spatially unconfined elastic sheet with the two lateral boundaries being free to move relative to the underlying fluid. Thus, the in-plane compression is suppressed, and bending stresses dominate the relaxation process regardless of the ratio d/h_i. By assuming incompressible flow and imposing no-slip conditions at the two solid substrates, and considering a one-dimensional geometry as there are no variations along the y direction, one obtains the governing equation for the evolution of the height profile (see, e.g., Ref. [8]),

$$\frac{\partial\hat{h}(x,t)}{\partial t} = \frac{\partial}{\partial x}\left[\frac{B}{12\mu}\hat{h}^3(x,t)\frac{\partial^5\hat{h}(x,t)}{\partial x^5} + \Gamma\hat{h}^{3/2}(x,t)\eta(x,t)\right], \tag{1}$$

where μ is the fluid's dynamic viscosity. At small scales, thermal fluctuations can also influence the dynamics, which is described by the last term of Eq. (1). This term mimics the stress generated by thermal fluctuations, originates from an additional symmetric random stress term in the Navier-Stokes equations, and is obtained by an integration in the z direction (for details see Refs. [29,39–41]). The noise term $\eta(x,t)$ is multiplied by a prefactor $\Gamma = \sqrt{k_\mathrm{B}T_\mathrm{A}/(6\mu b)}$ where k_B is the Boltzmann constant, T_A is the ambient temperature, b is the width of the plate along the y direction, and $\eta(x,t)$ is modeled as a spatiotemporal Gaussian white noise such that $\langle\eta(x,t)\rangle = 0$ and $\langle\eta(x,t)\eta(x',t')\rangle = \delta(x-x')\delta(t-t')$, where the $\langle\,\rangle$ symbols indicate average quantities. We nondimensionalize Eq. (1) by using $X = x/R_\mathrm{i}$, $\hat{H}(X,T) = \hat{h}(x,t)/h_\mathrm{i}$, $T = tBh_\mathrm{i}^3/(12\mu R_\mathrm{i}^6)$, and $\Theta(X,T) = \eta(x,t)[12\mu R_\mathrm{i}^7/(Bh_\mathrm{i}^3)]^{1/2}$. When $\Gamma = 0$, this nondimensionalization procedure gives us a parameter-free partial differential equation for $\hat{H}(X,T)$. When $\Gamma > 0$, the nondimensional number $N = [2k_\mathrm{B}T_\mathrm{A}R_\mathrm{i}^3/(Bh_\mathrm{i}^2 b)]^{1/2}$ appears as a prefactor in front of the stochastic term, and N^2 measures the ratio between thermal and bending energies. For the macroscopic system provided in our experiment and described in detail below, i.e., $T_A = 300$ K, $h_\mathrm{i} = 2.5$ μm, $R_\mathrm{i} = 20$ μm, $\mu = 10^4$ Pa s, and $B = 1.3\times10^{-12}$ N m we get the noise prefactor $\Gamma = 2.5\times10^{-13}$ m s$^{-1/2}$ and the energy ratio $N = 1.75\times10^{-6}$ which is well within the elastic-bending-dominated regime. However, a transition from a dominant elastohydrodynamic leveling to a dominant stochastic leveling would occur for a system with temperature $T_\mathrm{A} = 300$ K, membrane perturbation height $h_\mathrm{i} = 10$ nm, and radius $R_\mathrm{i} = 5$ μm for a bending modulus B in the range of 10–100 $k_\mathrm{B}T_\mathrm{A}$ where $k_\mathrm{B}T_\mathrm{A} = 4\times10^{-21}$ N m, which corresponds to N in the range 0–8 [29].

We solve the dimensionless version of Eq. (1) numerically by using a finite element method, and we split it into three coupled equations for the bump profile $H(X,T) = \hat{H}(X,T) - \epsilon/h_\mathrm{i}$, the linearized curvature $\partial^2H(X,T)/\partial X^2$, and the bending pressure $\partial^4H(X,T)/\partial X^4$. These fields are discretized with linear elements and solved by using Newton's method from the FEniCS library [42]. For the deterministic case $N = 0$, an adaptive time-stepping routine has been used with an upper time-step limit of $\Delta T = 0.001$ and a discretization in space $\Delta X \in [0.001; 0.01]$. For the stochastic case $N > 0$, we have used a constant time step $\Delta T = 0.001$, together with a discretization in space $\Delta X = 0.0025$. At $T = 0$ we impose the initial condition $H(X, T=0) = 1 - \tanh(50X^2)$. We further impose the following boundary conditions at the boundary $\partial\Omega$ of the numerical domain: $H(X\in\partial\Omega, T) = H(X\in\partial\Omega, 0)$, $\partial^2H(X\in\partial\Omega,T)/\partial X^2 = 0$, and $\partial^4H(X\in\partial\Omega,T)/\partial X^4 = 0$. The noise $\Theta(X,T)$ is introduced independently at each discrete position and time step by using the "random" class with the "randn" Gaussian subclass from the NUMPY library [43], with zero mean

and a variance $1/(\Delta X\,\Delta T)$. We avoid negative values of $\hat{H}(X,T)$ (that might occur in the stochastic case due to the fluctuations), by imposing that, when $\hat{H}(X,T) < 10^{-6}$, it is put back to 10^{-6} as in Refs. [34,36]. To verify the predictions of Eq. (1), we construct an experimental setup which is described in the following section.

III. EXPERIMENTAL PROCEDURE

The experimental setup is composed of a fiber of polystyrene (PS) with a glass-transition temperature $T_{g,\,PS} \approx 100\,^{\circ}$C deposited on a film of the same polymer supported on a silicon (Si) substrate. These samples are capped by a thin sheet of polysulfone (PSU) with $T_{g,\,PSU} \approx 180\,^{\circ}$C. Sample preparation is carried out as follows: PS fibers (with number-averaged molecular weight $M_n = 15.8$ kg/mol and polydispersity index PDI $= 1.05$, Polymer Source Inc., Canada) are pulled from the melt at 175 °C by using a glass rod. Thin PS films are spin casted from a toluene solution onto 10×10 mm^2 Si substrates, leading to a thickness of 25 to 380 nm, as measured by using ellipsometry (Accurion, EP3). The films are annealed at 110 °C for at least 12 hours in vacuum to remove residual solvent and relax residual stresses. The PS fibers are then transferred onto the PS films and the ensemble is heated briefly above $T_{g,\,PS}$. The heating allows the PS to flow, thereby resulting in a bump. Thin PSU films ($M_n \approx 22$ kg/mol, Sigma-Aldrich) are prepared by spin casting from a cyclohexanone solution onto freshly cleaved mica substrates (Ted Pella, USA). The PSU films have a thickness of ≈160 nm, as measured by using ellipsometry, and are annealed in vacuum at 200 °C for at least 12 hours. The PSU films are floated on water and then transferred onto a supporting apparatus (described previously [44]), held only by the film edges. These freestanding films can be relaxed to an unstrained state, ensuring no in-plane tension. The PSU films are finally transferred onto the PS sample. The part of the PSU film at the edges of the Si wafer was then removed by using a scalpel blade prior to annealing. This was done to ensure slippage at the boundary between the PSU film and liquid PS layer, thus rendering the relaxation bending-dominated, as discussed above.

After preparation, the samples were annealed on a hotstage (Linkam, UK) at 130 °C, which is above $T_{g,\,PS}$ but below $T_{g,\,PSU}$. Hence, the PS becomes a viscous liquid while the capping PSU film remains an elastic solid, thus realizing the system illustrated in Fig. 1. The height profile is imaged during annealing by using optical microscopy with a red laser line filter ($\lambda = 632.8$ nm, Newport, USA), which creates interference fringes in the region of the bump, as shown in Fig. 2(a), due to the light that is reflected from the Si substrate. It is clear from these fringes that the initial fiber and resulting flow are one dimensional over length scales that are many times the width of the perturbation itself. Each interference fringe corresponds to a change in height of $\lambda/(4n)$, where $n \approx 1.57$ is the average index of refraction of the two polymers that make up the sample ($n_{PS} = 1.53$ and $n_{PSU} = 1.61$). This allows the bump profile $h(x,t)$ to be reconstructed by fitting a polynomial to the fringe data, as shown in Fig. 2(b). Such profiles can then be used to track the leveling dynamics, and to extract in particular the evolution of the height $h_0(t)$ of the bump with time for various initial geometries.

IV. RESULTS

A. Elastohydrodynamic leveling

We first start by investigating the elastohydrodynamic leveling in the absence of thermal fluctuations ($N = 0$). In Fig. 3 we show the numerical solutions of the dimensionless version of Eq. (1) for $N = 0$ and we can see that the aspect ratio h_i/ϵ controls both the timescale for leveling and the detailed features of the height profile. The smaller h_i/ϵ, the faster the dimensionless leveling process. Also, the dip created near the advancing front of the perturbation is enhanced both in magnitude and lateral extent for smaller h_i/ϵ. We remark that, for each initial aspect ratio, there is a transition period of a few numerical time steps preceding the onset of the leveling process. This part of the data is not included in Fig. 4 because it is considered to depend on the initial condition, but does not

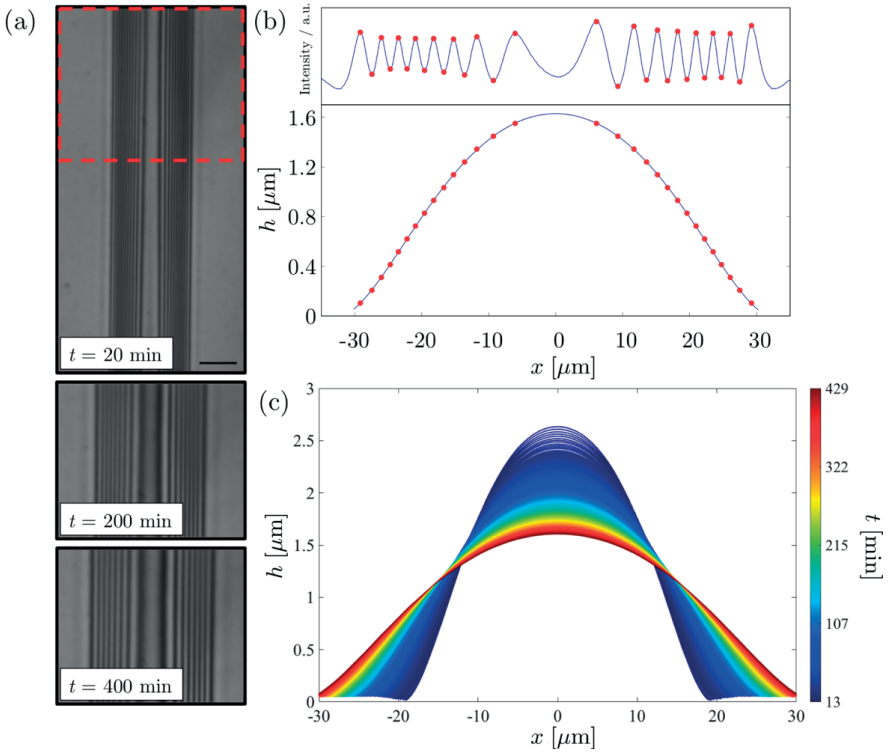

FIG. 2. (a) Typical optical microscopy images showing the temporal evolution of the interference fringes due to the liquid bump capped by the elastic plate (20 μm scale bar). The image at 20 minutes is uncropped, showing the invariance in the y direction, while the later images are cropped at the red box. (b) Intensity profile (averaged along the y direction) of the bump at a given time t, and corresponding reconstructed bump profile at 400 minutes. (c) Temporal evolution of the bump profile.

influence the later dynamics. For $h_i/\epsilon = 43$, the numerical height profiles are further compared with our experiments, which are found to be in good agreement. We recall here that the elastic plate is floating on the liquid film and has edges that are free to move. Therefore, the pressure contribution from bending still largely dominates any contribution from stretching and Eq. (1) is still valid.

We now turn to a scaling analysis of Eq. (1) for $N = 0$. When $h_0(t)/\epsilon \ll 1$, the equation can be linearized and reduces to $12\mu\partial h/\partial t = B\epsilon^3\partial^6 h/\partial x^6$ as $\hat{h}(x,t) = h(x,t) + \epsilon$ and we deduce the long-term scaling for the temporal evolution of the horizontal length of the bump: $R(t) \sim [B\epsilon^3 t/(12\mu)]^{1/6}$. Since there is area conservation in the (x,z) plane, we assume $R(t)h_0(t)$ to be constant, that is evaluated to $R_i h_i$ at $t = 0$. By combining these scaling relations we get for $h_0(t)/\epsilon \ll 1$,

$$\frac{h_0(t)}{\epsilon} \sim \left(\frac{\tau}{t}\right)^{1/6}, \tag{2}$$

where $\tau = 12\mu h_i^6 R_i^6/(B\epsilon^9)$ is the characteristic timescale for the bending-driven leveling dynamics. Because we operate within the regime where bending dominates over stretching, a similar result is obtained by considering the force balance between the viscous and bending forces [18]. Also, if we include isotropic stretching due to clamped boundaries, a similar scaling law appears, but now with an additional logarithmic term, $R(t) \sim [t/\ln(t)]^{1/6}$ [19]. However, when $h_0(t)/\epsilon \gg 1$ we must match the curvature of a traveling-wave solution localized near the advancing front with the quasistatic solution to obtain the correct scaling [22], i.e., constant pressure in the bump, leading to [29]

$$\frac{h_0(t)}{\epsilon} \sim \left(\frac{\tau}{t}\right)^{2/17}. \tag{3}$$

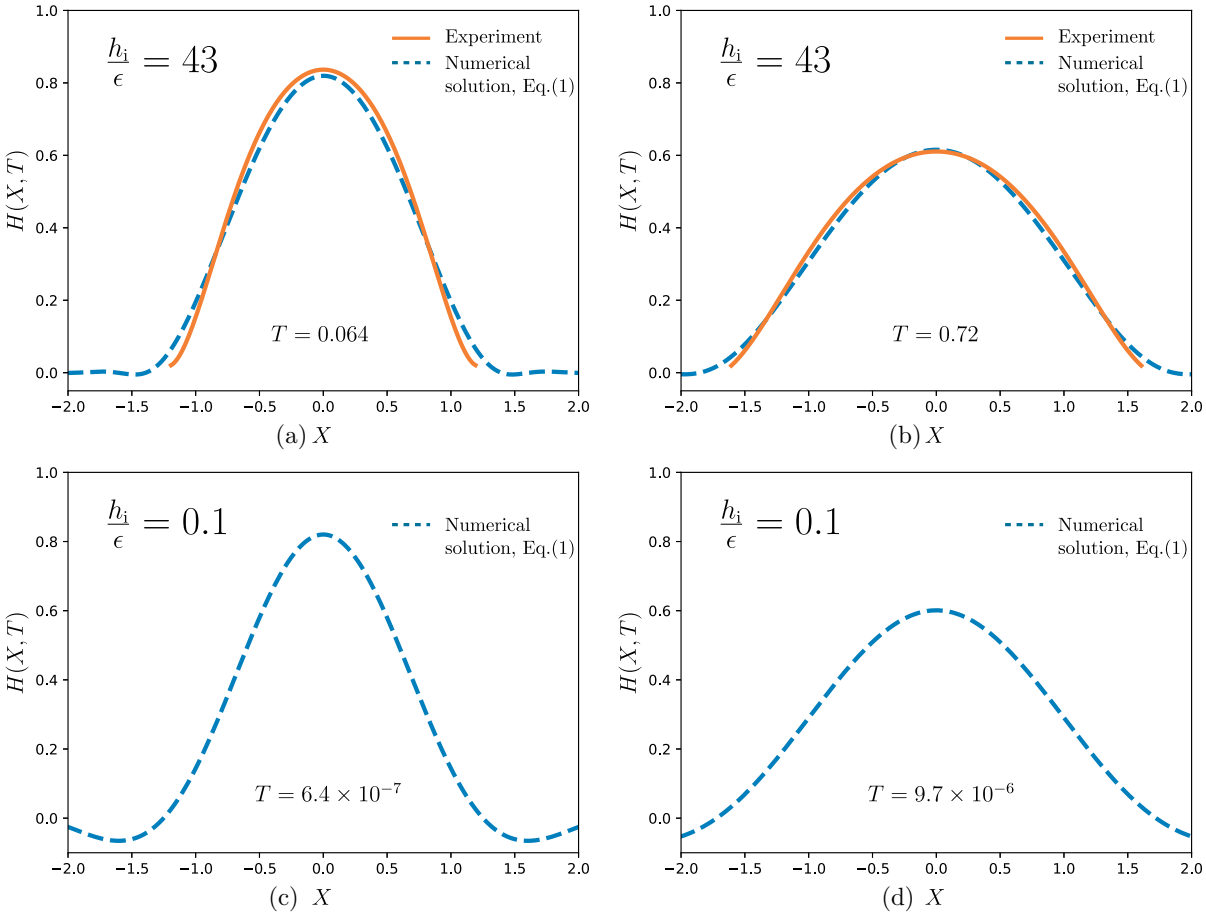

FIG. 3. (a), (b) Bump-height profiles for an initial aspect ratio $h_i/\epsilon = 43$, from a numerical solution of Eq. (1) and an experiment at two dimensionless times T as indicated, which correspond respectively to $t = 37$ min and $t = 416$ min. The geometrical parameters are $h_i = 2.9$ μm, $R_i = 16.5$ μm, and $\epsilon = 67$ nm. To account for the experimental uncertainties in the geometrical parameters, the experimental time t is divided by a free-fitting factor $\alpha = 0.13$. Note that, specifically for these figures, the initial condition for the numerical solution was fixed by a curve fitting of the actual experimental profile at $t = 13$ min. (c), (d) Bump-height profiles for an initial aspect ratio $h_i/\epsilon = 0.1$ from a numerical solution of Eq. (1) at two dimensionless times T, as indicated, chosen so that the central heights $H(X = 0, T)$ match those in the top row.

By balancing the two asymptotic predictions above, we expect the crossover between them to occur around $t/\tau \approx 1$. In addition, these asymptotic regimes suggest that $h_0(t)/\epsilon$ is essentially a function of t/τ only, independent of the value of h_i/ϵ.

To test our scaling predictions, we compute numerical solutions of the dimensionless version of Eq. (1) for $N = 0$, with $h_i/\epsilon \in [10^{-2}, 10^3]$, and extract $h_0(t)/\epsilon$ as a function of t/τ. These numerical results are plotted in Fig. 4 and compared with the experimental data. For each sample, the experimental data are matched to the numerical data through one fitting parameter α in front of the timescale τ. The values of the fluid viscosity and elastic Young's modulus are highly sensitive to the temperature in the experiments, and we estimate them to be $\mu \approx 10^4$ Pa s [45,46] and $E \approx 2.6$ GPa [47], respectively. Since all experiments were carried out at the same temperature and with the same polymer, sample-to-sample variations in τ result only from uncertainties in the geometrical parameters h_i, R_i, d, and ϵ. The α values obtained are 0.13, 0.7, and 1.3 for the three samples and each of these values are reasonably close to unity. More importantly, the sample-to-sample variations in α do not exceed a factor of ten, which is well within the expected relative error arising from the high sensitivity of τ to the geometrical parameters. The general agreement between the experimental data and the numerical predictions is good, over about five

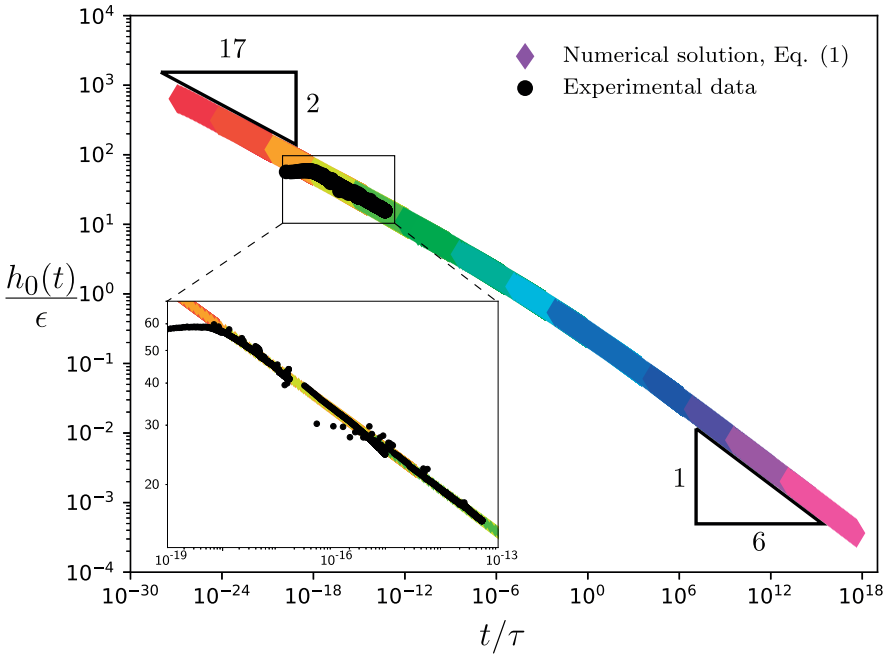

FIG. 4. Nondimensional bump height as a function of dimensionless time in the bending case, for various initial values of $h_i/\epsilon \in [10^{-2}; 10^3]$. The colored diamond-shaped markers are rescaled data points from the numerical solutions of the dimensionless version of Eq. (1) with $N = 0$, and the black circle-shaped markers are scaled experimental data points. The exponents of the two asymptotic regimes of Eqs. (2) and (3) are indicated with triangles. The inset provides a zoom in the region containing the experimental data for the three samples, with initial aspect ratios $h_i/\epsilon = 30$, 43, 56, corresponding respectively to $\epsilon = 50$, 67, 26 nm; $h_i = 1.52$, 2.9, 1.48 μm; and $R_i = 9.6$, 16.5, 9.9 μm. The uncertainties in all experimental length scales are about 5%. To compensate for those, the characteristic time τ for each sample is multiplied by a free-fitting factor $\alpha = 0.7$, 0.13, and 1.3, respectively.

orders of magnitude in t/τ. The systematic early time tail in the experimental data might be attributed to the initial compressive thermal stresses in the elastic layer, which arise due to the rapid heating of the samples from room temperature to $T = 130\,^{\circ}$C, which relax prior to leveling and the time needed for the initial shape to enter the asymptotic regime.

The master curve in Fig. 4 confirms that $h_0(t)/\epsilon$ is a function of t/τ. Furthermore, the two scaling regimes predicted above are indeed present, with prefactors close to unity, and the crossover between the two being located near $t/\tau \approx 1$ as predicted. Any bump that initially starts in a thin prewetted film regime $h_0(t)/\epsilon \gg 1$ will eventually cross over to a thick-film regime $h_0(t)/\epsilon \ll 1$, with the corresponding power laws in time. As a final remark, a similar combination (not included here) of numerical simulations and scaling analysis can be performed for an axisymmetric geometry, leading to $h_0(t) \sim t^{-2/11}$ for $h_i/\epsilon \gg 1$, and $h_0(t) \sim t^{-1/3}$ for $h_i/\epsilon \ll 1$.

B. Stochastic leveling

Next we investigate the leveling process when it is dominated by thermal fluctuations ($N > 0$). As shown in Fig. 5, the numerical solutions suggest that the aspect ratio h_i/ϵ is again essential, because it sets the timescale for leveling where the smaller h_i/ϵ, the faster the dimensionless leveling process. Moreover, by comparison with the deterministic ($N = 0$) case in Fig. 3, the stochastic ($N > 0$) profiles exhibit spatiotemporal fluctuations and adopt different average shapes and leveling dynamics.

To go further, we propose a scaling analysis of Eq. (1), inspired by Ref. [32]. We consider specifically the $N \gg 1$ limit, for which the thermal fluctuations are the dominant driving contribution to the dynamics and we assume that we can neglect the bending term so that Eq. (1) reduces

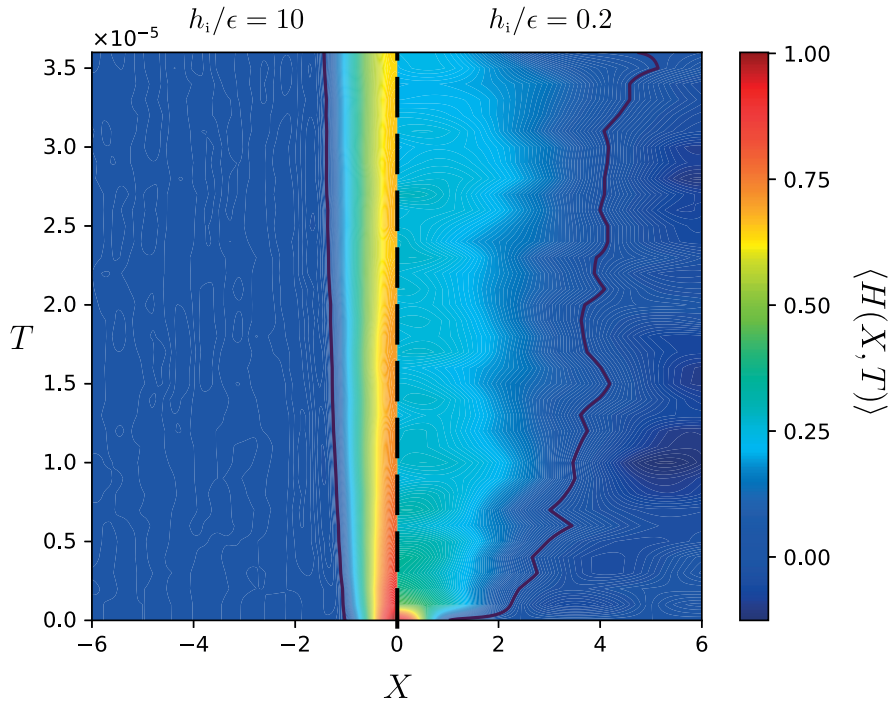

FIG. 5. Contour plot of the dimensionless bump-height profile $\langle H(X,T)\rangle$ as a function of both the dimensionless position X and time T, as obtained from numerical solutions of the dimensionless version (see text) of Eq. (1), with $N = 5$, and for $h_i/\epsilon = 10$ (left) or $h_i/\epsilon = 0.2$ (right). The thick solid lines indicate $\langle H(X,T)\rangle = 0.03$ as an arbitrary reference.

to $\partial h/\partial t = \Gamma\partial[(\epsilon + h)^{3/2}\eta]/\partial x$. We consider the average quantities $\langle h_0(t)\rangle$ and $\langle R(t)\rangle$, where we invoke the $\sim(tx)^{-1/2}$ scaling [34] for the root mean square value of the averaged noise over a space interval x and a time interval t. By assuming that the average area conservation in the (x, z) plane can be expressed as $\langle h_0(t)\rangle\langle R(t)\rangle \sim h_i R_i$, we get

$$\frac{\langle h_0(t)\rangle}{\epsilon}\left[1 + \frac{\langle h_0(t)\rangle}{\epsilon}\right]^3 \sim \frac{\tau_\Gamma}{t}, \tag{4}$$

where $\tau_\Gamma = 6\mu h_i^3 R_i^3 b/(k_B T_A \epsilon^4)$ is the characteristic timescale for the stochastic leveling dynamics. Interestingly, Eq. (4) describes a complete crossover between two asymptotic regimes in the stochastic leveling dynamics: for $\langle h_0(t)\rangle/\epsilon \gg 1$, we obtain $\langle h_0(t)\rangle/\epsilon \sim (\tau_\Gamma/t)^{1/4}$, and thus we recover $\langle h_0(t)\rangle \sim t^{-1/4}$ [34], while for $\langle h_0(t)\rangle/\epsilon \ll 1$, we get $\langle h_0(t)\rangle/\epsilon \sim \tau_\Gamma/t$. We expect the crossover between the two asymptotic regimes to occur around $\langle h_0(t)\rangle/\epsilon \approx 1$, i.e., around $t/\tau \approx 1/8$.

To test the prediction in Eq. (4), we compute the numerical solution of the dimensionless version of Eq. (1) for $5 \leqslant N \leqslant 8$, with $h_i/\epsilon \in [10^{-1}, 10^2]$. By averaging over a minimum of 30 realizations, we can extract $\langle h_0(t)\rangle/\epsilon$ as a function of t/τ_Γ, and the results are plotted in Fig. 6. The data from the numerical solutions are in good agreement with Eq. (4) for all $\langle h_0(t)\rangle/\epsilon$ and with no adjustable parameters. Our results highlight that Eq. (4) gives an accurate prediction of the stochastic leveling dynamics and show that the missing prefactor is close to unity. Finally, in order to further highlight the underlying self-similarity associated with each of the two asymptotic regimes, the insets of Fig. 6 show the corresponding bump-height profiles rescaled according to Eq. (4). In each asymptotic regime the height profiles collapse onto a universal shape which confirms the overall self-similarity in the leveling dynamics.

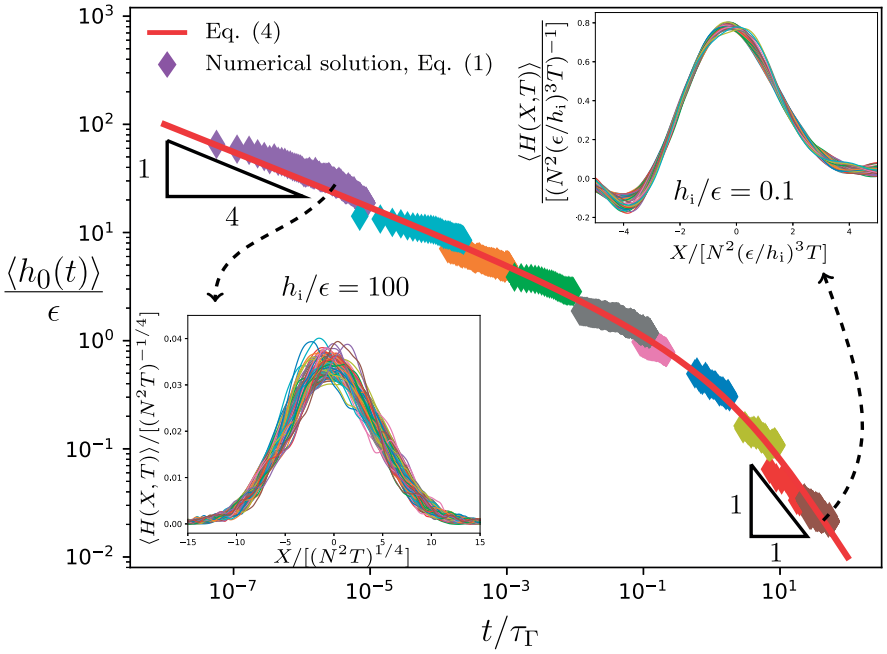

FIG. 6. Nondimensional bump height as a function of dimensionless time in the stochastic leveling dynamics, for different initial values of $h_i/\epsilon \in [10^{-1}, 10^2]$. The colored diamond-shaped markers are rescaled data points from the numerical solutions of Eq. (1) with $5 \leqslant N \leqslant 8$. Each data set is an average from a minimum of 30 numerical solutions. The solid red line corresponds to Eq. (4) with a prefactor of order unity. The insets show rescaled bump-height profiles for $h_i/\epsilon = 100$ with $T \in [1, 10] \times 10^{-3}$ (lower left) and for $h_i/\epsilon = 0.1$ with $T \in [4, 4.6] \times 10^{-3}$ (upper right).

V. CONCLUSION

We have described the elastohydrodynamic and stochastic leveling of an elastic plate placed atop a viscous film. By combining numerical solutions, scaling analysis, and experiments, we identified various canonical regimes. Our results highlight the importance of the driving mechanism, either by elastic bending of the plate or by thermal fluctuations, and the influence of the aspect ratio of bump height to film height. For each of these two driving mechanisms, a crossover between two distinct asymptotic regimes is controlled by the aspect ratio. These findings can be helpful to explain elastohydrodynamic leveling dynamics found in biological, engineering, or geological processes.

ACKNOWLEDGMENTS

The financial support by the Research Council of Norway (project grant 263056), the Natural Sciences and Engineering Research Council of Canada, and the Joliot Chair of ESPCI Paris is gratefully acknowledged. The authors also thank Tak Shing Chan, Miroslav Kuchta, Corentin Mailliet, René Ledesma-Alonso, Maxence Arutkin, Elie Raphaël, Howard Stone, Pauline Olive, Katelyn Dixon, Paul Fowler, Mark Ilton and David Dean for interesting discussions and preliminary works in different geometries.

[1] N. J. Balmforth, R. V. Craster, and A. C. Rust, Instability in flow through elastic conduits and volcanic tremor, J. Fluid Mech. **527**, 353 (2005).

[2] C. Michaut, Dynamics of magmatic intrusions in the upper crust: Theory and applications to laccoliths on Earth and the Moon, J. Geophys. Res. **116**, B05205 (2011).

[3] T. V. Ball and J. A. Neufeld, Static and dynamic fluid-driven fracturing of adhered elastica, Phys. Rev. Fluids **3**, 074101 (2018).
[4] L. E. Bilston, D. F. Fletcher, A. R. Brodbelt, and M. A. Stoodley, Arterial pulsation-driven cerebrospinal fluid flow in the perivascular space: A computational model, Comput. Methods Biomech. Biomed. Eng. **6**, 235 (2003).
[5] D. Takagi and N. J. Balmforth, Peristaltic pumping of viscous fluid in an elastic tube, J. Fluid Mech. **672**, 196 (2011).
[6] R. Borcia, M. Bestehorn, S. Uhlig, M. Gaudet, and H. Schenk, Liquid pumping induced by transverse forced vibrations of an elastic beam: A lubrication approach, Phys. Rev. Fluids **3**, 084202 (2018).
[7] D. A. Sanchez, Z. Dai, P. Wang, A. Cantu-Chavez, C. J. Brennan, R. Huang, and N. Lu, Mechanics of spontaneously formed nanoblisters trapped by transferred 2D crystals, Proc. Natl. Acad. Sci. USA **115**, 7884 (2018).
[8] A. E. Hosoi and L. Mahadevan, Peeling, Healing, and Bursting in a Lubricated Elastic Sheet, Phys. Rev. Lett. **93**, 137802 (2004).
[9] R. Huang and Z. Suo, Wrinkling of a compressed elastic film on a viscous layer, J. Appl. Phys. **91**, 1135 (2002).
[10] T. T. Al-Housseiny, I. C. Christov, and H. A. Stone, Two-Phase Fluid Displacement and Interfacial Instabilities Under Elastic Membranes, Phys. Rev. Lett. **111**, 034502 (2013).
[11] I. J. Hewitt, N. J. Balmforth, and J. R. De Bruyn, Elastic-plated gravity currents, Eur. J. Appl. Math. **26**, 1 (2015).
[12] A. Tulchinsky and A. D. Gat, Transient dynamics of an elastic Hele-Shaw cell due to external forces with application to impact mitigation, J. Fluid Mech. **800**, 517 (2016).
[13] S. B. Elbaz and A. D. Gat, Axial creeping flow in the gap between a rigid cylinder and a concentric elastic tube, J. Fluid Mech. **806**, 580 (2016).
[14] M. Arutkin, R. Ledesma-Alonso, T. Salez, and E. Raphaël, Elastohydrodynamic wake and wave resistance, J. Fluid Mech. **829**, 538 (2017).
[15] A. Juel, D. Pihler-Puzović, and M. Heil, Instabilities in blistering, Annu. Rev. Fluid Mech. **50**, 691 (2018).
[16] M. Rivetti, V. Bertin, T. Salez, C. Y. Hui, C. Linne, M. Arutkin, H. Wu, E. Raphaël, and O. Bäumchen, Elastocapillary levelling of thin viscous films on soft substrates, Phys. Rev. Fluids **2**, 094001 (2017).
[17] E. Cerda and L. Mahadevan, Geometry and Physics of Wrinkling, Phys. Rev. Lett. **90**, 074302 (2003).
[18] H. Vandeparre, S. Gabriele, F. Brau, C. Gay, K. K. Parker, and P. Damman, Hierarchical wrinkling patterns, Soft Matter **6**, 5751 (2010).
[19] O. Kodio, I. M. Griffiths, and D. Vella, Lubricated wrinkles: Imposed constraints affect the dynamics of wrinkle coarsening, Phys. Rev. Fluids **2**, 014202 (2017).
[20] R. Bernal, C. Tassius, F. Melo, and J. C. Géminard, Elastic response and wrinkling onset of curved elastic membranes subjected to indentation test, Eur. Phys. J. E **34**, 13 (2011).
[21] F. Box, D. O'Kiely, O. Kodio, M. Inizan, A. A. Castrejón-Pita, and D. Vella, Dynamics of wrinkling in ultrathin elastic sheets, Proc. Natl. Acad. Sci. USA **116**, 20875 (2019).
[22] J. R. Lister, G. G. Peng, and J. A. Neufeld, Viscous Control of Peeling an Elastic Sheet by Bending and Pulling, Phys. Rev. Lett. **111**, 154501 (2013).
[23] M. Berhanu, A. Guérin, S. C. du Pont, F. Raoult, R. Perrier, and C. Michaut, Uplift of an elastic membrane by a viscous flow, Phys. Rev. E **99**, 043102 (2019).
[24] A. Carlson and L. Mahadevan, Similarity and singularity in adhesive elastohydrodynamic touchdown, Phys. Fluids **28**, 011702 (2016).
[25] W. W. Zhang and J. R. Lister, Similarity solutions for van der Waals rupture of a thin film on a solid substrate, Phys. Fluids **11**, 2454 (1999).
[26] D. Pihler-Puzović, A. Juel, G. G. Peng, J. R. Lister, and M. Heil, Displacement flows under elastic membranes. Part 1. Experiments and direct numerical simulations, J. Fluid Mech. **784**, 487 (2015).
[27] M. Heil and A. L. Hazel, Fluid-structure interaction in internal physiological flows, Annu. Rev. Fluid Mech. **43**, 141 (2011).
[28] G. K. Batchelor, *An Introduction to Fluid Dynamics* (Cambridge University Press, New York, 2000).
[29] A. Carlson, Fluctuation assisted spreading of a fluid filled elastic blister, J. Fluid Mech. **846**, 1076 (2018).

[30] L. H. Tanner, The spreading of silicone oil drops on horizontal surfaces, J. Phys. D: Appl. Phys. **12**, 1473 (1979).
[31] P. G. De Gennes, Wetting: Statics and dynamics, Rev. Mod. Phys. **57**, 827 (1985).
[32] S. L. Cormier, J. D. McGraw, T. Salez, E. Raphaël, and K. Dalnoki-Veress, Beyond Tanner's Law: Crossover Between Spreading Regimes of a Viscous Droplet on an Identical Film, Phys. Rev. Lett. **109**, 154501 (2012).
[33] N. Bergemann, A. Juel, and M. Heil, Viscous drops on a layer of the same fluid: From sinking, wedging and spreading to their long-time evolution, J. Fluid Mech. **843**, 1 (2018).
[34] B. Davidovitch, E. Moro, and H. A. Stone, Spreading of Viscous Fluid Drops on a Solid Substrate Assisted by Thermal Fluctuations, Phys. Rev. Lett. **95**, 244505 (2005).
[35] V. Démery and D. S. Dean, Perturbative path-integral study of active- and passive-tracer diffusion in fluctuating fields, Phys. Rev. E **84**, 011148 (2011).
[36] S. Nesic, R. Cuerno, E. Moro, and L. Kondic, Fully nonlinear dynamics of stochastic thin-film dewetting, Phys. Rev. E **92**, 061002 (2015).
[37] S. Marbach, D. S. Dean, and L. Bocquet, Transport and dispersion across wiggling nanopores, Nat. Phys. **14**, 1108 (2018).
[38] L. D. Landau and E. M. Lifshitz, *Course of Theoretical Physics Vol 7: Theory and Elasticity* (Pergamon Press, Oxford, 1959).
[39] G. Grün, K. Mecke, and M. Rauscher, Thin-film flow influenced by thermal noise, J. Stat. Phys. **122**, 1261 (2006).
[40] M. A. Durán-Olivencia, R. S. Gvalani, S. Kalliadasis, and G. A. Pavliotis, Instability, rupture and fluctuations in thin liquid films: Theory and computations, J. Stat. Phys. **174**, 579 (2019).
[41] S. Nesic, R. Cuerno, E. Moro, and L. Kondic, Dynamics of thin fluid films controlled by thermal fluctuations, Eur. Phys. J. Spec. Top. **224**, 379 (2015).
[42] A. Logg, K. A. Mardal, and G. Wells, *Automated Solution of Differential Equations by the Finite Element Method: The FEniCS Book* (Springer Science & Business Media, Berlin, 2012), Vol. 84.
[43] T. Oliphant, *NumPy: A guide to NumPy* (Trelgol Publishing, 2006).
[44] R. D. Schulman, J. F. Niven, M. A. Hack, C. DiMaria, and K. Dalnoki-Veress, Liquid dewetting under a thin elastic film, Soft Matter **14**, 3557 (2018).
[45] J. D. McGraw, T. Salez, O. Bäumchen, E. Raphaël, and K. Dalnoki-Veress, Self-Similarity and Energy Dissipation in Stepped Polymer Films, Phys. Rev. Lett. **109**, 128303 (2012).
[46] M. Ilton, M. M. P. Couchman, C. Gerbelot, M. Benzaquen, P. D. Fowler, H. A. Stone, E. Raphaël, K. Dalnoki-Veress, and T. Salez, Capillary Leveling of Freestanding Liquid Nanofilms, Phys. Rev. Lett. **117**, 167801 (2016).
[47] *Springer Handbook of Condensed Matter and Materials Data*, edited by W. Martienssen and H. Warlimont (Springer, New York, 2005).

Paper III

Capillary deformation of ultrathin glassy polymer films by air nanobubbles

Shuai Ren, Christian Pedersen, Andreas Carlson, Thomas Salez, Yuliang Wang

Published in Physical Review Research 2, 043166 (2020). DOI: https://doi.org/10.1103/PhysRevResearch.2.043166.

III

Capillary deformation of ultrathin glassy polymer films by air nanobubbles

Shuai Ren [1,*] Christian Pedersen,[2,*] Andreas Carlson [2] Thomas Salez [3,4,†] and Yuliang Wang [1,5,‡]

[1]*School of Mechanical Engineering and Automation, Beihang University, 37 Xueyuan Road, Haidian District, Beijing 100191, China*

[2]*Mechanics Division, Department of Mathematics, University of Oslo, 0316 Oslo, Norway*

[3]*Univ. Bordeaux, CNRS, LOMA, UMR 5798, F-33405 Talence, France*

[4]*Global Station for Soft Matter, Global Institution for Collaborative Research and Education, Hokkaido University, Sapporo, Hokkaido 060-0808, Japan*

[5]*Beijing Advanced Innovation Center for Biomedical Engineering, Beihang University, 37 Xueyuan Road, Haidian District, Beijing 100191, China*

(Received 5 March 2020; accepted 14 September 2020; published 30 October 2020)

Confined glasses and their anomalous interfacial rheology raise important questions in fundamental research and numerous practical applications. In this work, we study the influence of interfacial air nanobubbles on the free surface of ultrathin high-molecular-weight glassy polystyrene films immersed in water, in ambient conditions. In particular, we reveal the counterintuitive fact that a soft nanobubble is able to deform the surface of a rigid glass, forming a nanocrater with a depth that increases with time. By combining *in situ* atomic-force-microscopy measurements and a modified lubrication model for the liquidlike layer at the free surface of the glass, we demonstrate that the capillary pressure in the nanobubble together with the liquidlike layer at the free surface of the glass determine the spatiotemporal growth of the nanocraters. Finally, from the excellent agreement between the experimental profiles and the numerical solutions of the governing glassy thin-film equation, we are able to precisely extract the surface mobility of the glass. In addition to revealing and quantifying how surface nanobubbles deform immersed glasses, until the latter eventually dewet from their substrates, our work provides a novel, precise, and simple measurement of the surface nanorheology of glasses.

DOI: 10.1103/PhysRevResearch.2.043166

I. INTRODUCTION

The glass transition has been a major enigma in solid-state physics [1] for almost a century, leading to an important literature for the bulk case [2]. Besides a hypothetical underlying phase transition, the tremendous dynamical slowing down of glass-forming supercooled liquids has been attributed to molecular caging, and the associated requirement for cooperative relaxation [3] in a region of a certain cooperative size [4].

The quest for the latter observable, and its possible divergence, led to an alternative strategy: the study of glasses in confinement [5–7]. In the particular case of thin polymer films, anomalies have been reported, such as reductions of the apparent glass-transition temperature T_g at small film thicknesses [8,9], where the presence of free surfaces played an important role [10]. Furthermore, space-dependent T_g values were inferred from local measurements [11]. Besides, the free surface of a polymer glass was discovered to be much more mobile than the bulk, which was attributed to the existence of a nanometric liquidlike superficial layer capable to flow under external constraints [12–17], or equivalently for small enough molecules to undergo surface diffusion [18–20] as in crystals [21], which could even lead to striking engulfment phenomena [22]. The previous Stokes-Einstein-like equivalence between surface flow and surface diffusion in the mobile layer was shown to be eventually broken for long-enough surface polymer chains due to their anchoring into the bulk matrix [23], and ultimately the commensurability of their typical size with the sample thickness itself [24,25]. Finally, among other interesting properties, spatial heterogeneities were associated with the dynamics of thin glassy polymer films [26]. To rationalize these observations, various numerical approaches [27,28] and theoretical models [29–34] have been proposed, but a unifying picture is still at large.

In this work, we study the influence of air nanobubbles spontaneously created at the free surface of ultrathin high-molecular-weight glassy polystyrene (PS) films when immersed in water, and in ambient conditions [35,36]. In contrast to the bubble-inflation technique used for freestanding viscoelastic membranes [37], there is here no need for an externally driven inflation, and the glassy films are supported onto rigid silicon wafers and thus much less compliant. The nanobubbles are gaseous air domains with nanometric height and width. As a consequence of these small sizes, and from the Young-Laplace equation, the pressure inside the bubble

*These authors contributed equally to this work.
†thomas.salez@u-bordeaux.fr
‡wangyuliang@buaa.edu.cn

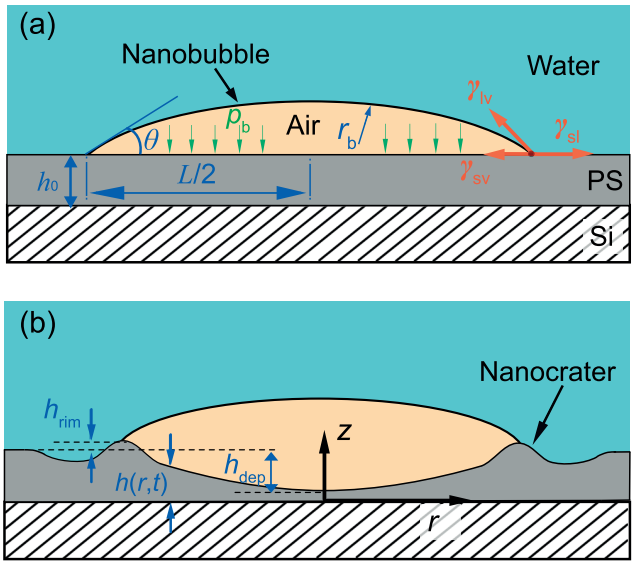

FIG. 1. Schematic of the bubble-PS film interaction. (a) An air nanobubble spontaneously forms at the PS-water interface right after immersion of the glassy PS sample in water. (b) Subsequently, a nanocrater appears beneath the nanobubble, and grows with time, as the liquidlike layers at both PS-fluid interfaces flow due to the capillary pressure gradient.

can reach up to ∼10 bar, which—despite being much smaller than the yield stress of the bulk glass—can lead to an external driving force for the flow of the liquidlike layer at the free surface of the glass. Consequently, a nanoscopic crater is formed underneath the bubble, and grows in size with time, as observed using an atomic-force microscope (AFM). The latter observations are discussed in the context of a modified lubrication model for the capillary-driven flow of the liquidlike layer at the free surface of the glassy film, under an external driving force. The excellent agreement between the experimental AFM profiles and the numerical solutions of the axisymmetric glassy thin-film equation yields a novel, precise, and simple measurement of the surface mobility of glasses. The value found for the latter is compared to values in the literature, and discussed in terms of polymer entanglements and anchoring effects in confinement. Finally, the model predicts a dewetting scenario for ultrathin polymer films, which might have important practical consequences.

II. EXPERIMENTAL SETUP

A schematic representation of the bubble-PS film interaction is shown in Fig. 1, where we define the bubble's contact diameter L, the bubble's radius of curvature r_b, the equilibrium contact angle θ, and the initial PS film thickness h_0. Note that L, r_b, and θ are related through volume conservation. According to the Young-Laplace equation, the pressure inside the bubble reads $p_b = p_{am} + 2\gamma_{lv}/r_b$, where γ_{lv} is the water-air surface tension and p_{am} is the ambient water pressure. In the following, we will quantify how the capillary pressure gradient can lead to the deformation of the glassy PS film and to the spatiotemporal evolution of the PS nanocrater. The latter is characterized by its depth h_{dep} and rim height h_{rim}.

Ultrathin PS films with three different thicknesses $h_0 \in \{2.8 \pm 0.6, 4.9 \pm 0.6, 7.1 \pm 0.8\}$ nm were prepared by spincoating a solution of PS (Sigma-Aldrich) in toluene onto a silicon wafer, at different toluene mass fractions $\{0.07, 0.10, 0.08\}$ wt% and rotational speeds of $\{1200, 1200, 1000\}$ rpm, respectively. The thicknesses of the PS films were measured by a scratching method [38]. The molecular weight of PS is about 350 kg/mol. After spincoating, the PS films were baked inside an oven at a temperature of 45°C for 4 h, to evaporate the remaining toluene. Here, we applied the temperature-exchange method to generate nanobubbles: cold deionized (DI) water at about 4°C was deposited on the PS films at about 30°C by a glass syringe. Upon immersion, nanobubbles were spontaneously nucleated.

An AFM (Resolve, Bruker, USA) in tapping mode was used to image the samples both in air and water. A silicon NSC36/Al BS cantilever (MikroMasch) with a tip radius <8 nm and a quoted stiffness of 1.0 N/m was used. The measured resonance frequencies of the cantilever in air and water were about 76 and 23 kHz, respectively. To minimize the force applied on the nanobubbles and sample surfaces, the setpoint for imaging was set to be only 95%–97% of the free amplitude. While imaging in air and water, the resonance frequencies were selected as the driving ones. The samples were scanned at a rate of 1.5 Hz with a scan angle of 0°.

III. RESULTS AND DISCUSSION

Figure 2(a) shows a typical AFM image of the PS film in air with a thickness $h_0 = 4.9 \pm 0.6$ nm. The root-mean-squared roughness is about 0.22 nm. After immersion in deionized (DI) water at room temperature, nanobubbles with diameters ranging from 30 to 100 nm spontaneously nucleated [Fig. 2(b)] at the PS-water interface [39]. The PS sample was kept in water for $t_b \approx 240$ min, before the water was removed and the sample surface was dried in air for $t - t_b \approx 250$ min. The same area of the sample was then scanned again with the AFM, as shown in Fig. 2(c). One observes the existence of nanocraters into the PS film. These nanocraters were generated at the exact same locations where the nanobubbles resided, when the sample was immersed in water (see also Fig. 4 in Appendix A for details).

The cross-sectional profiles for five different nanobubbles and their associated nanocraters (sorted by increasing nanobubble size) are shown in Figs. 2(d)–2(h). Interestingly, these profiles qualitatively ressemble the ones obtained on low-molecular-weight PS after embedding and subsequent removal of gold nanoparticles [12]. Moreover, it is clear that the lateral sizes of the nanocraters are approximately equal to the sizes of the nanobubbles—a commensurability valid for all samples in this study (see Fig. 5 in Appendix B). Nanobubbles with contact diameters $L \leqslant 50$ nm typically generate steeper nanocraters, and h_{dep} increases with L for those [Figs. 2(d)–2(f)]. When the contact diameter L is larger than 50 nm, the nanocraters are not as curved. Larger bubbles generate shallower craters with decreased h_{dep} and h_{rim} [Figs. 2(g) and 2(h)]. With further increased L, nanocraters with nearly flat bottoms are even created (see also Fig. 4 in Appendix A for details).

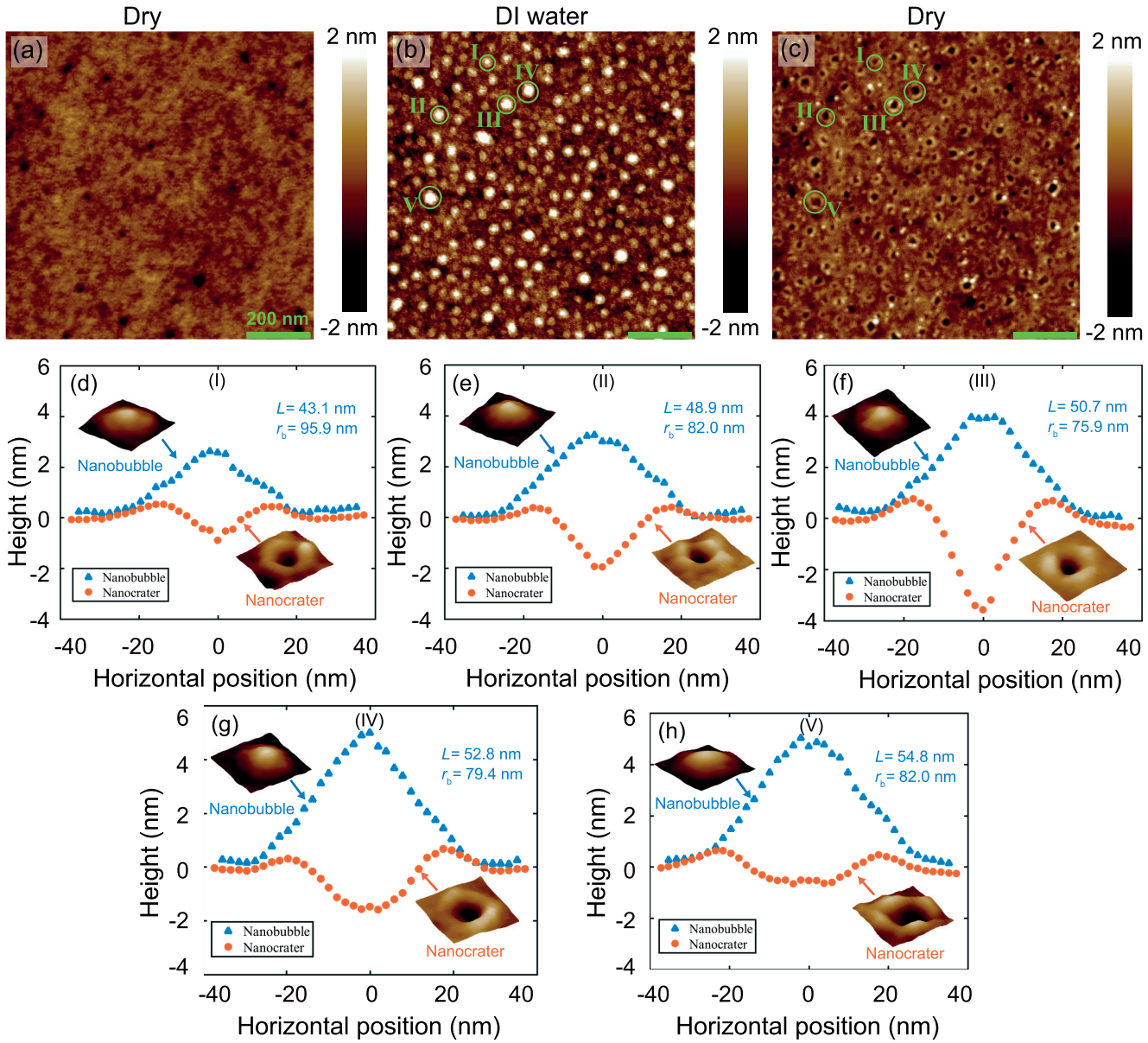

FIG. 2. Typical AFM images of an ultrathin glassy PS film with thickness $h_0 = 4.9 \pm 0.6$ nm in various situations: (a) before immersion in water; (b) after immersion in water, where nanobubbles (white) with an average contact diameter of 50 nm appear on top of it; (c) after immersion in water for $t_b \approx 240$ min, and subsequent removal of water followed by drying in air during $t - t_b \approx 250$ min. (d–h) Five cross-sectional profiles of nanobubble-nanocrater couples (sorted by increasing L values): $L = 43.1$ nm and $r_b = 95.9$ nm (d, couple I); $L = 48.9$ nm and $r_b = 82.0$ nm (e, couple II); $L = 50.7$ nm and $r_b = 75.9$ nm (f, couple III); $L = 52.8$ nm and $r_b = 79.4$ nm (g, couple IV); $L = 54.8$ nm and $r_b = 82.0$ nm) (h, couple V). The insets in each of those five panels are the 3D AFM images of the nanobubbles and the corresponding nanocraters.

To rationalize these observations, we invoke a theoretical model that combines two ingredients: (i) the existence of a liquidlike layer with viscosity η and thickness h_m of a few nanometers at the free surface (i.e., exposed to any fluid) of the glassy PS film [12,14]; and (ii) a lubrication flow in this liquidlike layer [15], driven by the pressure jump between p_b and p_{am} at the contact line where the three phases intersect, and opposed by the restoring capillary force due to the induced curvature at the PS-fluid interfaces. We note that the PS films employed in this work have thicknesses of a few nanometers only, which are: (i) comparable to the typical thickness of the liquidlike layer [7]; and (ii) much smaller than the radius of gyration of 350 kg/mol PS (tens of nanometers). Therefore, the PS chains are mostly located in the liquidlike layer, they are expected to exhibit a reduced entanglement density compared to the one in thicker films [40–43], and we expect no major anchoring effect [23]. Since the liquidlike layer thickness h_m is much smaller than the typical horizontal size L, the viscous flow in the layer can be described by lubrication theory [44], where the velocity is predominantly in the radial direction, the pressure is constant across the thickness of the liquidlike layer [45–47], and the viscous forces therein are

balanced by the tangential pressure gradient discussed above. As the stresses remain relatively low compared to usual yield stresses and piezoviscous thresholds for polymers glasses and melts, the viscosity η is assumed to be a constant.

In general, the stress and deformation fields associated to one bubble could be affected by the neighboring bubbles. In a recent study involving two microsized droplets on a polymer film [48] (see also Fig. 6 in Appendix C), it is indeed found that the effective interaction between the two microdroplets is strongly influenced by their distance d, contact diameter L, and the film thickness h_0. When $d > L/2$ or $d \gg h_0$, the two-body interaction mediated by the film vanishes. In the present work, the average value of d is around 50 nm, L is in between 20 nm and 45 nm, and h_0 is less than 8 nm. It is thus clear that d is much bigger than $L/2$ and h_0. Therefore, we neglect the influence of neighboring bubbles in the model.

We define $h(r,t)$ as the total thickness profile of the PS film (see Fig. 1), assumed to be axisymmetric given the symmetry of the nanobubble, where r is the horizontal radial spatial coordinate, and t is time. We further assume small slopes for the PS-fluid interfaces, as well as a no-slip boundary condition at the bottom of the mobile layer, located at $z = h(r,t) - h_m$, and a no-shear boundary condition at the PS-fluid interfaces, located at $z = h(r,t)$. All together, this leads to the axisymmetric version of the glassy thin-film equation [15], with a novel source term due to the presence of the nanobubble:

$$\frac{\partial h(r,t)}{\partial t} + \frac{h_m^3}{3\eta r}\frac{\partial}{\partial r}\left\{r\frac{\partial}{\partial r}\left[\frac{\gamma_i(r)}{r}\frac{\partial}{\partial r}\left(r\frac{\partial}{\partial r}h(r,t)\right) - p_i(r)\right]\right\} = 0, \tag{1}$$

where the surface energy $\gamma_i(r)$ indicates γ_{SL} (PS-water) for $r \geqslant L/2$ and $t < t_b$, as well as γ_{SV} for either $t > t_b$, or $t < t_b$ and $r < L/2$; while the external pressure $p_i(r)$ indicates p_b for $r \leqslant L/2$ and $t < t_b$, as well as p_{am} for either $t > t_b$, or $t < t_b$ and $r > L/2$. Due to the constant liquidlike layer thickness h_m, the equation is linear, and formally resembles the capillary-driven thin-film equation for bulk flow under perturbative profile variations [46,49]. Just before the formation of the nanobubble (assumed to be instantaneous), the PS film has a uniform thickness $h(r, t = 0) = h_0$, which we use as an initial condition.

We now nondimensionalize Eq. (1) by rescaling the variables through $h = H\,h_0$, $r = R\,L/2$, $t = T\,3\eta L^4/(16\gamma_{SV}h_m^3)$, and $t_b = T_b\,3\eta L^4/(16\gamma_{SV}h_m^3)$, which leads to the dimensionless form of Eq. (1):

$$\frac{\partial H(R,T)}{\partial T} + \frac{1}{R}\frac{\partial}{\partial R}\left\{R\frac{\partial}{\partial R}\left[\frac{1-\alpha(T)\Theta(R-1)}{R}\frac{\partial}{\partial R}\left(R\frac{\partial}{\partial R}H(R,T)\right) - \beta(T)\Theta(1-R)\right]\right\} = 0, \tag{2}$$

where Θ is the Heaviside function, $\alpha(T) = (\gamma_{SV} - \gamma_{SL})\Theta(T_b - T)/\gamma_{SV}$ and $\beta(T) = L^2\gamma_{LV}\Theta(T_b - T)/(2h_0 r_b \gamma_{SV})$. We solve Eq. (2) numerically from the initial condition $H(R, T = 0) = 1$, by using a finite-element method where the equation is divided into two coupled second-order partial differential equations involving two fields [50]: the height $H(R,T)$ and the total pressure $P(R,T) = \frac{\alpha(T)\Theta(R-1)-1}{R}\frac{\partial}{\partial R}[R\frac{\partial}{\partial R}H(R,T)] + \beta(T)\Theta(1-R)$. The fields are discretized with linear elements, and the coupled equations are solved with a Newton solver from the FEniCS library [51]. The numerical routine is performed with a constant time step $\Delta T = 5 \times 10^{-4}$ and a uniform spatial discretization step $\Delta R = 5 \times 10^{-4}$. Finally, as spatial boundary conditions at $R = 0$, we set the first-order derivatives of the two fields to be zero due to symmetry. Besides, we choose the size of the numerical domain such that no dynamics occurs at the large-R boundary, and we thus impose the first-order derivatives to be equal to zero too at this boundary.

Figure 3(a) shows an example of a numerical solution of Eq. (2). It includes two subsequent steps. The first one (corresponding to the dimensionless T from 0 to 0.04) is the nanocrater growth process with a nanobubble on top of the nanocrater. During the process, both the dimensionless depth h_{dep}/h_0 of the nanocrater and the dimensionless height h_{rim}/h_0 of the rim increase monotonically with dimensionless time. The second step (corresponding to the dimensionless T from 0.04 to 0.128) is the partial recovery of the nanocrater after the nanobubble is removed. The depth and height decrease monotonically with time. As the fluid in the liquidlike layer gets displaced, we also observe a continuous lateral shift in the dimensionless horizontal position of the rim.

In Figs. 3(b)–3(f), we fit the numerical solutions to the experimental profiles, for five nanocraters created by the five selected nanobubbles [shown in Figs. 2(d)–2(h)] of increasing contact diameters L from b to f. To do so, we first put back dimensions in the numerical solutions, by using the experimental parameters: $t - t_b = 250$ min, $\gamma_{SV} = 40.7$ mN/m, $\gamma_{LV} = 72.8$ mN/m, and $h_0 = 4.9 \pm 0.6$ nm, as well as the values of t_b, L and r_b for each nanobubble. As we determine the geometric parameters from a single snapshot of the nanobubble profile, which is not perfectly symmetric, there is some uncertainty in the obtained values. To account for this uncertainty, we multiply L and r_b by a dimensionless free parameter ρ. For all experiments in this study, the value of the latter is found to be in the 0.3–0.5 range, which is reasonably close to 1 and thus acceptable. We observe that the numerical solutions show a good agreement with experimental cross-sectional profiles for all five exemplary nanocraters. The depth h_{dep} of the nanocraters first increases and then decreases with increasing L. Interestingly, we find that it is actually r_b that determines h_{dep}. With increasing L, r_b first decreases from 95.9 nm (bubble I) to 75.9 nm (bubble III). Then it increases from 75.9 nm (bubble III) to 82.0 nm (bubble V). The smaller r_b leads to the larger deformation in the PS film, i.e., the larger magnitudes of the rim height h_{rim} and crater depth h_{dep}. This is expected due to the Laplace pressure of the nanobubbles, that scales as $\sim 1/r_b$, and that drives the deformation of the PS layer.

From the fitting procedure detailed above, we extract a single relevant free parameter: the surface mobility $h_m^3/(3\eta) =$

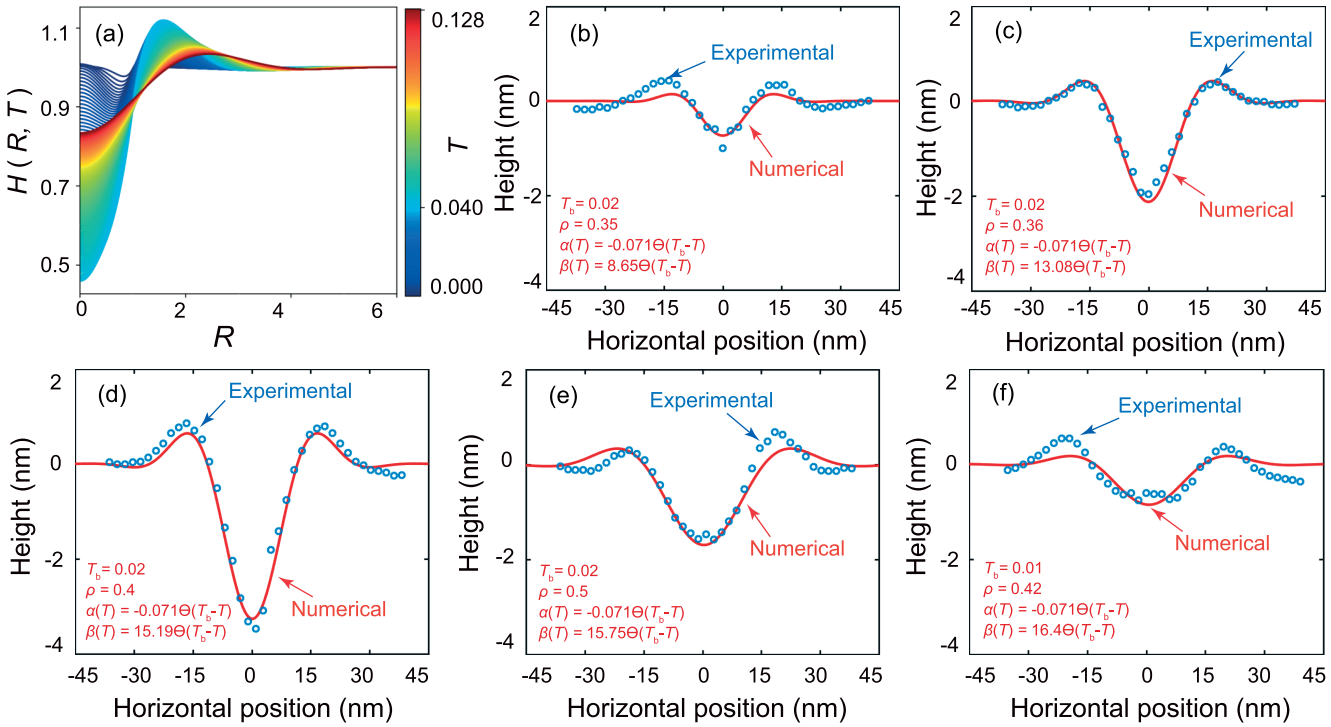

FIG. 3. Deformation of the PS film: (a) Numerical solution of Eq. (2) over a time interval $T \in [0, 0.128]$, for $T_b = 0.01$, $\alpha(T) = -0.071\,\Theta(T_b - T)$, and $\beta(T) = 5\,\Theta(T_b - T)$. (b–f) Cross-sectional AFM profiles (blue circular markers) in air for the five selected nanocraters in Figs. 2(d)–2(h), and corresponding best fit (red solid curves) to the numerical solution with $T_b = 0.02$, $\rho = 0.35$, $\alpha(T) = -0.071\,\Theta(T_b - T)$, and $\beta(T) = 8.65\,\Theta(T_b - T)$ (b); $T_b = 0.02$, $\rho = 0.36$, $\alpha(T) = -0.071\,\Theta(T_b - T)$, and $\beta(T) = 13.08\,\Theta(T_b - T)$ (c); $T_b = 0.02$, $\rho = 0.4$, $\alpha(T) = -0.071\,\Theta(T_b - T)$, and $\beta(T) = 15.19\,\Theta(T_b - T)$ (d); $T_b = 0.02$, $\rho = 0.5$, $\alpha(T) = -0.071\,\Theta(T_b - T)$, and $\beta(T) = 15.75\,\Theta(T_b - T)$ (e); $T_b = 0.01$, $\rho = 0.42$, $\alpha(T) = -0.071\,\Theta(T_b - T)$, and $\beta(T) = 16.4\,\Theta(T_b - T)$ (f). Note that the horizontal and vertical origins are arbitrarily shifted.

$2.31^{+1.73}_{-1.92} \times 10^{-10}$ nm^3/(Pa.s) of 350 kg/mol PS at room temperature. Regardless of the total PS film thickness, and the nanobubble geometry, the different experiments self-consistently exhibit the same value of surface mobility. Previously, the surface mobility of glassy PS was investigated around T_g for a range of molecular weights [14,15,52]. Interestingly, the extrapolation to room temperature of the Arrhenius-like trends in these works would lead to a surface mobility over one order of magnitude lower than the one reported here. This brings two possible nonexclusive scenarios: (i) a saturation of the surface mobility at low temperature; (ii) a reduction of the entanglement density, and thus viscosity, in strong confinement. Indeed, while it is known that in the near-T_g region the surface mobility exhibits an Arrhenius-like dependence in the temperature, which is characteristic of a liquidlike behavior [15,52], the mobility saturates at lower temperatures [12]. Regarding the entanglement density, it is found that polymer molecules at interfaces are less entangled than their bulk counterparts [41–43]. The entanglement density collapses rapidly when the film thickness becomes lower than the end-to-end distance of the polymer chains [40,53]. This further implies a reduction in viscosity [54–56]. For these reasons, since the PS films used here are colder and thinner than that in studies from the literature, one could expect a much higher mobility compared to Arrhenius-like extrapolations of the literature results.

Finally, we stress that the PS deformation profiles are transient, and that they in fact will continue to evolve with increasing time [see Fig. 3(a)], although very slowly. Moreover, a careful mathematical analysis of Eq. (1) reveals the absence of any relevant stationary state, which implies a dramatic consequence: due to the existence of a liquidlike surface layer, and provided the films are thin enough (i.e., h_0 close to h_m) to avoid anchoring effects at large molecular weights [23], the presence of surface nanobubbles should eventually lead to the dewetting of any ultrathin glassy PS film [57,58]. The critical time for dewetting is solely controlled by the parameters θ, γ_{SV}, γ_{LV}, h_0, and L (or r_b, due to volume conservation) above, as well as the surface mobility $h_m^3/(3\eta)$.

IV. CONCLUSION

As a conclusion, we have shown that immersing ultrathin glassy polystyrene films in water, in ambient conditions, leads to the spontaneous nucleation of air nanobubbles, which then generate nanocraters into the free surface of the PS films. The mechanism of such a dynamical deformation process is found by combining experimental atomic-force microscopy with a mathematical model based on lubrication theory applied to the liquidlike layer present at the free surface of a glassy film. The liquidlike layer is driven to flow by the pressure jump at the contact line where the three phases intersect, between the

nanobubble's inner Laplace pressure and the outer ambient pressure, and opposed by the capillary force due to the induced curvature at the PS-fluid interfaces. Since the Laplace pressure scales as the inverse of the bubble's radius of curvature, the size of the nanocraters can be finely controlled. From the excellent agreement between the experimental profiles and the numerical solutions of the modified glassy thin-film equation, we extract the surface mobility of the glassy films. Comparison of the surface mobility with extrapolated results from the literature points towards the possible saturation of surface mobility at low temperature, and/or the reduction of polymeric entanglement density (and thus viscosity) in confinement. All together, our work provides a novel, precise, and simple measurement of the surface nanorheology of glasses. Furthermore, our results highlight the influence of surface nanobubbles on the stability of immersed ultrathin glassy polymer films: the nanobubbles can drive the film towards dewetting, which would have important consequences for nanoimprint lithography [59] and nanomechanical data storage [60], to name a few.

ACKNOWLEDGMENTS

The authors thank James Forrest, Robert Style, Detlef Lohse, and Jacco Snoeijer for interesting discussions. Y.W. and S.R. appreciate financial support from the National Natural Science Foundation of China (Grants No. 51775028 and No. 52075029) and the Beijing Natural Science Foundation (Grant No. 3182022). A.C. is grateful for the financial support from the Norwegian Research Council, Projects No. 263056 and No. 301138.

APPENDIX A: NANOBUBBLE-NANOCRATER CORRELATION

Figure 4(a) shows AFM image of nanobubbles on the surface of an ultrathin PS glassy film in DI water. After water was removed, the AFM image of the exact same scanning area is shown in Fig. 4(d). From the figure, one can see that the sample surface is covered with nanocraters. To demonstrate that those nanocraters were indeed produced at the exact same locations as the nanobubbles, the AFM images of nanobubbles and nanocraters were segmented, as shown in Figs. 4(b) and 4(e), respectively. The obtained binary images of nanobubbles and nanocraters are shown in Figs. 4(c) and 4(f). The overlapped image [Fig. 4(g)] from the two binary images indicates that the nanocraters were generated at the exact same locations as the nanobubbles.

APPENDIX B: NANOCRATER FORMATION ON SAMPLES WITH DIFFERENT THICKNESSES

Three PS films of different thicknesses were used. Figures 5(a), 5(d) and 5(g) are AFM images in air of the three PS films with thicknesses of 2.8 ± 0.6 nm, 4.9 ± 0.6 nm, and 7.1 ± 0.8 nm, respectively. After immersion in DI water, the obtained AFM images are shown in Figs. 5(b), 5(e) and 5(h). One can see that nanobubbles with different sizes were produced on the surface of the PS samples. After DI water was removed [Figs. 5(c), 5(f) and 5(i)], nanocraters were observed on the surface of the PS samples. The sizes of the nanocraters are highly correlated with those of the nanobubbles. Larger nanobubbles lead to nanocraters with larger lateral widths.

For the sample with a thickness of 2.8 nm, one could observe pre-existed holes. However, we believe that these holes

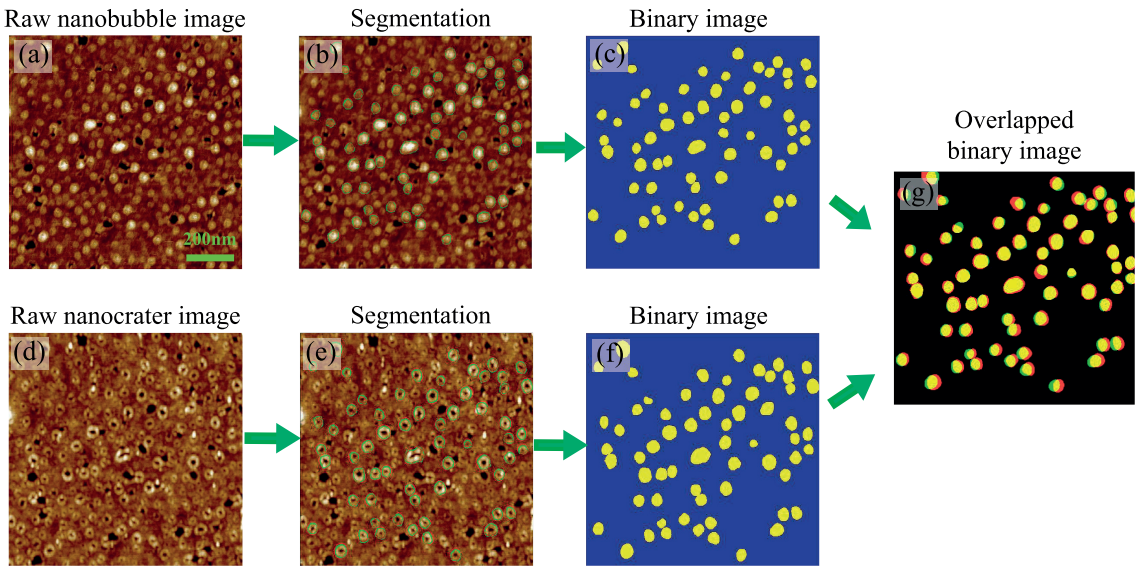

FIG. 4. (a) Raw AFM image of nanobubbles at the surface of an ultrathin glassy PS film in deionized (DI) water. (b) Segmentation of the nanobubble image. The green contours are extracted nanobubble boundaries. (c) The resulting binary image. The yellow masks are extracted nanobubble areas. (d) Raw AFM image of nanocraters at the exact same scanning area as in panel (a). (e) Segmented nanocrater image. (f) Resulting binary image of the segmented nanocrater image. The yellow masks are extracted nanocrater areas. (g) Superposition of the two binary images.

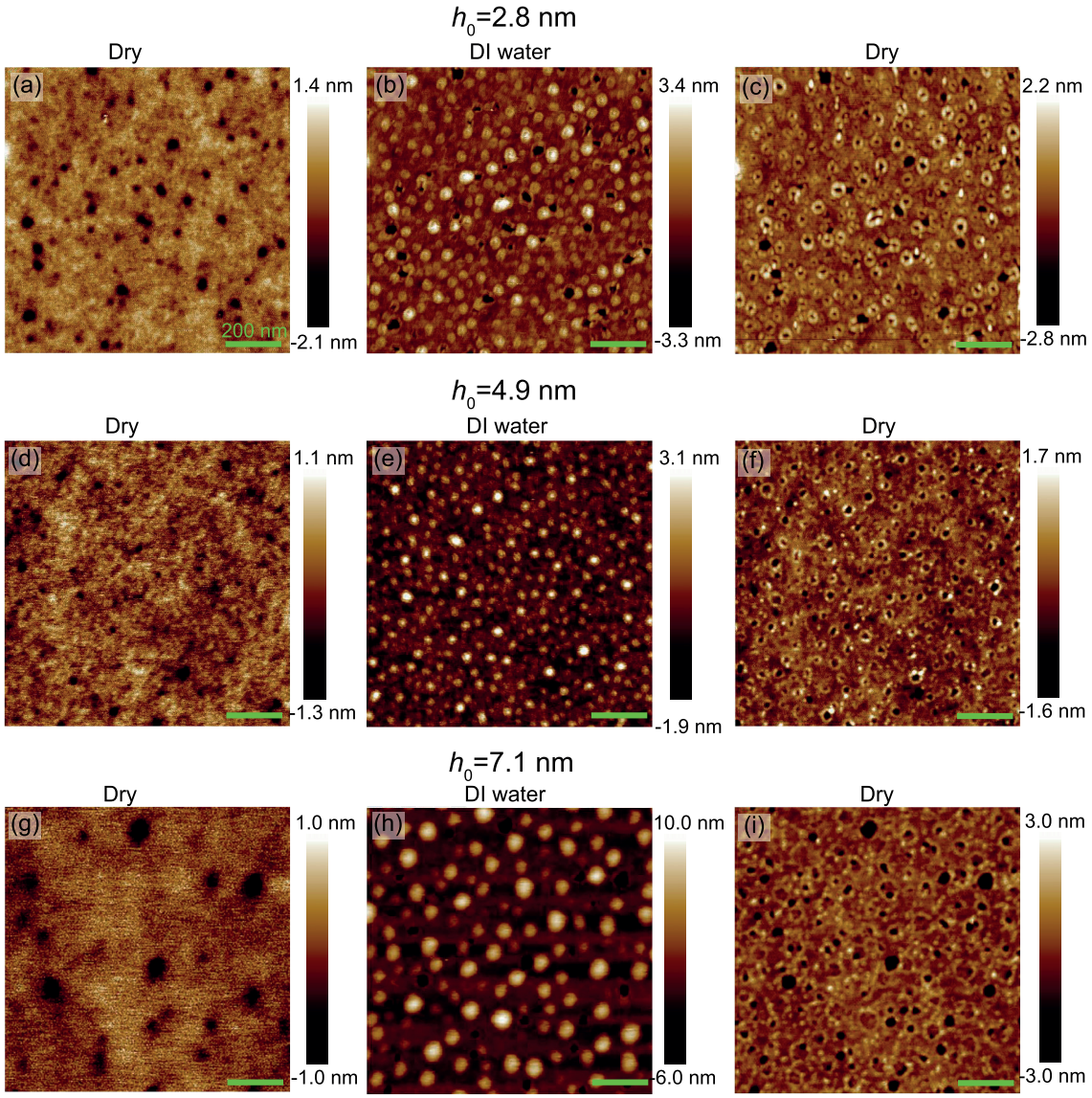

FIG. 5. (a) AFM image of the PS film with a thickness of 2.8 nm, obtained in air. (b) AFM image of the nanobubbles nucleated in the same scanning area as in panel (a), after immersion in DI water. (c) AFM image of the nanobubble-induced nanocraters, after DI water was removed. (d) AFM image of the PS film with a thickness of 4.9 nm, obtained in air. (e) AFM image of the nanobubbles nucleated in the same scanning area as in (d), after immersion in DI water. (f) AFM image of the nanobubble-induced nanocraters, after DI water was removed. (g) AFM image of the PS film with a thickness of 7.1 nm, obtained in air. (h) AFM image of the nanobubbles nucleated in the same scanning area as in panel (g), after immersion in DI water. (i) AFM image of the nanobubble-induced nanocraters, after DI water was removed.

are not due to the dewetting of the sample at room temperature (which would then impact the nanocrater dynamics), based on the following fact. If the film was close to dewetting, one would expect more holes to appear and grow with time. Figure 5 clearly shows that the number, locations, as well as sizes of the pre-existed holes do not change before and after water immersion. This clearly indicates that the surface of the solid-liquid interface is stable during the experiment, besides the nanocrater dynamics at stake. It is highly possible that the pre-existed holes were generated during the sample-preparation process, through the thermal-annealing step in particular.

APPENDIX C: INFLUENCE OF NEIGHBORING NANOBUBBLES

For a given nanocrater, it is *a priori* possible that the stress and deformation fields are influenced by neighboring nanobubbles. The influence from neighboring nanobubbles depends on the following geometrical parameters: the distance d between the bubbles, the contact radius $R_c = L/2$, and the substrate's thickness h_0. When $d \gg R_c$ or $d \gg h_0$, we expect the effects from neighboring bubbles to vanish, which was verified in microdroplet experiments [48] (see also Fig. 6). According to the latter, when d/R_c becomes comparable to

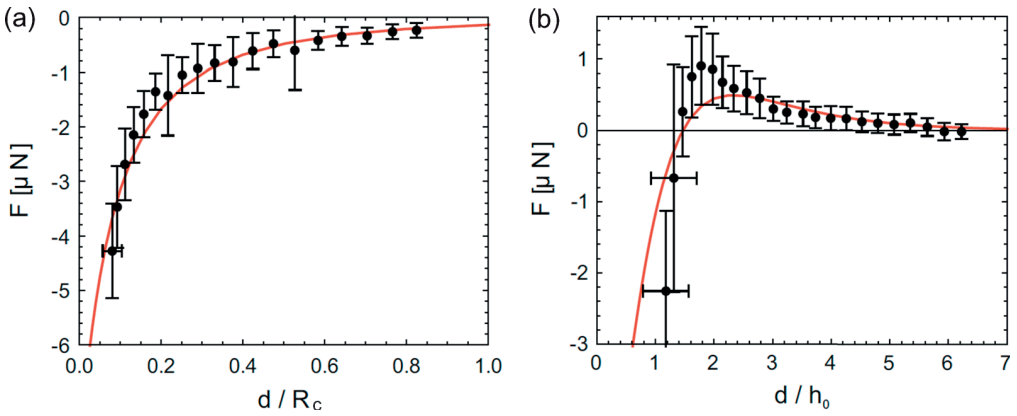

FIG. 6. Reproduction of Fig. 2 from Ref. [48]. (a) Interaction force (dots: measurements; line: model) F between two neighboring droplets as a function of the ratio between their separation distance d and the contact radius R_c. (b) Interaction force (dots: measurements; line: model) F between two neighboring droplets as a function of the ratio between their separation distance d and the substrate's thickness h_0.

or less than 1, and for large enough h_0, there is an attractive force F between the two droplets [see Fig. 6(a)]. Besides, when d/h_0 gets sufficiently larger than 1, the force becomes repulsive [see Fig. 6(b)].

In the present work, the distance d between two neighboring nanobubbles is around 50 nm. The contact radii of the nanobubbles are in between 20 nm and 45 nm. The initial thicknesses of the three different ultrathin PS films are $h_0 = 2.8 \pm 0.6$, 4.9 ± 0.6, and 7.1 ± 0.8 nm. Therefore, $d/R_c > 1$ and $d/h_0 \gg 1$, such that the influence of neighboring nanobubbles can be safely neglected in our study (see Fig. 6).

[1] P. W. Anderson, Science **267**, 1615 (1995).
[2] L. Berthier and G. Biroli, Rev. Mod. Phys. **83**, 587 (2011).
[3] G. Adam and J. H. Gibbs, J. Chem. Phys. **43**, 139 (1965).
[4] E. Donth, J. Polym. Sci., Part B: Polym. Phys. **34**, 2881 (1996).
[5] C. L. Jackson and G. B. McKenna, J. Chem. Phys. **93**, 9002 (1990).
[6] J. A. Forrest and K. Dalnoki-Veress, Adv. Colloid Interface Sci. **94**, 167 (2001).
[7] M. D. Ediger and J. A. Forrest, Macromolecules **47**, 471 (2014).
[8] J. L. Keddie, R. A. L. Jones, and R. A. Cory, Europhys. Lett. **27**, 59 (1994).
[9] J. A. Forrest, K. Dalnoki-Veress, J. R. Stevens, and J. R. Dutcher, Phys. Rev. Lett. **77**, 2002 (1996).
[10] O. Bäumchen, J. D. McGraw, J. A. Forrest, and K. Dalnoki-Veress, Phys. Rev. Lett. **109**, 055701 (2012).
[11] C. J. Ellison and J. M. Torkelson, Nat. Mater. **2**, 695 (2003).
[12] Z. Fakhraai and J. A. Forrest, Science **319**, 600 (2008).
[13] M. Ilton, D. Qi, and J. A. Forrest, Macromolecules **42**, 6851 (2009).
[14] Z. Yang, Y. Fujii, F. K. Lee, C.-H. Lam, and O. K. C. Tsui, Science **328**, 1676 (2010).
[15] Y. Chai, T. Salez, J. D. McGraw, M. Benzaquen, K. Dalnoki-Veress, E. Raphael, and J. A. Forrest, Science **343**, 994 (2014).
[16] H. Kim, Y. Cang, E. Kang, B. Graczykowski, M. Secchi, M. Montagna, R. D. Priestley, E. M. Furst, and G. Fytas, Nat. Commun. **9**, 2918 (2018).
[17] W. Ogieglo, K. Tempelman, S. Napolitano, and N. E. Benes, J. Phys. Chem. Lett. **9**, 1195 (2018).
[18] L. Zhu, C. W. Brian, S. F. Swallen, P. T. Straus, M. D. Ediger, and L. Yu, Phys. Rev. Lett. **106**, 256103 (2011).
[19] W. Zhang and L. Yu, Macromolecules **49**, 731 (2016).
[20] I. Tanis, K. Karatasos, and T. Salez, J. Phys. Chem. B **123**, 8543 (2019).
[21] W. W. Mullins, J. Appl. Phys. **28**, 333 (1957).
[22] H. Le-The, C. Tregouet, M. Kappl, M. Müller, K. Kirchhoff, D. Lohse, A. van den Berg, M. Odijk, and J. C. T. Eijkel, Nanotechnology **30**, 065301 (2009).
[23] Y. Chai, T. Salez, and J. A. Forrest, Macromolecules **53**, 1084 (2020).
[24] P. De Gennes, Eur. Phys. J. E **2**, 201 (2000).
[25] S. T. Milner and J. E. Lipson, Macromolecules **43**, 9865 (2010).
[26] I. Siretanu, H. Saadaoui, J.-P. Chapel, and C. Drummond, Macromolecules **48**, 2787 (2015).
[27] F. Varnik, J. Baschnagel, and K. Binder, Phys. Rev. E **65**, 021507 (2002).
[28] J. Baschnagel and F. Varnik, J. Phys.: Condens. Matter **17**, R851 (2005).
[29] K. Ngai, A. Rizos, and D. Plazek, J. Non-Cryst. Solids **235**, 435 (1998).
[30] D. Long and F. Lequeux, Eur. Phys. J. E **4**, 371 (2001).
[31] J. E. G. Lipson and S. T. Milner, Eur. Phys. J. B **72**, 133 (2009).
[32] S. Mirigian and K. S. Schweizer, J. Chem. Phys. **141**, 161103 (2014).
[33] T. Salez, J. Salez, K. Dalnoki-Veress, E. Raphael, and J. A. Forrest, Proc. Natl. Acad. Sci. USA **112**, 8227 (2015).
[34] M. Arutkin, E. Raphaël, J. A. Forrest, and T. Salez, Soft Matter **13**, 141 (2016).
[35] Y. Wang and B. Bhushan, Soft Matter **6**, 29 (2010).
[36] D. Lohse and X. Zhang, Rev. Mod. Phys. **87**, 981 (2015).
[37] P. O'Connell and G. McKenna, Science **307**, 1760 (2005).

[38] Y. Wang, B. Zeng, X. Li, and X. Zhang, Adv. Mater. Interfaces **6**, 1900002 (2019).
[39] Y. Wang, X. Li, S. Ren, H. T. Alem, L. Yang, and D. Lohse, Soft Matter **13**, 5381 (2017).
[40] A. Silberberg, J. Colloid Int. Sci. **90**, 86 (1982).
[41] R. L. Jones, S. K. Kumar, D. L. Ho, R. M. Briber, and T. P. Russell, Nature **400**, 146 (1999).
[42] L. Si, M. V. Massa, K. Dalnoki-Veress, H. R. Brown, and R. A. L. Jones, Phys. Rev. Lett. **94**, 127801 (2005).
[43] O. Bäumchen, R. Fetzer, and K. Jacobs, Phys. Rev. Lett. **103**, 247801 (2009).
[44] C. K. Batchelor and G. Batchelor, *An Introduction to Fluid Dynamics* (Cambridge University Press, Cambridge, UK, 1967).
[45] R. Blossey, *Thin Liquid Films: Dewetting and Polymer Flow* (Springer Science & Business Media, Berlin, 2012).
[46] T. Salez, J. D. McGraw, O. Bäumchen, K. Dalnoki-Veress, and E. Raphaël, Phys. Fluids **24**, 102111 (2012).
[47] T. Salez, J. D. McGraw, S. L. Cormier, O. Bäumchen, K. Dalnoki-Veress, and E. Raphaël, Eur. Phys. J. E **35**, 114 (2012).
[48] S. Karpitschka, A. Pandey, L. A. Lubbers, J. H. Weijs, L. Botto, S. Das, B. Andreotti, and J. H. Snoeijer, Proc. Natl. Acad. Sci. USA **113**, 7403 (2016).
[49] M. Backholm, M. Benzaquen, T. Salez, E. Raphael, and K. Dalnoki-Veress, Soft Matter **10**, 2550 (2014).
[50] C. Pedersen, J. F. Niven, T. Salez, K. Dalnoki-Veress, and A. Carlson, Phys. Rev. Fluids **4**, 124003 (2019).
[51] A. Logg, K.-A. Mardal, and G. Wells, *Automated Solution of Differential Equations by the Finite Element Method: The FEniCS Book*, Vol. 84 (Springer Science & Business Media, Berlin, 2012).
[52] F. Chen, D. Peng, C.-H. Lam, and O. K. C. Tsui, Macromolecules **48**, 5034 (2015).
[53] H. Hasegawa, T. Ohta, K. Ito, and H. Yokoyama, Polymer **123**, 179 (2017).
[54] F. Brochard Wyart and P.-G. de Gennes, Eur. Phys. J. E **1**, 93 (2000).
[55] H. Bodiguel and C. Fretigny, Phys. Rev. Lett. **97**, 266105 (2006).
[56] K. Shin, S. Obukhov, J.-T. Chen, J. Huh, Y. Hwang, S. Mok, P. Dobriyal, P. Thiyagarajan, and T. Russell, Nat. Mater. **6**, 961 (2007).
[57] G. Reiter, Phys. Rev. Lett. **87**, 186101 (2001).
[58] P. Damman, N. Baudelet, and G. Reiter, Phys. Rev. Lett. **91**, 216101 (2003).
[59] J. Teisseire, A. Revaux, M. Foresti, and E. Barthel, Appl. Phys. Lett. **98**, 013106 (2011).
[60] P. Vettiger, G. Cross, M. Despont, U. Drechsler, U. Durig, B. Gotsmann, W. Haberle, M. A. Lantz, H. E. Rothuizen, R. Stutz, and G. K. Binnig, IEEE Trans. Nanotechnol. **1**, 39 (2002).

Paper V

Film deposition and dynamics of a self-propelled wetting droplet on a conical fibre

Tak Shing Chan, Christian Pedersen, Joel Koplik, Andreas Carlson

Published in Journal of Fluid Mechanics, 907, (2021). DOI: https://doi.org/10.1017/jfm.2020.834

V

J. Fluid Mech. (2021), *vol*. 907, A29. © The Author(s), 2020. **907** A29-1
Published by Cambridge University Press

doi:10.1017/jfm.2020.834

Film deposition and dynamics of a self-propelled wetting droplet on a conical fibre

Tak Shing Chan[1],†, **Christian Pedersen**[1], **Joel Koplik**[2] **and Andreas Carlson**[1],†

[1]Mechanics Division, Department of Mathematics, University of Oslo, Oslo 0316, Norway

[2]Benjamin Levich Institute and Department of Physics, City College of the City University of New York, New York, NY 10031, USA

(Received 14 March 2020; revised 11 August 2020; accepted 16 September 2020)

We study the dynamic wetting of a self-propelled viscous droplet using the time-dependent lubrication equation on a conical-shaped substrate for different cone radii, cone angles and slip lengths. The droplet velocity is found to increase with the cone angle and the slip length, but decrease with the cone radius. We show that a film is formed at the receding part of the droplet, much like the classical Landau–Levich–Derjaguin film. The film thickness h_f is found to decrease with the slip length λ. By using the approach of matching asymptotic profiles in the film region and the quasi-static droplet, we obtain the same film thickness as the results from the lubrication approach for all slip lengths. We identify two scaling laws for the asymptotic regimes: $h_f h_o'' \sim Ca^{2/3}$ for $\lambda \ll h_f$ and $h_f h_o''^3 \sim (Ca/\lambda)^2$ for $\lambda \gg h_f$; here, $1/h_o''$ is a characteristic length at the receding contact line and Ca is the capillary number. We compare the position and the shape of the droplet predicted from our continuum theory with molecular dynamics simulations, which are in close agreement. Our results show that manipulating the droplet size, the cone angle and the slip length provides different schemes for guiding droplet motion and coating the substrate with a film.

Key words: drops, thin films, lubrication theory

1. Introduction

Coating a film onto a substrate as a liquid is forced to move along it is a technique used in painting and industrial applications such as lithography, which has been studied since the early twentieth century (Quéré 1999). Dip coating is one way to coat a plate as it is withdrawn from a liquid reservoir above a critical plate velocity (Snoeijer *et al.* 2006; Maleki *et al.* 2011; Gao *et al.* 2016). A mathematical model describing this film coating was developed in the seminal works by Landau & Levich (1942) and Derjaguin (1943). These theoretical works sparked a great interest in film coating, later adopted for a range of solid geometries, e.g. cylindrical fibres (White & Tallmadge 1966; Wilson 1988; De Ryck & Quéré 1996), coating by rollers (Taylor 1963; Wilson 1982) and coating the inner surface of a channel/tube (Bretherton 1961; Tabeling & Libchaber 1986).

† Email addresses for correspondence: taksc@math.uio.no, acarlson@math.uio.no

Some studies have focused on how other physical effects influence the film deposition such as gravity (Derjaguin 1943; Snoeijer *et al.* 2008), inertia (De Ryck & Quéré 1996; Orsini & Tricoli 2017), surfactants (Carroll & Lucassen 1973), particles on the interface (Colosqui, Morris & Stone 2013; Dixit & Homsy 2013*a*,*b*), van der Waals forces for deposited films of nanometric scales (Quéré, di Meglio & Brochard-Wyart 1989) as well as effects of substrate roughness (Krechetnikov & Homsy 2005) and confinement due to the reservoir (Kim & Nam 2017). Much of the extensive literature on the film deposition dynamics has been summarized in several review articles (Ruschak 1985; Quéré 1999; Weinstein & Ruschak 2004; Rio & Boulogne 2017).

The classical theory by Landau & Levich (1942) and Derjaguin (1943) gives a fundamental description of thin film coating, where the deposited film thickness is so thin that gravity can be neglected. The flow inside the film region is maintained by the balance of capillarity, characterized by the liquid/air surface tension coefficient γ, and the viscous forces, characterized by the liquid viscosity η. The film region is connected to a quasi-static liquid reservoir of a length scale that is much larger than the thickness of the deposited film. When a plate is withdrawn from a reservoir, this length is set by the capillary length $\ell_c \equiv (\gamma/\rho g)^{1/2}$, with ρ the liquid density and g the gravitational acceleration. By using the method of asymptotic matching, the thickness of the film h_f, denoted as the Landau–Levich–Derjaguin (LLD) film, is shown to have a universal scaling with respect to the plate velocity U as $h_f/\ell_c \sim Ca^{2/3}$, where the capillary number $Ca \equiv \eta U/\gamma$ is the ratio between the viscous and the surface tension forces. Remarkably, this $Ca^{2/3}$ power law has been demonstrated to be a robust relation in many different systems when a fluid film is deposited. The only required change in the scaling relation is to replace the capillary length by the corresponding characteristic length of the system. For example, the film thickness is rescaled by the fibre radius for the case when a cylindrical fibre is withdrawn from a bath (White & Tallmadge 1966; James 1973; Wilson 1988); while in the case of a long bubble moving in a tube, also known as Bretherton's problem, the corresponding length is the tube radius (Bretherton 1961).

Common to fluid coating processes is that they often require an external driving force to displace the fluid. However, when a droplet with a size smaller than the capillary length comes in contact with a conical fibre, it moves spontaneously from the tip to the base of the cone due to capillarity (Lorenceau & Quéré 2004; Li & Thoroddsen 2013). In nature, this self-propelled mechanism has been exploited by plants (Liu *et al.* 2015) and animals (Zheng *et al.* 2010; Wang *et al.* 2015) to facilitate water transport at small scales. When a droplet is translating above a critical velocity, a layer of liquid film is expected to be deposited on the conical surface at the receding part of the droplet. It has been discovered recently on the trichome of the *Sarrancenia* that the deposited film provides a wetted surface, enabling later water droplets to be transported at a velocity several orders of magnitude larger than found in other plants (Chen *et al.* 2018). Despite the importance of understanding the film deposition and potential implications for biological evolution in plants and giving a path to very fast droplet transport, the film deposition has not been studied before on conical geometries. Previous fluid coating studies have assumed a no-slip condition at the fluid–solid boundary, i.e. no relative motion between the fluid and the solid boundary. Interestingly, slip lengths have been reported to be as large as a few micrometres for fluids such as polymer melts (Bäumchen, Fetzer & Jacobs 2009) and for superhydrophobic surfaces (Rothstein 2010). When the droplet size is decreased to a few micrometres or below, effects due to the fluid slip on solid surface may become significant, as demonstrated in dynamical fluidic systems (Lauga, Brenner & Stone 2007; Bocquet & Charlaix 2009) such as the dewetting of microdroplets (McGraw *et al.* 2016; Chan *et al.* 2017) and of liquid films (Fetzer *et al.* 2005). However, the influence of slip on

the droplet dynamics and film deposition is not known for the directional droplet motion on a cone.

Although conical solid structures are common in nature and appear as a component in industrial processes, modelling of the droplet fluid flow on such geometries is lacking. In our recent article (Chan, Yang & Carlson 2020), we provide a physical picture of the spontaneous motion of the droplet based on the mismatch between the equilibrium contact angle and the apparent contact angles. This generates flow in the contact line regions and maintains the droplet motion. In this study, we implement the time-dependent lubrication equation developed in Chan *et al.* (2020) to investigate the evolution of the liquid–air interface of the capillary driven droplet motion on a smooth conical fibre. The properties of a deposited film generated by a self-propelled droplet are studied for small cone angles and for a wide range of slip lengths. Apart from the continuum approach, the simple geometry of a conical shape allows us to study fluid flow using molecular dynamics (MD) simulations. Results from the MD simulations will be used as a verification for the droplet shape predicted by the lubrication model. In fact, the approach of MD simulations has previously been implemented to study the wetting dynamics at the nanoscale (Nakamura *et al.* 2013), the slip condition at a contact line region (Qian, Wang & Sheng 2003), the frictional force on a sliding droplet (Koplik 2019) and the influence of physico-chemistry of the water/substrate interface on the droplet dynamics (Johansson, Carlson & Hess 2015).

2. Mathematical formulation

An axisymmetric viscous droplet with a volume V is placed in contact with a wetted surface of a conical fibre with a cone angle $\alpha \ll 1$, see figure 1(a). We consider a fibre surface prewetted with a thin layer of the same fluid of thickness ϵ. The prewetted layer can be deposited or interpreted as a microscopic precursor film for a perfectly wetting droplet, i.e. equilibrium contact angle $\theta_e = 0^\circ$. The profile of the liquid–air interface is described by $h(r, t)$, the distance between the interface and the substrate, as a function of the distance from the vertex of the cone along its surface r and time t. For droplets with a Bond number $Bo \equiv \rho g V^{2/3}/\gamma \ll 1$, gravitational effects can be ignored. We consider the Reynolds number $Re \equiv \rho U V^{1/3}/\eta \ll 1$ and the flow inside the droplet is described by the Stokes equations and the continuity equation.

2.1. *Lubrication approximation on a cone (LAC)*

Consider the flow in the droplet as $\boldsymbol{u}(r, \theta)$, here θ is the polar angle measured from the axis of rotation. Supposing the polar angle of the free surface of the droplet is very small, the flow is primarily in the radial direction. By using these approximations, the Stokes equations reduce to the lubrication equations here given in spherical coordinates (Chan *et al.* 2020),

$$\frac{\partial p}{\partial r} = \frac{\eta}{r^2\theta}\frac{\partial}{\partial \theta}\left(\theta \frac{\partial u}{\partial \theta}\right), \tag{2.1}$$

$$\frac{\partial p}{\partial \theta} = 0, \tag{2.2}$$

where p is the pressure and u is the radial velocity inside the droplet/film.

To describe the fluid flow (2.1) and (2.2) need to be accompanied by several boundary conditions. At the liquid–air surface, the tangential stress is zero as we neglect viscous

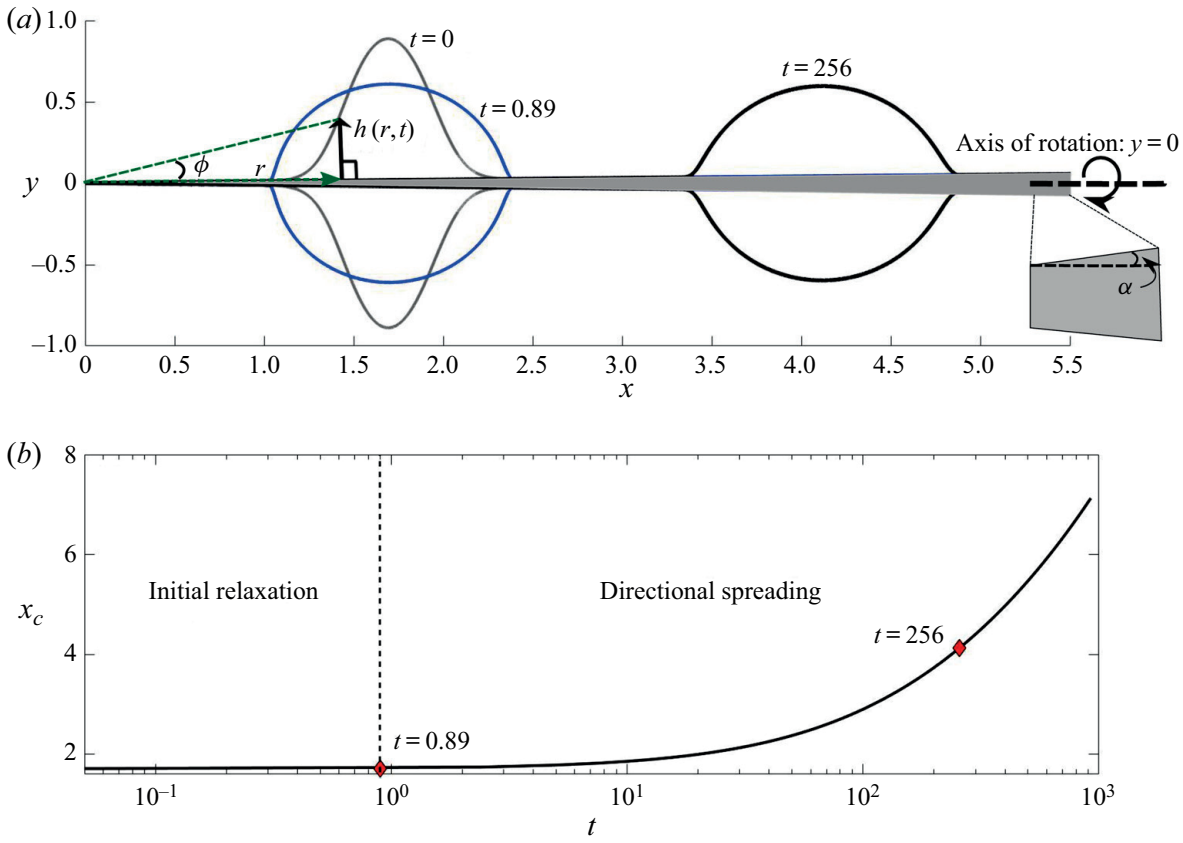

FIGURE 1. (*a*) A description of the system at study, where a droplet is moving across (from left to right) a conically shaped fibre (grey shaded region). Droplet profiles $h(r, t)$ are shown at three different times on the fibre with a cone angle α. From $t = 0$ to $t = 0.89$, there is a fast relaxation of the droplet before it slowly spreads across the fibre. (*b*) The centre of mass of the droplet x_c plotted as a function of time. The diamond markers correspond to the two profiles shown in (*a*), with a cone angle $\alpha = 0.01$ rad, a prewetted film thickness $\epsilon = 10^{-3}$ and a slip length $\lambda = 0$.

effects in the air

$$\frac{\partial u}{\partial \theta} = 0 \quad \text{at } \theta = \alpha + \phi. \tag{2.3}$$

At the wetted substrate, the normal velocity is zero and we assume a radial velocity described by the Navier-slip condition (Lauga, Brenner & Stone 2008)

$$\frac{u}{\lambda} = \frac{1}{r}\frac{\partial u}{\partial \theta} \quad \text{at } \theta = \alpha, \tag{2.4}$$

where λ is the slip length.

Solving (2.1) and (2.2) with the boundary conditions (2.3) and (2.4) gives the velocity, and by imposing mass conservation of the liquid we get

$$\frac{\partial h}{\partial t} + \frac{1}{r\alpha + h}\frac{\partial}{\partial r}\left[\frac{r^4\alpha^4}{2\eta}\frac{\partial p}{\partial r}\left\{\frac{1}{8}\left[3\left(1+\frac{h}{r\alpha}\right)^4 - 4\left(1+\frac{h}{r\alpha}\right)^2 + 1\right]\right.\right.$$
$$\left.\left. - \frac{1}{2}\left(1+\frac{h}{r\alpha}\right)^4 \ln\left(1+\frac{h}{r\alpha}\right) - \frac{\lambda h^2}{2r^3\alpha^3}\left(2+\frac{h}{r\alpha}\right)^2\right\}\right] = 0. \tag{2.5}$$

The pressure gradient inside the liquid is generated by the Laplace pressure $p = -\gamma\kappa$ where κ is the curvature of the liquid–air interface, which for $\alpha \ll 1$ simplifies as

$$\kappa = \frac{h''}{\left(1 + h'^2\right)^{3/2}} - \frac{1 - \alpha h'}{(r\alpha + h)\left(1 + h'^2\right)^{1/2}}, \tag{2.6}$$

with $()' \equiv \partial()/\partial r$. The second term of the curvature is derived by using a rotation matrix with the cone angle $\alpha \ll 1$. We keep the h' terms as the interface slope is not always small at the droplet scale. We will see in § 3.1 that the viscous effect is weak in the droplet and it quickly adopts a quasi-static shape at the leading order, which is determined by the uniform pressure condition i.e. $\kappa =$ constant. Although the flow field computed from the lubrication equation is inaccurate at the droplet scale, the correct quasi-static shape determines the flows in the contact line regions where lubrication approximation does work. Hence, (2.5) is still valid for computing the evolution of the interface.

2.2. *Finite element method*

We solve a coupled system of equations consisting of (2.5) and the Laplace pressure equation $p = -\gamma\kappa$ numerically by using the finite element method. For the pressure equation, we split it into the two following equations:

$$p = -\gamma\left[\frac{q'}{\left(1 + h'^2\right)^{3/2}} - \frac{1 - \alpha h'}{(r\alpha + h)\left(1 + h'^2\right)^{1/2}}\right] \tag{2.7}$$

and

$$q = h'. \tag{2.8}$$

The variables we solve for are $h(r, t)$, $p(r, t)$ and $q(r, t)$. These fields are discretized with linear elements and solved as a coupled equation set by using Newton's method in the FEniCS library (Logg, Mardal & Wells 2012). We use both an adaptive time stepping routine and an adaptive spatial discretization to refine the spatial resolution around the receding tail and the advancing front of the droplet with a resolution of $\Delta r = 10^{-4}V^{1/3}$; here, Δr is the difference of r between two nodal points. The numerical simulations are initialized with the initial profile $h(r, t = 0) = \epsilon + A[1 - \tanh(r - r_i)^2]$ where A determines the volume of the droplet and r_i determines the initial position of the droplet's geometric centre. The simulations are insensitive to the initial droplet shape after a very short initial relaxation, see figure 1 and appendix B. Further, we impose the following boundary conditions at the boundary $\partial\Omega$ of the numerical domain: $p(r = \partial\Omega, t) = p(r = \partial\Omega, t = 0)$ and $\partial h(r = \partial\Omega, t)/\partial r = 0$.

2.3. *Molecular dynamics simulations*

We can test our hydrodynamic model by means of a 'numerical experiment' – a classical MD simulation of a liquid drop placed on a solid cone, based on standard methods (Frenkel & Smit 2002). We consider a generic viscous liquid consisting of spherically symmetric atoms with a Lennard–Jones (LJ) interaction, bound into linear tetramer molecules by a

Case	x_1	x_2	R_{out}	N
A	30	40	75	117 880
B	30	45	70	164 120
C	30	45	70	280 280

TABLE 1. Initial geometry of the drops.

FENE (finitely extensible nonlinear elastic) potential

$$V_{LJ}(\mathcal{X}) = 4E\left[\left(\frac{\mathcal{X}}{\sigma}\right)^{-12} - \left(\frac{\mathcal{X}}{\sigma}\right)^{-6}\right] \quad V_{FENE}(\mathcal{X}) = -\frac{1}{2}k_F\mathcal{X}_0^2 \ln\left(1 - \frac{\mathcal{X}^2}{\mathcal{X}_0^2}\right), \quad (2.9a,b)$$

where $\mathcal{X}$ is the separation between the centre of mass of two atoms. The LJ potential acts between all pairs of atoms within a cutoff distance 2.5σ, and is shifted by a linear term so that the force vanishes at the cutoff. The FENE interaction (with parameters $k_F = 30E/\sigma^2$ and $\mathcal{X}_0 = 1.5\sigma$), following Grest & Kremer (1986) acts between adjacent atoms on the chain. The advantage of a molecular rather than a monatomic liquid is that the vapour pressure is very low and the liquid/vapour interface is relatively sharp and easy to visualize. The solid is a conical section of a regular lattice whose atoms are mobile but bound to their lattice sites by linear springs with stiffness $100E/\sigma^2$. The simulations are conducted in a canonical/NVT ensemble, where the temperature is fixed at $0.8E/k_B$ using a Nosé–Hoover thermostat. This particular solid/liquid system has been used in a number of previous simulations (Busic, Koplik & Banavar 2003; Koplik *et al.* 2006; Koplik & Zhang 2013; Koplik & Maldarelli 2017), and its properties are well characterized. The liquid has bulk number density $0.857\sigma^{-3}$, viscosity $5.18m/(\sigma\tau)$ and liquid–vapour surface tension $0.668E/\sigma^2$, where m is the mass of the liquid atoms and $\tau = \sigma(m/E)^{1/2}$ is the natural time scale based on the LJ parameters. Furthermore, the liquid is completely wetting: a drop placed on flat solid surface with the same density and interactions spreads completely into a thin film.

The simulation begins with all atoms on face-centred cubic (fcc) lattice sites, within a rectangular box of length 256.5σ and sides 171σ, with repulsive confining walls in the long (x) direction and periodic boundary conditions on the sides. For the cone we select all atoms in an fcc lattice of number density $1.06\sigma^{-3}$ within a radius $R_{co}(x) = 3 + x\tan\alpha$ (in the unit of σ) of the central axis, which runs in the x-direction through the centre of the box, and where $\alpha = 0.1$ rad. The resulting solid has 74,362 atoms. The liquid initially occupies a disc-shaped region near the left edge, $x_1 < x < x_2$ and $R_{co}(x) < \mathcal{R} < R_{out}$ consisting of all atoms outside the cone but inside an outer radius R_{out}. We have studied two cases (A, B) where the remaining cone surface is initially dry and one case (C) where there is also a liquid (prewetting) film of thickness 4σ. The parameters for the various cases and the number of fluid atoms N is given in table 1. The simulation temperature starts at a low value in the solid phase and increases linearly to the final value, $0.2 \rightarrow 0.8E/k_B$ over 250τ, to prevent the liquid atoms from leaving the cone, and subsequently the drop is allowed to evolve freely at the final temperature.

3. Results and discussions

3.1. *Numerical solutions of the LAC*

We first present numerical simulation results for the typical evolution of the droplet profile obtained from the lubrication approximation on a cone. In the following, all lengths are rescaled by $V^{1/3}$ and time is rescaled by $V^{1/3}\eta/\gamma$. The dimensionless parameters are the cone angle α, the thickness of the prewetted layer ϵ and the slip length λ.

A typical dynamical process is shown in figure 1(*a*). First the droplet relaxes from an initial shape ($t = 0$) to a quasi-static shape ($t = 0.89$) in a short time. At $t = 0$, the initial shape gives a non-uniform curvature and hence a non-uniform pressure inside the whole droplet region. The pressure gradient generates flow inside the droplet. At $t = 0.89$, a nearly uniform pressure distribution is achieved in the bulk of the droplet, but a large pressure gradient is created at the two edges of the droplet, which are commonly referred to as the 'contact line regions', see figure 2(*b*) for the pressure distribution at $t = 256$. A concentration of stresses at the contact line would be expected (Huh & Scriven 1971). After the quick initial relaxation, the droplet starts to propagate toward the thicker part of the cone. The position of the droplet is described by the centre of mass of the droplet, for $\alpha \ll 1$, defined as

$$x_c = \pi \int_{r_r}^{r_a} h(h + 2\alpha r) r \, \mathrm{d}r, \tag{3.1}$$

which is plotted as a function of time in figure 1(*b*). Here r_r is the apparent receding and r_a is the apparent advancing contact line positions, which are defined in appendix A. The numerical simulations suggest that the droplet adopts a quasi-static shape during the directional spreading. For example, the profile for $t = 256$ is plotted as the black solid line in figure 2(*a*), and the pressure distribution is shown in figure 2(*b*). Given the uniform pressure/curvature condition, one can solve for a static droplet profile, see the details of the computation in § 3.5. The static profile obtained in this way is plotted as the red dashed curve in figure 2(*a*) for the same droplet position as obtained from the LAC at $t = 256$. The agreement between the two profiles again demonstrates that the droplet profile is quasi-static on the droplet scale. As the droplet shape appears more round than flat, it may affect the validity of the lubrication approximation in the contact line regions where the viscous effects are significant. We zoom into the advancing and receding contact line regions and compute the pressure gradient p' rescaled by its maximum magnitude and the interfacial slope h', which are shown in figures 2(*c*) and 2(*d*). We observe that when approaching the contact line regions, the pressure gradient p' increases from almost zero in the bulk of the droplet, and along with it the interface slope decreases. The maximum magnitude of the pressure gradient in both the receding and the advancing regions corresponds to an interfacial slope of magnitude < 0.1 rad (5.7°) which presumably fulfils the small slope assumption.

As shown in figures 2(*c*) and 2(*d*), the pressure gradients at the receding and the advancing contact line regions are large. By zooming into these regions of the droplet (see figure 3) at early times, we observe large interface curvatures, consistent with what one would expect from the results of a large pressure gradient. We want to highlight that as the droplet starts to move across the cone, a film is formed at the receding region. Since the later self-propelling state is independent of the initial conditions, the droplet properties such as the deposited film thickness and the droplet velocity are a function of the droplet position on the cone.

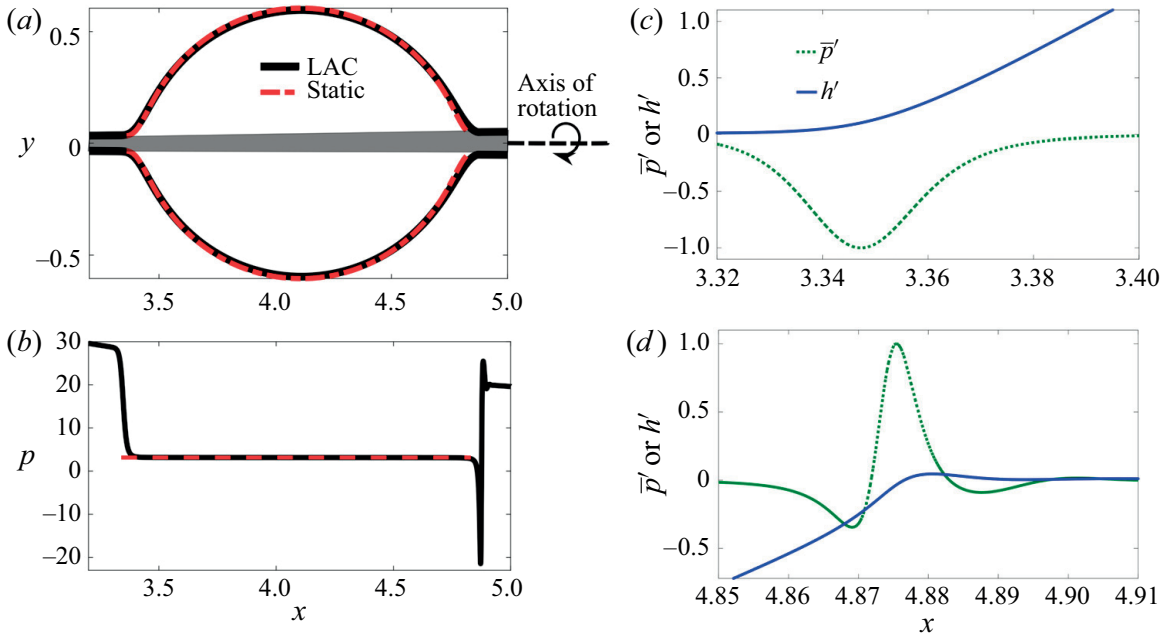

FIGURE 2. (*a*) Solid line: droplet shape on a conical fibre (grey shaded region) with a cone angle $\alpha = 0.01$ rad at $t = 256$ obtained from a numerical solution of the LAC with $\epsilon = 10^{-3}$ and $\lambda = 0$. Red dashed line: static droplet shape obtained from solving the uniform curvature condition $\kappa =$ constant. (*b*) Solid line: the Laplace pressure p as a function x obtained from LAC. Red dashed line: the Laplace pressure of a static droplet, where the domain of the static droplet is between $x = 3.36$ and $x = 4.83$. In (*c*,*d*) the pressure gradient is rescaled by its maximum value, denoted as $\bar{p}'$ and the interface slope h' in the receding region in (*c*) and the advancing region in (*d*).

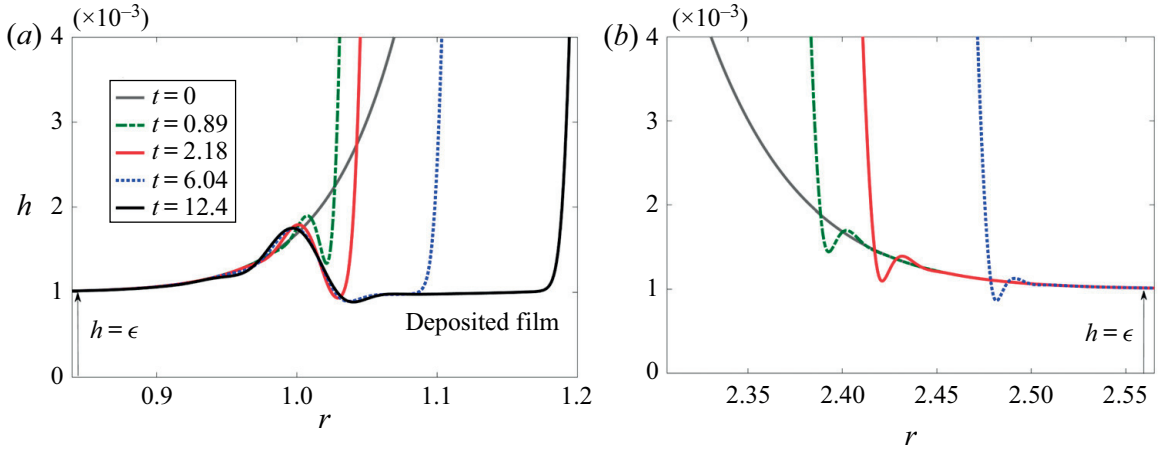

FIGURE 3. (*a*) Interface dynamics at the receding region of the droplet, showing the formation of a deposited film from $t > 2.18$. (*b*) The interface dynamics at the advancing region of the droplet. The far field conditions of the profiles at both ends match to a constant prewetted fluid layer of thickness $h = \epsilon = 10^{-3}$ and we have $\alpha = 0.01$ rad and $\lambda = 0$.

3.2. *Comparison of the numerical solutions of the LAC with molecular dynamics simulations*

We compare the results for the case of cone angle $\alpha = 0.1$ rad from the numerical solutions of the LAC and the MD simulations. The comparison serves also as a verification of our

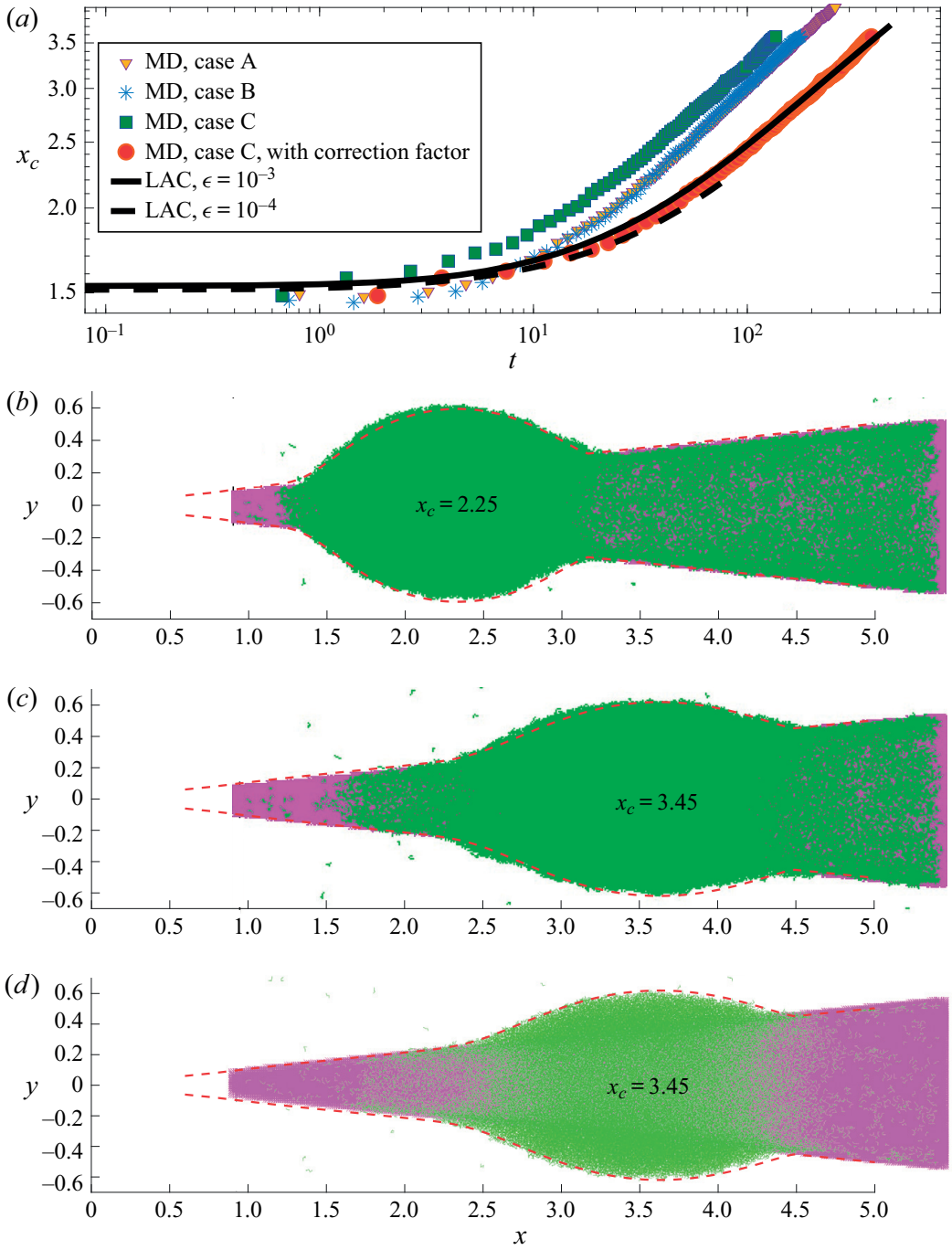

FIGURE 4. (*a*) The centre of mass of the droplet x_c as a function of time t obtained from the MD simulations (symbols) for three different cases and the numerical solutions of the LAC (lines) for $\lambda = 0$ and $\alpha = 0.1$ rad. The red circles are results obtained by multiplying the time in case C with a prefactor 2.8. (*b–d*) Comparison between droplet profiles obtained from the LAC and the MD simulations. For each comparison, the profiles are chosen such that x_c is the same. Both (*b*,*c*) are for the case C of the MD simulations (wetted substrate) but at two different droplet positions; (*d*) is for case A (dry substrate) of the MD simulations. Red dashed curves: profiles from LAC. Green dots: liquid molecules of the droplet. Pink colour: the cone substrate.

lubrication model and can help reveal nanoscopic physical effects. We first compare the centre of mass of the droplet x_c as a function of time in figure 4(*a*). For the LAC, we have used two different values of prewetted layer thickness, i.e. $\epsilon = 10^{-4}$ and 10^{-3}, to highlight their weak influence on the results. We have three cases for the MD simulations.

We see that droplets on the dry surface (case A and case B) move slower than the droplet on the wet surface (case C, with the rescaled thickness of the prewetted layer = 0.065). This is consistent with the expectation that the wetted layer reduces the frictional force between the droplet and the substrate. When comparing with the LAC results, we find that the results from the MD simulation (for both the dry surface and wet surface cases) have a larger non-dimensional velocity. When we multiply the time scale in MD by a prefactor of 2.8 for case C (with a wetted layer), we effectively shift the data from MD horizontally to the right and obtain the results represented by red circles, which makes the two models give the same results. The difference in time scale is equivalent to the difference in drop velocity, and this is related to the strength of the 'driving force'. In the MD calculation the liquid/solid interaction strength controls the speed of the drop (as well as the slip length), but this parameter does not appear directly in the continuum calculations. Indeed, in continuum calculations of wetting usually the contact angle (for partially wetting cases) and the van der Waals interaction (for the completely wetting case) controls the motion. Here, the prewetting film thickness and the assumption that it is asymptotically constant indirectly incorporate this information. There is no obvious way to match this aspect of the molecular and continuum calculations in advance and it is no surprise that they differ. Furthermore, the presence of slip in the simulations is rather unclear because the translation velocity of the drop is much smaller than the thermal velocity of the atoms, by a factor of 10^{-3} or less, and it is not possible to resolve the flow field inside the drop. However, simulations of the same liquid in shear flow along a planar solid of the same structure as the cone, under otherwise identical conditions, have a velocity field which extrapolates to zero roughly halfway between the innermost liquid and outermost solid atoms. If one (naturally) identifies the latter point as the liquid/solid boundary then the slip length is at most a small fraction of an atomic diameter, which is essentially zero. The shapes of the droplet are shown in figure 4(*b–d*), where the same droplet shapes are predicted by the LAC and the MD when comparing for the same centre of mass of the droplet. However, no deposited film is observed for all cases in the MD simulations.

The effects of the thin prewetted layer are illustrated when comparing a drop advancing on a cone at the same centre of mass position ($x_c = 3.45$) for the wetted case in figure 4(*c*) with the dry case in figure 4(*d*). The lighter colouring of the liquid region as compared to figure 4(*b*,*c*) reflects the fact that there are fewer liquid molecules present in the dry case. For the dry case, the advancing meniscus of the drop is irregular at molecular scales, corresponding to individual molecules hopping to attractive sites on the surface, which is also the case for wetting drops advancing on a dry flat surface (D'Ortona *et al.* 1996). The receding meniscus region is an uneven film as well, zero to two molecules in thickness, and this behaviour is also present in the prewetted case. The absence of a continuous trailing film for these drops is surprising because one would expect a completely wetting liquid to remain in contact with a solid unless removed by an external force, and the lubrication calculations in this paper incorporate this assumption. One possible explanation is the finite size of the simulated droplets, which may not have enough molecules to exhibit all features of continuum behaviour. A second, more specific explanation involves the curvature of the surface. Liquid adjacent to a flat surface tends to form pronounced layers and, at least for a crystalline solid, there is an ordered structure in each layer because the molecules favour positions in register with the lattice. High curvature disrupts the usual lattice structure and could thereby weaken the liquid-solid attraction. In this vein, it is known that solid curvature has a significant effect on slip lengths, which are controlled by the same interaction (Chen, Zhang & Koplik 2014; Guo, Chen & Robbins 2016).

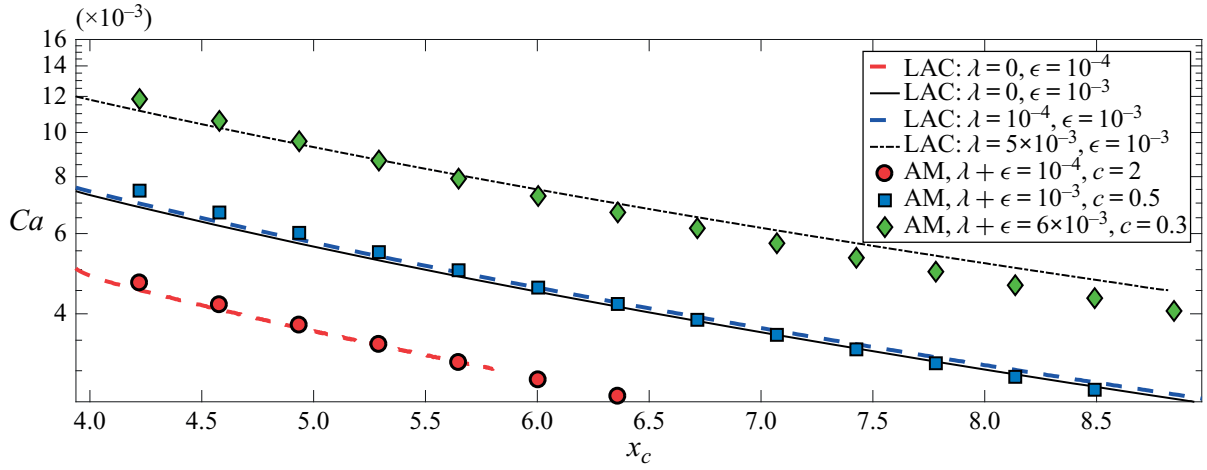

FIGURE 5. Lines: the capillary number Ca as a function of the centre of mass of the droplet x_c obtained from LAC. Symbols: the relation given by (3.3) with different values of c. The cone angle is $\alpha = 0.01$.

3.3. *Droplet velocity*

We consider here only cases in which the prewetted layer is much thinner than the droplet, i.e. $\epsilon \in [10^{-4}, 10^{-3}]$, but we vary the slip length across a wide range $\lambda \in [0, 20]$. When the prewetted layer is thick, e.g. $\epsilon > 10^{-2}$, it becomes unstable quickly due to Rayleigh–Plateau instability (Eggers & Villermaux 2008). To investigate the droplet dynamics, we define the capillary number as the dimensionless velocity of the droplet, namely

$$Ca \equiv \frac{\mathrm{d}x_c}{\mathrm{d}t}. \tag{3.2}$$

3.3.1. *Dependence of droplet velocity on the thickness of the prewetted layer and the slip length*

We start by looking at cases when both the prewetted layer and the slip length are small, i.e. $\epsilon \ll 1$ and $\lambda \ll 1$. In models of dynamical wetting (Bonn *et al.* 2009; Snoeijer & Andreotti 2013), these microscopic lengths act as a cutoff length scale for moving contact line singularity and the length scales appear in a logarithmic term of the viscous dissipation. In Chan *et al.* (2020), by using asymptotic matching, it is shown that the capillary number scales as $Ca = \theta_a^3/9\ln(c/\lambda)$, where θ_a is the advancing apparent contact angle of the corresponding static droplet and c is a fitting parameter. We here propose a similar relation but include the prewetted layer thickness ϵ as

$$Ca = \frac{\theta_a^3}{9\ln(c/[\lambda+\epsilon])}. \tag{3.3}$$

With an adjustment of the fitting parameter c, this relation describes well the results from the LAC as shown in figure 5, but gradually becomes invalid when λ is no longer small.

When exploring a wider range of slip length λ, one expects a change in the flow profile inside the droplet, from a Poiseuille flow for the case of no-slip to a plug flow as we approach free slip (Münch, Wagner & Witelski 2005). Figure 6(*a*) shows Ca as a function of x_c for different slip lengths, where droplets move faster for larger slip lengths as the viscous dissipation is decreased. At large slip lengths, it is expected that the term with the slip length in the governing equation (2.5) dominates over the other terms, thus λ can be

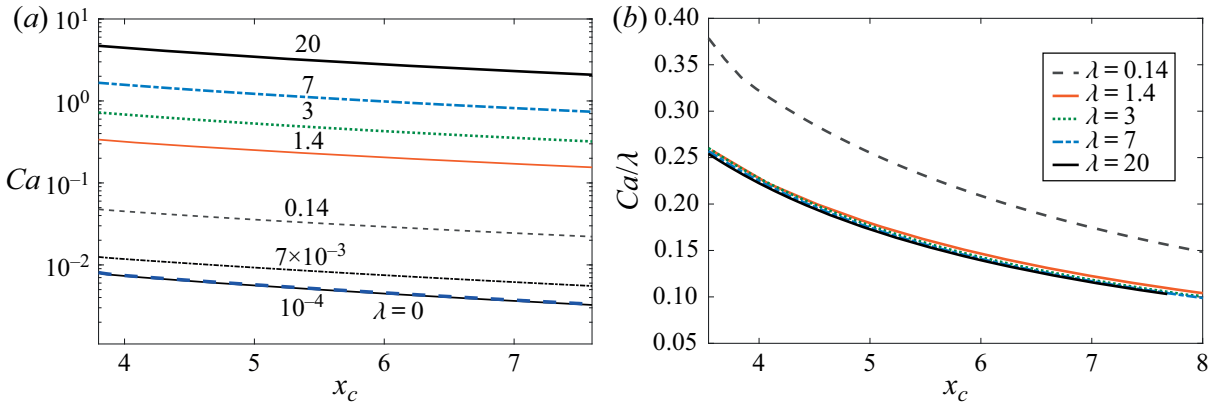

FIGURE 6. (*a*) The capillary number Ca plotted as a function of the centre of mass of the droplet x_c for different slip lengths. (*b*) The rescaled Ca by λ as a function of x_c. Parameters: $\epsilon = 10^{-3}$ and $\alpha = 0.01$ rad. We rescale the data in (*a*) as Ca/λ, which collapses the data onto a single curve for $\lambda > 1$.

scaled out from the equation by defining $\bar{t} \equiv \lambda t$. This implies Ca scales linearly with λ. We plot Ca rescaled by λ in figure 6(*b*), and find that Ca/λ collapse onto a single curve for $\lambda > 1$, consistent with our expectation. An alternative derivation can also be made based on a balance between the rate of change of capillary energy and the viscous dissipation. The viscous stress scales as $\sim \eta U/\lambda$, giving a bulk dissipation $\sim \eta V U^2/\lambda^2$, which is much smaller than the dissipation due to friction at the substrate $\sim \eta A_w U^2/\lambda$; here, A_w is the wetted area. By balancing the dominant viscous dissipation with the rate of change of the surface energy $\partial(\gamma A_w)/\partial t \sim \gamma x_c \alpha U$ gives $U \sim \lambda$.

3.3.2. *Dependence of droplet velocity on the cone angle and the droplet position*

As there is no directional spreading when $\alpha = 0$, it is natural to expect that a droplet moves faster at larger cone angles. This is true when comparing Ca at the same cone radius, as shown in figure 7(*a*) in which Ca is plotted as a function of $R_c \equiv x_c \tan\alpha$. The results from the LAC agree nicely with the matching results of (3.3) for the three different values of α using the same value of $c = 2$. Remarkably, the agreement is good even when the apparent contact angle is as large as $\theta_a \approx 1$ rad, for example when $R_c \approx 0.06$ and $\alpha = 0.03$ rad. Another feature we observe is that Ca decreases when the droplet is at a position of larger cone radius for a fixed cone angle, namely the droplet slows down when moving to the thicker part of the cone. When plotting Ca rescaled by α in figure 7(*b*), the results for the three different cone angles nearly collapse onto a single curve.

We have shown that the cone angle and the cone radius give opposite effects to the droplet velocity. It might be interesting to see how the droplet velocity depends on the distance from the tip of the cone, particularly the length of a fibre can be a more important parameter for certain functionality. In figure 7(*c*), we show Ca as a function of the droplet's centre of mass x_c. Remarkably, a non-monotonic behaviour is observed. In the limit of large distances from the tip, droplets on cones with smaller cone angles move faster when comparing at the same x_c. When decreasing x_c, there are changes of relative strength of Ca. For example, at $x_c = 2.3$, Ca for $\alpha = 0.03$ rad is even higher than that for $\alpha = 0.01$ rad. The reason for the non-monotonic behaviour is that two factors are playing roles when comparing at the same x_c, namely α and R_c. The influence of the cone radius R_c is dominant over the cone angle effect when x_c is large, thus droplets move faster at smaller α.

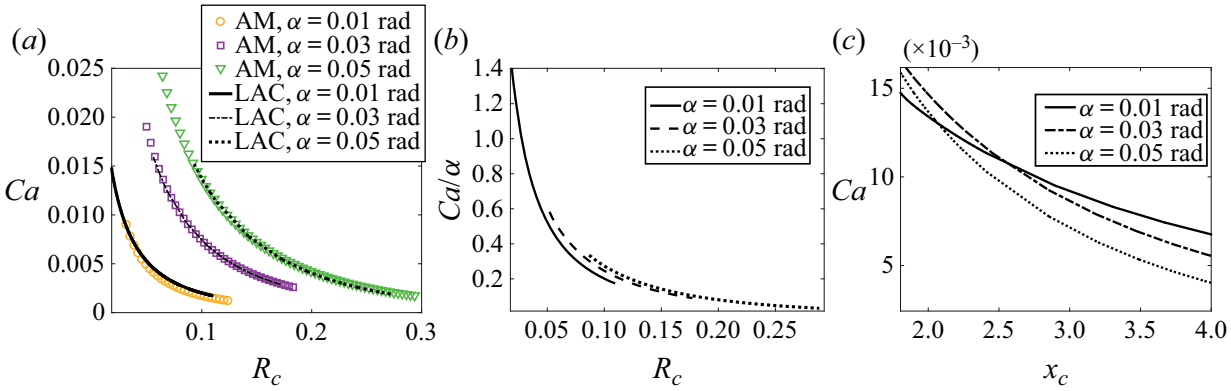

FIGURE 7. Lines: results from LAC. Symbols: the relation given by (3.3) with $c = 2$. The droplet capillary number Ca plotted as a function of $R_c \equiv x_c \tan\alpha$ in (a), and as a function of the centre of mass of the droplet x_c in (c), whereas in (b) Ca is rescaled by α plotted as a function of R_c. Parameters: $\epsilon = 10^{-3}$ and $\lambda = 0$.

The cone angle effect becomes more important when x_c is small. Our results demonstrate that a sensitive control of the geometrical factors such as α and R_c is necessary for optimal droplet transport on these structures.

3.4. *Film deposition*

A film is formed at the receding region of the droplet when the droplet moves to the thicker part of the cone, as already shown in figure 3(a). We refer to the region that connects the prewetted layer and the deposited film as the film edge region. One can observe from figure 3(a) that the film edge region (around $r = 1$) propagates much slower than the motion of the droplet. Hence a long deposited film is generated and the film profile is found to remain steady within the simulated time. However, the film would eventually become unstable due to the Rayleigh–Plateau instability, but the time scale for the growth of the disturbance is here greater than the time for the droplet to spread across the cone. For films of nanometric thickness, they can be stabilized by intermolecular forces (Quéré, di Meglio & Brochard-Wyart 1990).

3.4.1. *Dependence of the deposited film on the cone angle*

We first consider cases of no slip ($\lambda = 0$). The profiles of the deposited films are shown in figure 8(a) for $\alpha = [0.01, 0.03, 0.05]$ rad. It is found that the film thickness increases with both α and r. It is also important to understand the influence of the cone angle on the film thickness when comparing at the same cone radius. We hence plot in figure 8(b) the profiles of the films as a function of $R \equiv r \sin\alpha$. The film is thicker for larger cone angles. As will be explained in § 3.5, this is mainly due to the larger capillary number for larger cone angles.

3.4.2. *Dependence of the deposited film on the slip length*

As droplets move faster at larger slip lengths, one may expect that a thicker film is deposited according to the LLD model. However, our analysis shows the opposite results (figure 9) with $\alpha = 0.01$ rad and $\epsilon = 10^{-3}$. The film thickness decreases with the slip length. We find two asymptotic film profiles. One is for the limit of small slip length ($\lambda < 10^{-4}$). Another one is for the limit of large slip length ($\lambda > 1$), which can be understood by

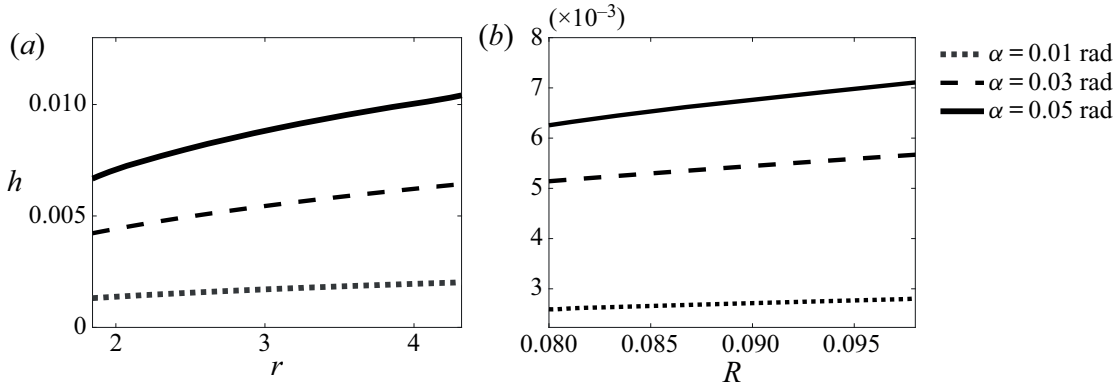

FIGURE 8. (*a*) The profiles of the deposited film h plotted as a function of the distance from the tip of the cone r for $\alpha = [0.01, 0.03, 0.05]$ rad. (*b*) The profiles of the deposited film h plotted as a function of the cone radius R. Parameters: $\epsilon = 10^{-3}$ and $\lambda = 0$.

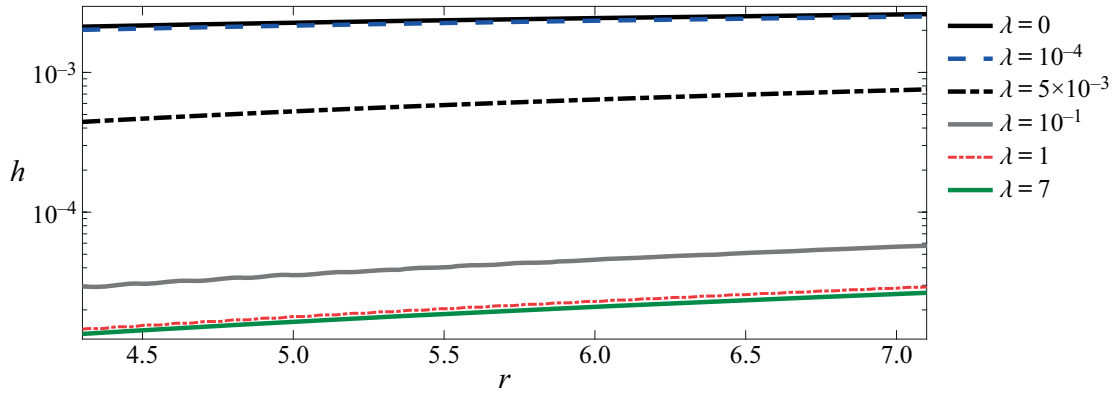

FIGURE 9. The profiles of the deposited film h plotted as a function of the distance from the tip of the cone r for different slip lengths. Parameters: $\epsilon = 10^{-3}$ and $\alpha = 0.01$ rad.

the argument that the slip length is absorbed into the time variable $\bar{t}$ as explained in § 3.3. Hence, the droplet profile and the deposited film thickness become independent of the slip length. A dramatic change of film thickness appears for slip length in between 10^{-4} and 1. The difference of film thickness between these two limits is of two orders of magnitude. Our results show that when the droplet size is too small, film deposition is not possible as the film thickness computed from our model can be of sub-molecular size. This is particularly relevant for large slip lengths, for which the deposited film is much thinner and the large slip regime can be realized usually for droplet size of micrometres or below.

3.5. *Asymptotic matching*

Although we have shown the interface profiles $h(r)$ of the deposited films (figures 8 and 9), it is not clear yet how a particular film thickness is related to the capillary number. For droplets spreading on a cone, the motion of the droplet is self-propelled, and the capillary number is a function of the droplet position x_c (or time t). Nevertheless, at each moment in time, the droplet deposits a portion of film with a particular thickness $h_f = h_f(x_c)$. Hence, we can link a particular film thickness to the corresponding Ca at each droplet position on the cone. The procedure of determining h_f is given in appendix A. A natural way to rescale the film thickness h_f is by using the corresponding cone radius $R_f \equiv r_f \sin\alpha$ where the film is deposited. The rescaled h_f/R_f is plotted as a function of Ca

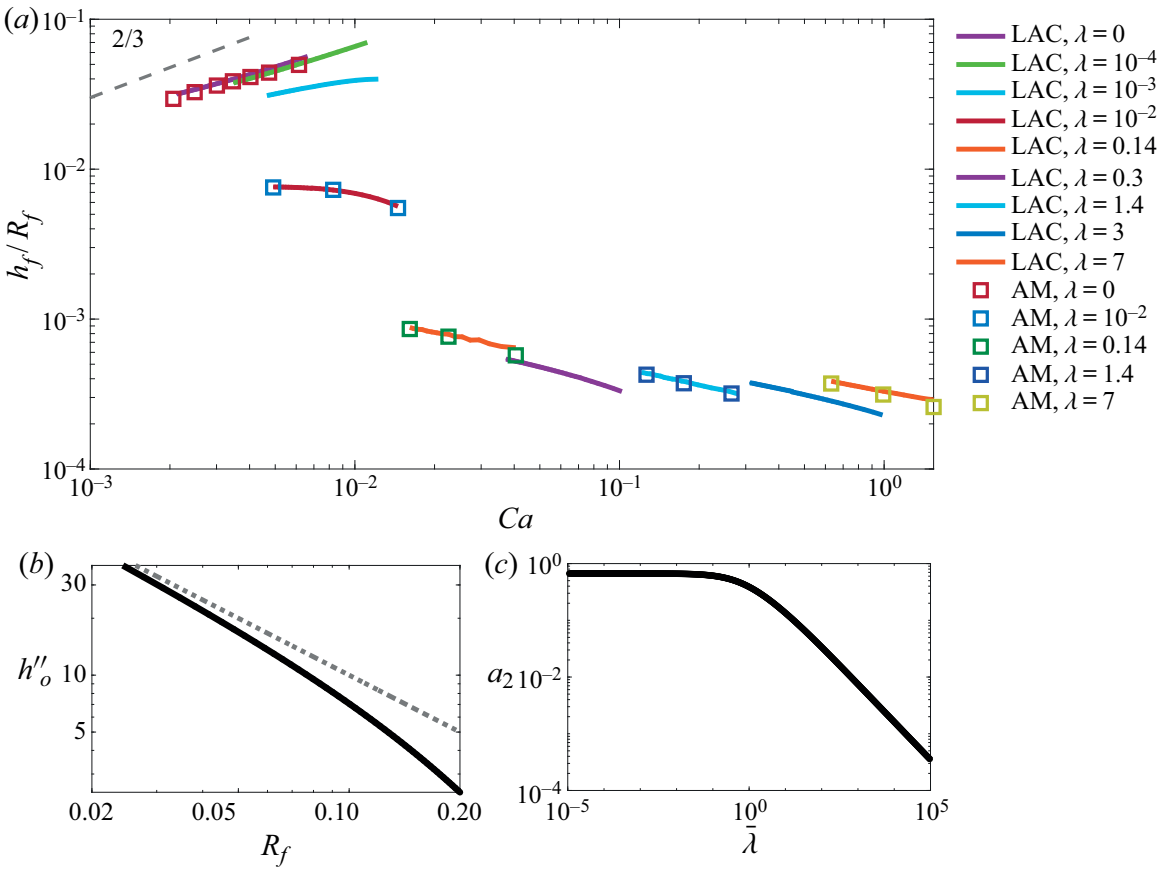

FIGURE 10. (*a*) The rescaled film thickness h_f/R_f as a function of the capillary number Ca for different slip lengths. Lines: results from the lubrication approach (LAC). Parameters: $\epsilon = 10^{-3}$ and $\alpha = 0.01$ rad. Squares: results from the asymptotic matching (AM). The grey dashed line indicates a scaling $Ca^{2/3}$. (*b*) Solid line: the second derivative at the apparent receding contact line of a static droplet $h''_o \equiv h''_s(r = r_r)$ as a function of the cone radius of a deposited film R_f. The dashed line represents the asymptotic relation $h''_o = 1/R_f$ when $R_f \ll 1$. (*c*) The value of a_2 obtained from the two-dimensional lubrication equation for the film region as a function of the rescaled slip length $\bar{\lambda} \equiv \lambda/h_f$.

for a wide range of slip length λ in figure 10(*a*) with log–log axes. First, the 2/3 scaling is not observed for any cases, even for the no-slip case which we would expect from the LLD model. Second, the local slope (in log scales) decreases with the slip length, and becomes negative when the slip length $> 10^{-2}$.

To understand better the numerical solutions of the LAC, we revisit the approach of asymptotic matching. We consider two regions of the liquid–air interface profile: the film region and the static droplet region, which are described by two different force balance equations. We then match the asymptotic profiles of these two regions to determine the deposited film thickness.

As the film thickness is much smaller than the cone radius, we propose that the profile in the film region locally is described by a steady solution $h = h_{2d}(x)$ of the two-dimensional lubrication equation. In the droplet frame, translating with a non-dimensional velocity Ca, the rescaled liquid–air interfacial profile $H(\xi) = h_{2d}/h_f$, here $\xi = xCa^{1/3}/h_f$, follows (Snoeijer *et al.* 2008)

$$\frac{\partial^3 H}{\partial \xi^3} = \frac{3}{H\left(H + 3\bar{\lambda}\right)}\left(1 - \frac{1}{H}\right), \tag{3.4}$$

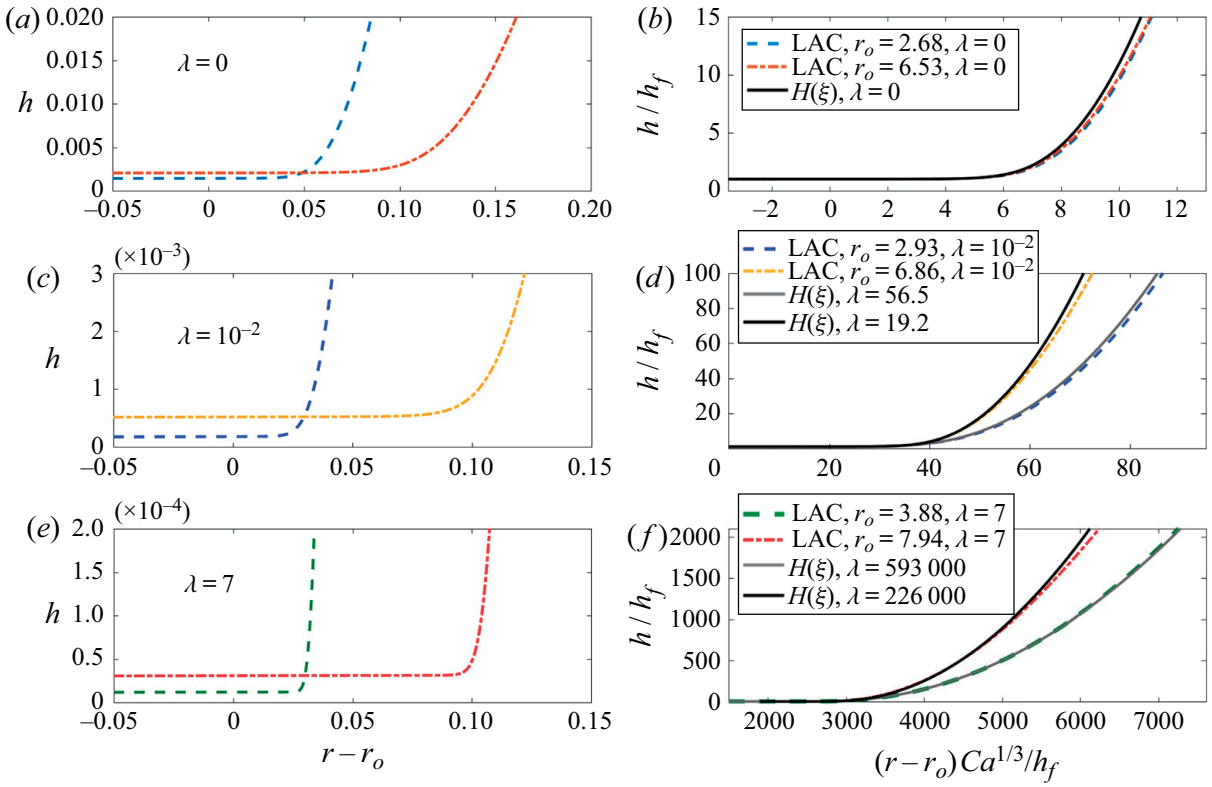

FIGURE 11. (*a*,*c*,*e*) The interfacial profile h as a function of the shifted radial coordinate $r - r_o$ obtained from LAC in the region connecting the flat film and the droplet for different slip lengths λ and droplet positions (characterized by r_r in *b*,*d*,*f*). The parameters are the cone angle $\alpha = 0.01$ rad and the prewetted layer thickness $\epsilon = 0.001$. (*b*,*d*,*f*) The rescaled profiles h/h_f as a function of $(r - r_o)Ca^{1/3}/h_f$. The solid lines are the numerical solution of (3.4) with values of $\bar{\lambda} \equiv \lambda/h_f$ computed by the corresponding values of λ and h_f from the LAC.

where $\bar{\lambda} \equiv \lambda/h_f$. We impose a flat film boundary condition $H(\xi \to -\infty) = 1$, and hence close to the flat film, we can write $H = 1 + \delta \exp[3^{1/3}\xi/(1 + 3\bar{\lambda})^{1/3}]$, with $\delta \ll 1$ (Oron, Davis & Bankoff 1997). The value of δ is arbitrary due to the translational invariance of (3.4). Here, we set $\delta = 5 \times 10^{-7}$ when $\xi = 0$. When $\xi \to \infty$, the profile of the film has to match to the droplet shape at the receding region, thus H tends to ∞, the asymptotic solution of (3.4) is described by $H = a_1\xi + a_2\xi^2$. The value of a_1 and a_2 are determined by the numerical solution of (3.4). A comparison between the similarity profile $H(\xi)$ and the rescaled profiles from LAC in the region connecting the flat film and the droplet is given in figure 11 for three different slip lengths: $\lambda = 0$, 10^{-2} and 7. The profiles from LAC are shifted manually by r_o so that they match the best with the solution of (3.4). The value of r_o is close to r_r (difference within 2 %). Note that for non-zero slip lengths, as h_f varies with droplet positions, $\bar{\lambda}$ has different values at different droplet positions even though λ is the same. We can see in figure 11 that the similarity profiles describe well the profiles from the LAC particularly at the region closer to the flat film. Away from the flat film, the profiles from the LAC bend to match the droplet shape.

In the static droplet region, the profile $h_s(r)$ is determined by the static equation of uniform curvature κ_s obtained by substituting $h_s(r) = h(r)$ into (2.6), with a magnitude of κ_s that depends on the droplet position on the cone. The problem is closed by including the boundary conditions $h_s(r = r_r) = 0$ and $h_s'(r = r_r) = 0$ at the substrate.

Now we are in a position of matching the two asymptotic profiles in the overlapping region. As we already impose the condition $h_s'(r = r_r) = 0$ for the droplet region. A natural

matching condition is equating the second derivatives of the asymptotic profiles. In the film region,

$$h''_{2d}(\xi \to \infty) = 2a_2 Ca^{2/3}/h_f. \tag{3.5}$$

Matching $h''_{2d}(\xi \to \infty)$ to the second derivative $h''_o \equiv h''_s(r = r_r)$ in the static droplet region gives the film thickness

$$h_f = \frac{2a_2(\bar{\lambda})}{h''_o(R_f)} Ca^{2/3}. \tag{3.6}$$

Importantly, as all the cone angles are small, h''_o is independent of α but only a function of the cone radius R_f, which is plotted in figure 10(b) in log scales. Note also that a_2 is determined from (3.4) and a function of $\bar{\lambda} \equiv \lambda/h_f$, which is plotted in figure 10(c). We note that $h''_o = 1/R_f + \kappa_s$, and thus $h''_o \approx 1/R_f$ when $R_f \ll 1$, which is represented by the dashed line in figure 10(b). With the computed values of h''_o and a_2, and using the values of Ca for each droplet position obtained from LAC, we plot h_f/R_f computed from (3.6) in figure 10(a) as square markers. Remarkably, the results from the asymptotic matching agree with the numerical results for all slip lengths. Provided the excellent agreement between the two approaches, we can understand our results in terms of the flow inside the film and the geometry of the droplet, and hence provide a better picture of the physical mechanism of film deposition by a droplet moving on a cone.

We first look at the no-slip case. When $\bar{\lambda} = 0$, $a_2 = 0.669$, which is the same value as obtained from previous studies (Rio & Boulogne 2017). The description of the film region is the same as, for example, the dip-coating cases. Then why is the 2/3 scaling not obtained when plotting h_f/R_f as a function of Ca? One important aspect in our problem is that the droplets have a finite size. Hence, there are two length scales: the cone radius and the droplet radius. In terms of rescaled quantities, this means that the second derivative h''_o is not a linear function of $1/R_f$, except when $R_f \ll 1$, which is already demonstrated in figure 10(b). When we rescale the results of h_f obtained from the LAC by $1/h''_o$ and plot it as a function of Ca in figure 12(a) for three different cone angles. The scaling $Ca^{2/3}$ is recovered and agrees well with the prediction from asymptotic matching especially for smaller cone angles.

Next we look at the slip dependence. From figure 10(c), we see a_2 is independent of $\bar{\lambda}$ when $\bar{\lambda} \ll 1$. Hence for $\lambda \ll h_f$, the film thickness becomes independent of λ. As the typical order of magnitude of h_f for a no-slip case is 10^{-3}, h_f starts to depend on λ significantly when $\lambda > 10^{-3}$. This is consistent with our numerical results. For $\bar{\lambda} \gg 1$, we find that $a_2 = 0.771\bar{\lambda}^{-2/3}$. Substituting this expression of a_2 into (3.6), we obtain

$$h_f = \frac{3.667}{h''^3_o}\left(\frac{Ca}{\lambda}\right)^2. \tag{3.7}$$

This expression is in perfect agreement with our numerical results from the LAC for $\lambda \gg h_f$ in figure 12(b). For droplets moving on a conical fibre, we show already that $Ca \sim \lambda$ when $\lambda \gg 1$, (3.7) then suggests h_f is independent of the slip length as shown in figure 9 for $\lambda \gg 1$.

One may expect that the droplet profile does not maintain a quasi-static shape when the slip length is not small due to significant viscous effects in the entire droplet. However, the excellent agreement between the results from the lubrication equation on a cone and the approach of asymptotic matching suggests that the quasi-static assumption is still valid. The reason might be the large length separation between the deposited film and the droplet height maintaining a very large difference in time scales, as one can observe

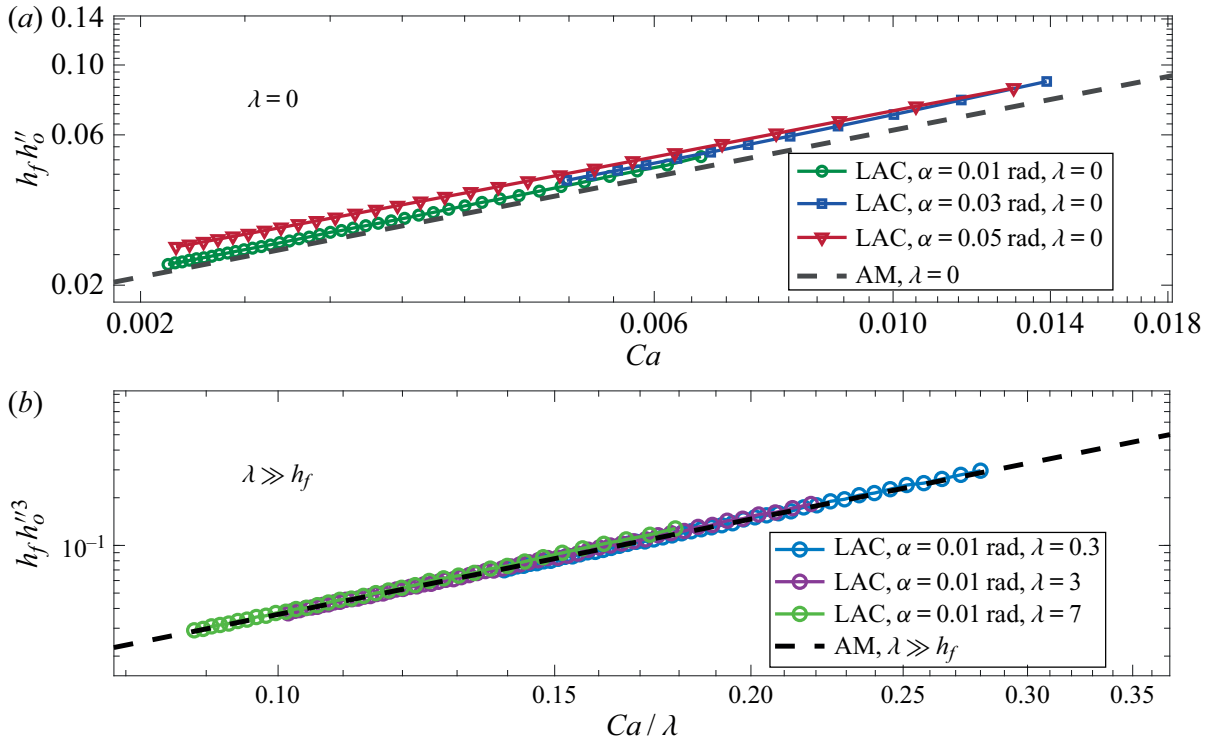

FIGURE 12. (*a*) The film thickness h_f rescaled by $1/h_o''$ as a function of Ca for $\lambda = 0$. Symbols are results from LAC for three different cone angles. The prewetted layer thickness $\epsilon = 10^{-3}$. The dashed line is the result from AM: $h_f h_o'' = 1.34 Ca^{2/3}$. (*b*) The film thickness h_f rescaled by $1/h_o''^3$ as a function of Ca/λ for three different slip lengths $\lambda \gg h_f$. Symbols are results from LAC. The dashed line is the result from AM: $h_f h_o''^3 = 3.667(Ca/\lambda)^2$.

from the mobility term which scales as $\sim \lambda h^2$. Thus there is sufficient time for the droplet to relax to a quasi-static shape when the apparent contact lines move. For the large slip length regime, elongational flow has been proposed to appear and dominate the viscous dissipation (Münch *et al.* 2005), which has been observed for dewetting droplets (McGraw *et al.* 2016; Chan *et al.* 2017). The large slip regime in our model, assuming Poiseuille flow as the dominating flow structure, is considered as the intermediate slip regime in the analysis of Münch *et al.* (2005). For a translating droplet, the effect of elongational flow is unclear, which requires additional experimental and theoretical studies.

For partially wetting surfaces, the droplet dynamics is the same as for the perfectly wetting cases if the prewetted layer is thick enough so that van der Waals forces between the liquid–air and the solid–liquid interfaces can be neglected. A partially wetting droplet moving on a cone without a prewetted layer will also deposit a film if it moves with a velocity above a critical value. The properties of the film are expected to be similar to the wetting cases, namely following the asymptotic relation (3.6), as long as the droplet maintains an axisymmetric shape.

4. Conclusions

The directional spreading of a viscous droplet on a conical fibre due to capillarity is investigated for small cone angles and for a wide range of slip lengths by using the lubrication equation on a cone. The droplet velocity increases with the cone angle and the slip length, but decreases as the cone radius becomes larger. At the receding part of the droplet, a film is deposited on the cone surface while the droplet is moving.

When comparing with our MD simulations, we find that the droplet shapes obtained from these two approaches are the same. The velocity also shows a similar trend. However, no deposited film is observed in the MD simulations, which might be due to the nanoscopic size of the droplet.

The thickness of the deposited film observed in the LAC decreases from $h_f \approx 10^{-3}$ for the no-slip case ($\lambda = 0$) to $h_f \approx 10^{-5}$ for $\lambda > 1$. We show that the film thickness obtained from the lubrication model can be understood by a similar approach of asymptotic matching used in the LLD model. For the no-slip limit, the standard $Ca^{2/3}$ scaling is recovered only when the length scale is given by $1/h_o''$ in the re-scaling. In the limit of $\lambda \gg h_f$, we find another asymptotic regime in which the film thickness scales as $h_f h_o''^3 \sim (Ca/\lambda)^2$. For the problem we study here, the cross-over of these two regimes occurs at $\lambda \approx 10^{-4} - 10^{-1}$. Our results show that manipulating the droplet size, the cone angle and the slip length provides different schemes for guiding droplet motion and coating the substrate with a film.

Acknowledgements

T.S.C. and A.C. gratefully acknowledge financial support from the UiO: Life Science initiative at the University of Oslo. A.C. is grateful for the financial support from the Norwegian Research Council, project number 263056 and 301138. This research was supported by the National Science Foundation under grant no. 1743794, PIRE: Investigation of Multi-Scale, Multi-Phase Phenomena in Complex Fluids for the Energy Industries. We thank Dr K. Dalnoki-Veress and C. Lee for stimulating discussions.

Declaration of interests

The authors report no conflict of interest.

Appendix A. Determination of r_r, r_a, h_f and R_f

Since the liquid–air interface of the droplet is continually connected to the liquid–air interface of the prewetted layer/LLD film, we define the domain of the droplet as follows. We denote the boundaries of the droplet in the receding and the advancing regions respectively as $r = r_r$ and $r = r_a$. We first compute the second derivative of the profile $h''(r)$ at a certain time, which is shown in figures 13(a) and 13(b) respectively in the receding and the advancing regions. The second derivative drops to zero when approaching the film regions. Since h'' is non-negative in the receding region, the droplet boundary $r = r_r$ is defined as the position at which $h''(r)$ drops to below 0.01, i.e. $h''(r = r_r) = 0.01$. In the advancing region, $r = r_a$ is defined as the position at which $h''(r)$ vanishes, i.e. $h''(r = r_a) = 0$. The thickness of the deposited film at that particular time is defined as $h_f(t) = h(r = r_r, t)$ and the corresponding cone radius $R_f(t) = r_r\alpha$. Hence we can link the film thickness h_f to the capillary number Ca at each time.

Appendix B. Dependence on the initial profile

To investigate how the droplet dynamics depends on the initial profile of the droplet, we here compare the dynamics of two droplets with different initial profiles. The initial profiles of the two droplets are described in § 2.2 with different values of A and r_i, see figure 14(a). We compare the capillary number as a function of the droplet position in figure 14(b). We can see after an initial quick relaxation, the later dynamics is independent of the initial profiles.

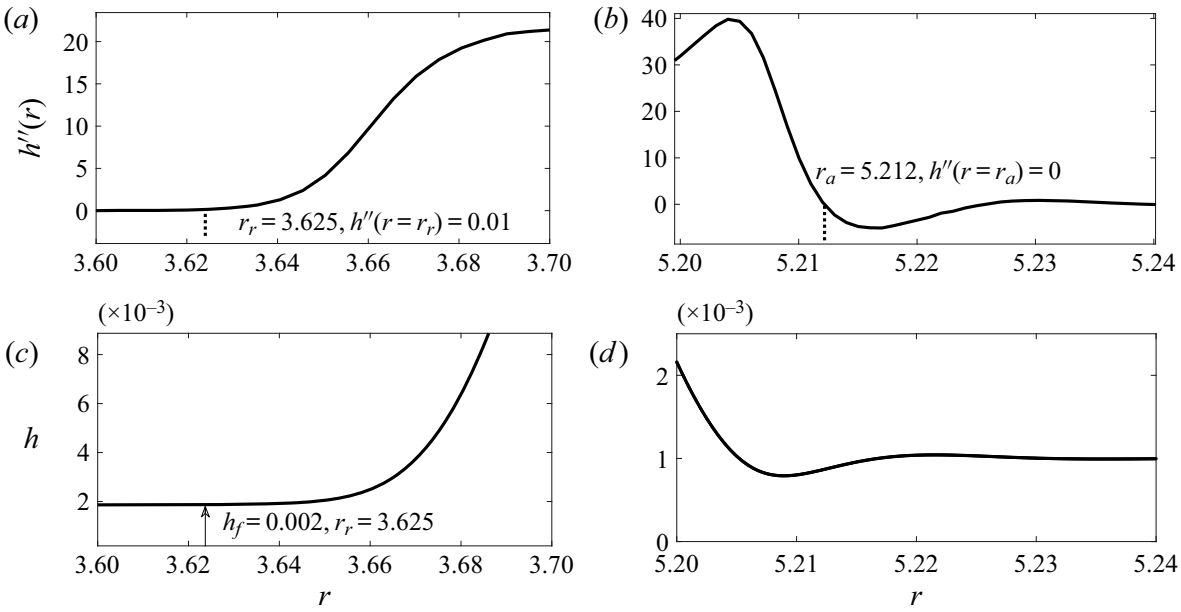

FIGURE 13. (*a*) The second derivative $h''(r)$ of the liquid–air interfacial profile at the receding region of the droplet that connects to the LLD film at $t = 309$. (*b*) The second derivative $h''(r)$ of the liquid–air interfacial profile at the advancing region of the droplet that connects to the prewetted liquid layer at $t = 309$. (*c*) The liquid–air interfacial profile $h(r)$ at the same range of r as (*a*). (*d*) The liquid–air interfacial profile $h(r)$ at the same range of r as (*b*). Parameters: the cone angle $\alpha = 0.01$ rad, the prewetted layer thickness $\epsilon = 10^{-3}$ and the slip length $\lambda = 0$.

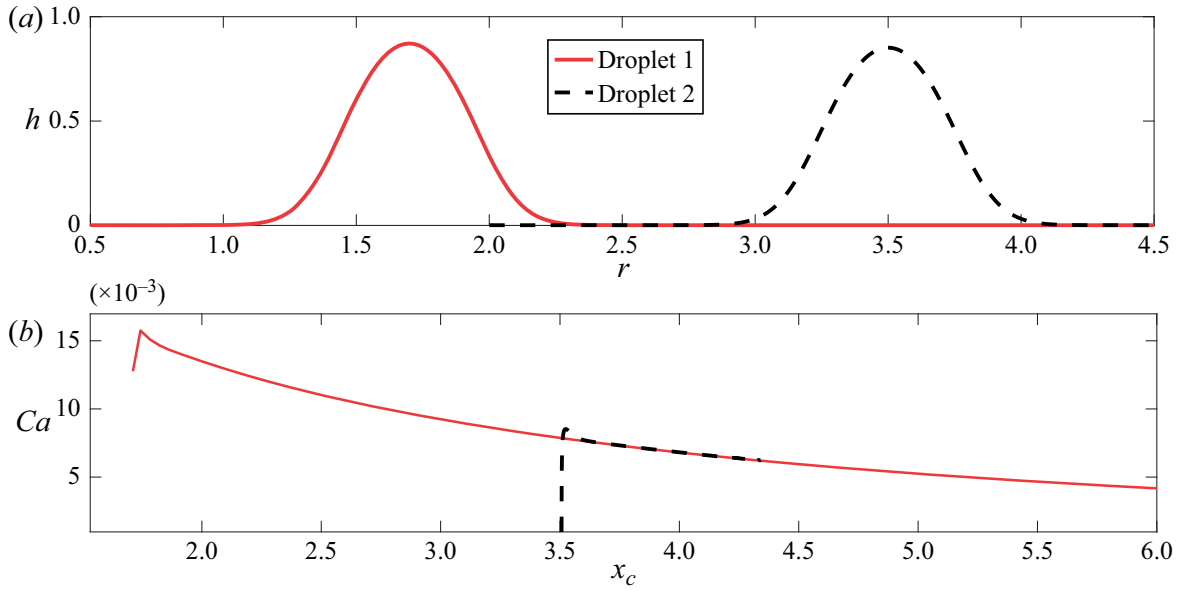

FIGURE 14. (*a*) Two different initial droplet profiles. The droplets profiles are described in § 2.2 with $\epsilon = 10^{-3}$. Droplet 1: $A = 0.87$ and $r_i = 1.7$. Droplet 2: $A = 0.85$ and $r_i = 3.5$. (*b*) The capillary number Ca as a function of the droplet position x_c. Red solid line: droplet 1. Black dashed line: droplet 2. Parameters: $\alpha = 0.01$ rad and $\lambda = 0$.

REFERENCES

BÄUMCHEN, O., FETZER, R. & JACOBS, K. 2009 Reduced interfacial entanglement density affects the boundary conditions of polymer flow. *Phys. Rev. Lett.* **103**, 247801.

BOCQUET, L. & CHARLAIX, E. 2009 Nanofluidics, from bulk to interfaces. *Chem. Soc. Rev.* **39**, 1073.

BONN, D., EGGERS, J., INDEKEU, J., MEUNIER, J. & ROLLEY, E. 2009 Wetting and spreading. *Rev. Mod. Phys.* **81**, 739.

BRETHERTON, F. P. 1961 The motion of long bubbles in tubes. *J. Fluid Mech.* **10**, 166.

BUSIC, B., KOPLIK, J. & BANAVAR, J. R. 2003 Molecular dynamics simulation of liquid bridge extensional flows. *J. Non-Newtonian Fluid Mech.* **109** (1), 51–89.

CARROLL, B. J. & LUCASSEN, J. 1973 Capillarity-controlled entrainment of liquid by a thin cylindrical filament moving through an interface. *Chem. Engng Sci.* **28** (1), 23–30.

CHAN, T. S., MCGRAW, J. D., SALEZ, T., SEEMANN, R. & BRINKMANN, M. 2017 Morphological evolution of microscopic dewetting droplets with slip. *J. Fluid Mech.* **828**, 271–288.

CHAN, T. S., YANG, F. & CARLSON, A. 2020 Directional spreading of a viscous droplet on a conical fibre. *J. Fluid Mech.* **894**, A26.

CHEN, H., RAN, T., GAN, Y., ZHOU, J., ZHANG, Y., ZHANG, L., ZHANG, D. & JIANG, L. 2018 Ultrafast water harvesting and transport in hierarchical microchannels. *Nat. Mater.* **17** (10), 935–942.

CHEN, W., ZHANG, R. & KOPLIK, J. 2014 Velocity slip on curved surfaces. *Phys. Rev.* E **89**, 023005.

COLOSQUI, C. E., MORRIS, J. F. & STONE, H. A. 2013 Hydrodynamically driven colloidal assembly in dip coating. *Phys. Rev. Lett.* **110**, 188302.

DE RYCK, A. & QUÉRÉ, D. 1996 Inertial coating of a fibre. *J. Fluid Mech.* **311**, 219–237.

DERJAGUIN, B. V. 1943 On the thickness of a layer of liquid remaining on the walls of vessels after their emptying, and the theory of the application of photoemulsion after coating on the cine film. *Acta Physicochim. USSR* **20**, 349.

DIXIT, H. N. & HOMSY, G. M. 2013*a* The elastic Landau–Levich problem. *J. Fluid Mech.* **732**, 5–28.

DIXIT, H. N. & HOMSY, G. M. 2013*b* The elastocapillary Landau–Levich problem. *J. Fluid Mech.* **735**, 1–28.

D'ORTONA, U., DE CONINCK, J., KOPLIK, J. & BANAVAR, J. R. 1996 Terraced spreading mechanisms for chain molecules. *Phys. Rev.* E **53**, 562–569.

EGGERS, J. & VILLERMAUX, E. 2008 Physics of liquid jets. *Rep. Prog. Phys.* **71**, 036601.

FETZER, R., JACOBS, K., MÜNCH, A., WAGNER, B. & WITELSKI, T. P. 2005 New slip regimes and the shape of dewetting thin liquid films. *Phys. Rev. Lett.* **95**, 127801.

FRENKEL, D. & SMIT, B. 2002 *Understanding Molecular Simulation*, 2nd edn. Academic Press.

GAO, P., LI, L., FENG, J. J., DING, H. & LU, X.-Y. 2016 Film deposition and transition on a partially wetting plate in dip coating. *J. Fluid Mech.* **791**, 358–383.

GREST, G. S. & KREMER, K. 1986 Molecular dynamics simulation for polymers in the presence of a heat bath. *Phys. Rev.* A **33**, 3628–3631.

GUO, L., CHEN, S. & ROBBINS, M. O. 2016 Slip boundary conditions over curved surfaces. *Phys. Rev.* E **93**, 013105.

HUH, C. & SCRIVEN, L. E. 1971 Hydrodynamic model of steady movement of a solid/liquid/fluid contact line. *J. Colloid Interface Sci.* **35**, 85–101.

JAMES, D. F. 1973 The meniscus on the outside of a small circular cylinder. *J. Fluid Mech.* **63**, 657.

JOHANSSON, P., CARLSON, A. & HESS, B. 2015 Water–substrate physico-chemistry in wetting dynamics. *J. Fluid Mech.* **781**, 695–711.

KIM, O. & NAM, J. 2017 Confinement effects in dip coating. *J. Fluid Mech.* **827**, 1–30.

KOPLIK, J. 2019 Frictional force on sliding drops. *Phys. Rev. Fluids* **4**, 014001.

KOPLIK, J., LO, T. S., RAUSCHER, M. & DIETRICH, S. 2006 Pearling instability of nanoscale fluid flow confined to a chemical channel. *Phys. Fluids* **18** (3), 032104.

KOPLIK, J. & MALDARELLI, C. 2017 Diffusivity and hydrodynamic drag of nanoparticles at a vapor-liquid interface. *Phys. Rev. Fluids* **2**, 024303.

KOPLIK, J. & ZHANG, R. 2013 Nanodrop impact on solid surfaces. *Phys. Fluids* **25** (2), 022003.

KRECHETNIKOV, R. & HOMSY, G. M. 2005 Experimental study of substrate roughness and surfactant effects on the Landau–Levich law. *Phys. Fluids* **17** (10), 102108.

LANDAU, L. D. & LEVICH, B. V. 1942 Dragging of a liquid by a moving plate. *Acta physicochim. USSR* **17**, 42.

LAUGA, E., BRENNER, M. P. & STONE, H. A. 2007 Microfluidics: the no-slip boundary condition. In *Handbook of Experimental Fluid Mechanics*, chap. 19. Springer.

LAUGA, E., BRENNER, M. P. & STONE, H. A. 2008 Microfluidics: the no-slip boundary condition. In *Springer Handbook of Experimental Fluid Mechnaics* (ed. C. Tropea, J. F. Foss & A. Yarin), pp. 1219–1240. Springer.

LI, E. Q. & THORODDSEN, S. T. 2013 The fastest drop climbing on a wet conical fibre. *Phys. Fluids* **25** (5), 052105.

LIU, C., XUE, Y., CHEN, Y. & ZHENG, Y. 2015 Effective directional self-gathering of drops on spine of cactus with splayed capillary arrays. *Sci. Rep.* **5**, 17757.

LOGG, A., MARDAL, K.-A. & WELLS, G. 2012 *Automated Solution of Differential Equations by the Finite Element Method: The FEniCS Book*, vol. 84. Springer Science & Business Media.

LORENCEAU, É. & QUÉRÉ, D. 2004 Drops on a conical wire. *J. Fluid Mech.* **510**, 29–45.

MALEKI, M., REYSSAT, M., RESTAGNO, F., QUÉRÉ, D. & CLANET, C. 2011 Landau–Levich menisci. *J. Colloid Interface Sci.* **354** (1), 359–363.

MCGRAW, J. D., CHAN, T. S., MAURER, S., SALEZ, T., BENZAQUEN, M., RAPHAËL, E., BRINKMANN, M. & JACOBS, K. 2016 Slip-mediated dewetting of polymer microdroplets. *Proc. Natl Acad. Sci. USA* **113** (5), 1168.

MÜNCH, A., WAGNER, B. & WITELSKI, T. P. 2005 Lubrication models with small to large slip lengths. *J. Engng Maths* **53**, 359.

NAKAMURA, Y., CARLSON, A., AMBERG, G. & SHIOMI, J. 2013 Dynamic wetting at the nanoscale. *Phys. Rev.* E **88**, 033010.

ORON, A., DAVIS, S. H. & BANKOFF, S. G. 1997 Long-scale evolution of thin liquid films. *Rev. Mod. Phys.* **69**, 931–980.

ORSINI, G. & TRICOLI, V. 2017 A scaling theory of the free-coating flow on a plate withdrawn from a pool. *Phys. Fluids* **29** (5), 052106.

QIAN, T., WANG, X.-P. & SHENG, P. 2003 Molecular scale contact line hydrodynamics of immiscible flows. *Phys. Rev.* E **68**, 016306.

QUÉRÉ, D. 1999 Fluid coating on a fiber. *Annu Rev. Fluid Mech.* **31**, 347.

QUÉRÉ, D, DI MEGLIO, J.-M. & BROCHARD-WYART, F. 1989 Making van der waals films on fibers. *Europhys. Lett.* **10** (4), 335–340.

QUÉRÉ, D., DI MEGLIO, J.-M. & BROCHARD-WYART, F. 1990 Spreading of liquids on highly curved surfaces. *Science* **249**, 1256–1260.

RIO, E. & BOULOGNE, F. 2017 Withdrawing a solid from a bath: how much liquid is coated? *Adv. Colloid Interface Sci.* **247**, 100–114. Dominique Langevin Festschrift: four decades opening gates in colloid and interface science.

ROTHSTEIN, J. P. 2010 Slip on superhydrophobic surfaces. *Annu. Rev. Fluid Mech.* **42** (1), 89–109.

RUSCHAK, K. J. 1985 Coating flows. *Annu. Rev. Fluid Mech.* **17** (1), 65–89.

SNOEIJER, J. H. & ANDREOTTI, B. 2013 Moving contact lines: scales, regimes, and dynamical transitions. *Annu. Rev. Fluid Mech.* **45**, 269.

SNOEIJER, J. H., DELON, G., FERMIGIER, M. & ANDREOTTI, B. 2006 Avoided critical behavior in dynamically forced wetting. *Phys. Rev. Lett.* **96**, 174504.

SNOEIJER, J. H., ZIEGLER, J., ANDREOTTI, B., FERMIGIER, M. & EGGERS, J. 2008 Thick films coating a plate withdrawn from a bath. *Phys. Rev. Lett.* **100**, 244502.

TABELING, P. & LIBCHABER, A. 1986 Film draining and the Saffman–Taylor problem. *Phys. Rev.* A **33**, 794–796.

TAYLOR, G. I. 1963 Cavitation of a viscous fluid in narrow passages. *J. Fluid Mech.* **16** (4), 595–619.

WANG, Q., YAO, X., LIU, H., QUÉRÉ, D. & JIANG, L. 2015 Self-removal of condensed water on the legs of water striders. *Proc. Natl Acad. Sci.* **112** (30), 9247–9252.

WEINSTEIN, S. J. & RUSCHAK, K. J. 2004 Coating flows. *Annu. Rev. Fluid Mech.* **36**, 29–53.

WHITE, D. A. & TALLMADGE, J. A. 1966 A theory of withdrawal of cylinders from liquid baths. *AIChE J.* **12** (2), 333–339.

WILSON, S. D. R. 1982 The drag-out problem in film coating theory. *J. Engng Maths* **16** (3), 209–221.

WILSON, S. D. R. 1988 Coating flow on to rods and wires. *AIChE J.* **34** (10), 1732–1735.

ZHENG, Y., BAI, H., HUANG, Z., TIAN, X., NIE, F.-Q., ZHAO, Y., ZHAI, J. & JIANG, L. 2010 Directional water collection on wetted spider silk. *Nature* **463**, 640–643.

Paper VI

Film coating by directional droplet spreading on fibers

Tak Shing Chan, Carmen L. Lee, Christian Pedersen, Kari Dalnoki-Veress, Andreas Carlson

Published in Physical Review Fluids 6, 014004 (2021). DOI: https://doi.org/10.1103/PhysRevFluids.6.014004.

Film coating by directional droplet spreading on fibers

Tak Shing Chan,[1,*] Carmen L. Lee,[2,*] Christian Pedersen,[1] Kari Dalnoki-Veress,[2,3] and Andreas Carlson[1,†]

[1]*Department of Mathematics, Mechanics Division, University of Oslo, N-0851 Oslo, Norway*
[2]*Department of Physics and Astronomy, McMaster University, 1280 Main Street West, Hamilton, Ontario, Canada L8S 4M1*
[3]*UMR CNRS Gulliver 7083, ESPCI Paris, PSL Research University, 75005 Paris, France*

(Received 10 August 2020; accepted 15 December 2020; published 20 January 2021)

Plants and insects use slender conical structures to transport and collect small droplets, which are propelled along the conical structures due to capillary action. These droplets can deposit a fluid film during their motion, but despite its importance to many biological systems and industrial applications, the properties of the deposited film are unknown. We characterize the film deposition by developing an asymptotic analysis together with experimental measurements and numerical simulations based on the lubrication equation. We show that the deposited film thickness depends significantly on both the fiber radius and the droplet size, highlighting that the coating is affected by finite-size effects relevant to film deposition on fibers of any slender geometry. We demonstrate that by changing the droplet size, while the mean fiber radius and the capillary number are fixed, the thickness of the deposited film can change by an order of magnitude or more. We show that self-propelled droplets have significant potential to create passively coated structures.

DOI: 10.1103/PhysRevFluids.6.014004

I. INTRODUCTION

Droplets on slender conical substrates will self-propel due to capillary action [1–10] provided the droplets are smaller than the capillary length. This principle is used by insects [11,12] and plants [13–20] for droplet collection. Several studies have focused on mimicking structures found in nature to control liquid movement [21–27]. Recent work [13] has shown that the conically shaped trichomes on the underside of the lid of the *Sarracenia*, a pitcher plant, can transport droplets with a velocity several orders of magnitude larger than that found in other plants. Enhanced water transport is the result of surface lubrication of the trichome. The first droplet that slowly spreads across the trichome deposits a microscopic liquid film, and the following droplets slide along the lubricating film on the trichome. From a technological point of view, understanding the principles of film deposition by capillary-driven motion of droplets can provide pathways for relubrication of slippery liquid infused porous surfaces with conical shapes [6,28] as well as the development of other multifunctional materials. This lubricating film-coating principle has a fundamental role in biological phenomena and has untapped potential as a droplet-driven coating technique, yet the properties of the liquid film are unknown. We study here how droplets deposit lubricating films as they move along slender structures.

*These authors contributed equally to this work.
†acarlson@math.uio.no

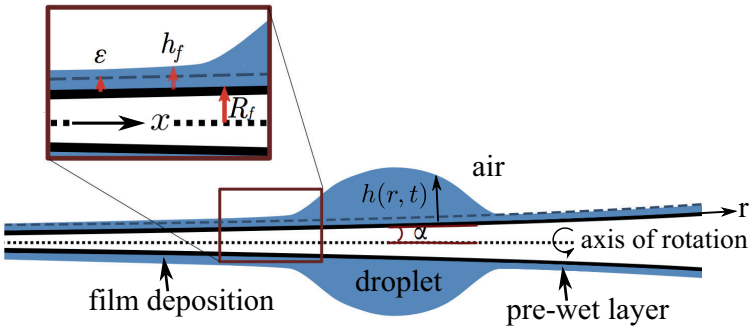

FIG. 1. (a) A sketch of a droplet on a conical fiber with a local cone angle α. Inset: zoom into the region connecting the deposited film of thickness h_f and the receding edge of the droplet at the fiber radius R_f. The fiber is prewet with a layer of the same fluid of thickness ϵ.

Coating a solid substrate with a lubricating liquid film as a way to reduce friction between substrates has been known since ancient Egypt [29]. The broad relevance of coating processes have made them widely studied, with great advances in understanding their underlying physical principles [30–34]. Dip-coating is today one of the most widespread coating techniques [35], where the solid moves with a velocity U relative to the liquid bath. The foundational work of Landau-Levich-Derjaguin (LLD) [36,37] has paved the way for a fundamental understanding of film deposition on solid substrates during wetting. By considering the viscous capillary flow of a liquid with a viscosity μ and a surface tension γ, LLD predicted that the deposited film thickness h_f, normalized by the characteristic length of the system L, is given by $h_f/L \sim \mathrm{Ca}^{2/3}$ [36,37], where the Capillary number $\mathrm{Ca} \equiv \mu U/\gamma$ is the ratio of the viscous and surface tension forces. The LLD theory was developed for $\mathrm{Ca} \ll 1$ and when inertia can be neglected. It is a generic scaling and has proven to be an accurate description of a wide range of coating phenomena, i.e., dip coating of plates [38], cylinders [31,39,40], and Bretherton bubbles [41]. However, a droplet depositing a film on a cylinder has a fundamental difference from film deposition from a liquid reservoir; the droplet size introduces another length scale to the system. The fiber geometry and droplet size are tuneable parameters to control the coating process [1,2].

II. THEORY AND EXPERIMENT

In the system studied here, a droplet deposits a film as it migrates toward the thicker part of a prewet conical fiber, driven by the curvature gradient, as shown schematically in Fig. 1. We investigate the system by combining asymptotic analysis, experiments, and numerical simulations. The assumptions made are that there is viscous flow driven by capillarity ($\mathrm{Ca} \ll 1$). Furthermore, we neglect gravitational effects because the drop size is much smaller than the capillary length, as is clear from the Bond number, which represents the balance between gravity and surface tension, $\mathrm{Bo} = \Delta\rho g V^{2/3}/\gamma \ll 1$, where $\Delta\rho$ is the density difference between the liquid and surrounding air, V is the droplet volume, and g is the gravitational acceleration. As will be seen below, these assumptions are verified by our experiments.

A. Asymptotic analysis

We start off by revising the classical LLD theory for the case of a droplet moving on a cylindrical fiber with radius R by matching asymptotically the quasistatic droplet profile on the fiber $h_s(x)$ and the self-similar deposited film profile (for details, see [4]). By matching the profiles, we show that the film thickness h_f scales with Ca as [4]

$$h_f = 1.338\ell \mathrm{Ca}^{2/3}, \tag{1}$$

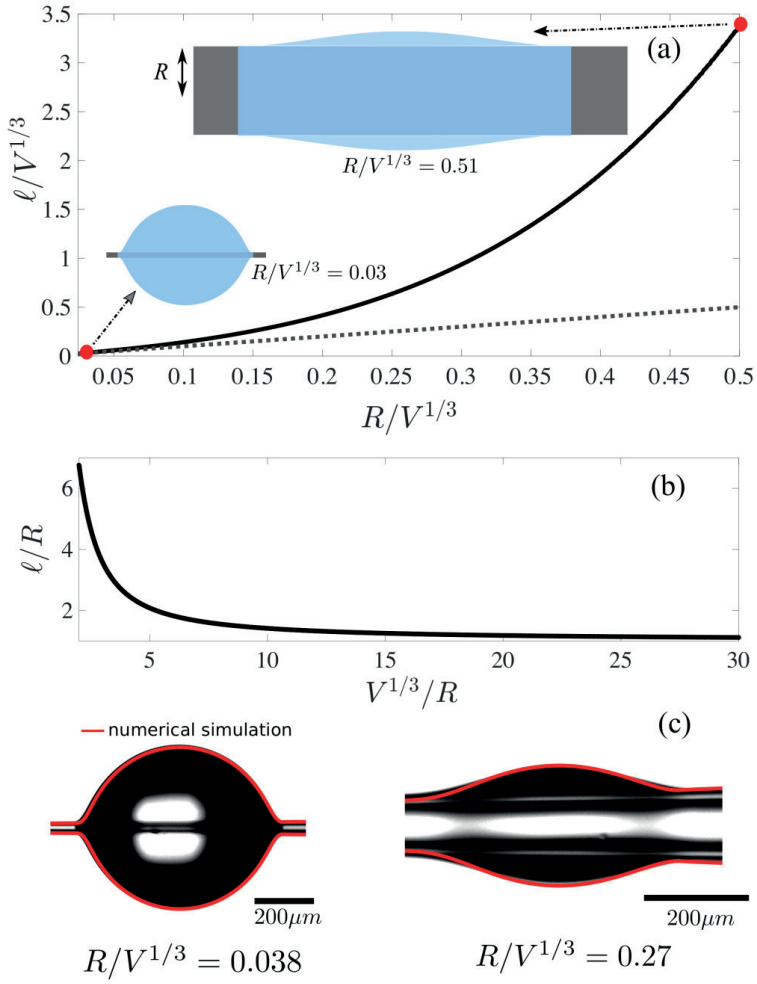

FIG. 2. (a) The dimensionless characteristic length $\ell/V^{1/3}$ as a function of the rescaled radius $R/V^{1/3}$ of a cylindrical fiber (solid line). The dotted line represents the linear relation, i.e., $\ell = R$. Inset: two static droplets of the same volume in contact with a fiber with $R/V^{1/3} = 0.03$ and 0.51 (indicated by the two red dots), which demonstrate different droplet shapes when R varies. The deposited film thickness h_f predicted by our asymptotic analysis scales linearly with ℓ for a given Capillary number Ca (dimensionless droplet velocity); see Eq. (1). From (a) we see that a droplet of a fixed volume coats a thicker film on a thicker fiber. In (b), ℓ rescaled by the fiber radius R is plotted as a function of $V^{1/3}/R$. It shows that for the same fiber radius, a smaller droplet coats a thicker film on the fiber. (c) Sample images of two droplets taken with optical microscopy (top views). Left: $\alpha = 0.43^\circ$ and $R/V^{1/3} = 0.038$, and right: $\alpha = 2.5^\circ$ and $R/V^{1/3} = 0.27$. The numerically calculated profiles from the lubrication theory on a cone [Eq. (2)] are shown in red for matching V, R, and α.

where $\ell \equiv 1/[\partial^2 h_s(x = x_{\rm cl})/\partial x^2]$ is the inverse of the second derivative of the static profile $h_s(x)$ evaluated at the contact line position $x = x_{\rm cl}$, i.e., where the profile $h_s(x)$ meets the solid substrate. A crucial difference from the classical LLD theory is that choosing $\ell = R$ only recovers the correct film thickness in the limit of $R \ll V^{1/3}$. In general, ℓ depends on both the droplet volume V and the fiber radius R, which indicates a finite-size effect. To illustrate this point, we plot $\ell/V^{1/3}$ as a function of $R/V^{1/3}$ in Fig. 2(a). In the limit where $R \ll V^{1/3}$, $\ell = R$, then the film thickness $h_f = 1.338R\,{\rm Ca}^{2/3}$ is independent of the droplet volume. However, when $R/V^{1/3} \gtrsim 0.15$, the droplet size starts to play a significant role in predicting the deposited film thickness that is much larger than if we would naively assume $\ell = R$. Since $\ell/V^{1/3}$ increases with $R/V^{1/3}$ faster than a linear relation, Eq. (1) also implies that a smaller droplet deposits a thicker film for fixed R and Ca. This property is shown in Fig. 2(b), in which ℓ/R decreases with increasing $V^{1/3}/R$. For the directional spreading of droplets

on a conical fiber with a small cone angle α, the influence of α on ℓ only appears as high-order corrections, which are neglected here (see [4] for details). The conical geometry acts as a factor that generates the spontaneous motion of the droplet and plays a role in determining the magnitude of Ca. The theoretical prediction for the film thickness dependence on the droplet size and the fiber radius [see Eq. (1)] can now be compared to experiments and numerical simulations based on the lubrication theory.

B. Experiments

The conical substrates used in the experiments are prepared by pulling standard borosilicate glass capillary tubes in a magnetic micropipette puller (Narishige PN-30). The resulting shape of the capillary tube is a nearly conical fiber with a smoothly varying diameter and gradient, with a smaller cone angle nearing the tip of the fiber. The gradient in the cone angle varies slowly along the fiber, thus on the length scale of the droplet the fibers can be treated as ideal. Droplets of silicone oil with viscosity of $\mu \approx 4.9$ Pa s, and with air-liquid surface tension $\gamma = 22$ mN/m, were deposited at the fiber tip. Silicone oil is ideal because it is totally wetting, chemically stable, nonvolatile, and nonhygroscopic. The fiber is prewet by placing a droplet on the tip of the fiber and allowing it to migrate from one end of the fiber to the other, thereby depositing a film. Prewet film thicknesses were found to range from 0.27 to 13.87 μm, as determined by optical microscopy (OM) using an upright microscope (Olympus BX51) with bottom illumination. OM images of the fiber were taken from above both before and after coating, and they were used to obtain the film thickness. Droplets of volumes V in the range of 0.009–1.99 mm^3, i.e., Bo $\in$ [0.02-0.7], were deposited onto the fiber. Images of the droplet are taken as it migrates along the fiber at a given radius R, and the deposited film is observed as the droplet passes a given location. To ensure the effects of gravity are not affecting the dynamics, a similar experiment was performed in which the entire experimental setup was tilted at different angles to measure if there were any changes in droplet motion in the plane of gravity. There were no discernible differences in droplet motion, and thus the effects of gravity are negligible. The radii of the cone at the measured film thicknesses ranged between 22.26 and 103.92 μm and the deposited film thicknesses were measured in the range of 0.17–19.75 μm.

C. Numerical simulations

To give a mathematical description of the droplet flow on the prewet fiber, we turn to the lubrication approximation for the viscous incompressible flow, when the cone angle $\alpha \ll 1$. The thin-film equation is obtained by reducing the Navier-Stokes equations for flow in films with large lateral dimensions in relation to the thickness [42,43], in combination with mass conservation. A detailed derivation of the lubrication approximation on a conical geometry for $\alpha \ll 1$ is found in [3]. Note that we impose a no-slip condition at the solid substrate and no-shear stress at the free surface. The axisymmetric liquid-air interface profile is given by $h = h(r, t)$, defined as the distance between the interface and the substrate, as a function of the radial distance from the vertex of the cone r and time t. The evolution of the free surface is described by [3,4],

$$\frac{\partial h}{\partial t} + \frac{1}{r\alpha + h}\frac{\partial}{\partial r}\left(M\frac{\partial p}{\partial r}\right) = 0, \tag{2}$$

where the mobility $M = M(h, r, \alpha)$ reads

$$M(h, r, \alpha) = \frac{r^4\alpha^4}{2\mu}\left\{\frac{1}{8}\left[3\left(1 + \frac{h}{r\alpha}\right)^4 - 4\left(1 + \frac{h}{r\alpha}\right)^2 + 1\right] - \frac{1}{2}\left(1 + \frac{h}{r\alpha}\right)^4 \ln\left(1 + \frac{h}{r\alpha}\right)\right\}. \tag{3}$$

The capillary pressure gradient in the liquid generates the flow, and the pressure $p = p(r, t)$ reads

$$p = -\gamma\left\{\frac{\frac{\partial^2 h}{\partial r^2}}{\left[1 + \left(\frac{\partial h}{\partial r}\right)^2\right]^{3/2}} - \frac{1 - \alpha\frac{\partial h}{\partial r}}{(r\alpha + h)\left[1 + \left(\frac{\partial h}{\partial r}\right)^2\right]^{1/2}}\right\}, \tag{4}$$

where the expression is simplified for $\alpha \ll 1$ [3,4]. Equations (2) and (4) are discretized by linear elements and numerically solved with a Newton solver by using the open source finite-element code FEniCS [44]; additional details about the numerical approach are found in [4]. The initial condition is a droplet smoothly connected to a prewet film of thickness ϵ. At the two boundaries ($\delta\Omega$) of the numerical domain, we impose $h(\delta\Omega, t) = \epsilon$ and $p(\delta\Omega, t) = \gamma/R(\delta\Omega)$, where $R(\delta\Omega)$ is the radius of the cone at the boundaries. We note that only the droplet volume V is important, and the initial droplet shape does not affect the results.

III. RESULTS AND DISCUSSION

We start by comparing the droplet spreading dynamics on two cones with $\alpha = 0.43^\circ$ and 2.5°, where the droplet quickly relaxes from its initial condition to its quasistatic shape and then starts to translate to the thicker part of the fiber. When we overlay the experimental measurement with the numerical simulations, as shown in Fig. 2(c), we see that the two results are in close agreement. By zooming into the trailing edge of the droplet, both the experiment and the numerical simulation show the deposition of a film of different thickness from that of the prewet film ϵ.

Next we turn to characterize the thickness of the film during the droplet spreading dynamics on the fiber. To determine the Ca, we extract the droplet velocity U measured at its center of mass. The film is measured on the cone after the droplet has deposited the film, which is stable throughout the observation time in the experiments and the numerical simulations. The Rayleigh-Plateau instability is expected to take place at much longer times as the time scale of the fastest growing mode for a film coated on a cylinder with similar radius is predicted to be more than an order of magnitude longer than both the experimental observation time and the simulation time. Since there is a slight gradient in the cone angle along r in the fiber used in the experiments, we extract the cone angle locally at a given position on the cone with radius $R = R_f$. Here R_f is the cone radius in the receding region, defined based on the droplet profile; see [4]. The deposited film thickness h_f is then a function of α, R_f, V, and ϵ. We combine all the experimental measurements and the numerical predictions of $h_f \in [0.17 - 19.75]$ μm, i.e., for $\alpha \in [0.35 - 2.3]^\circ$, in Fig. 3(a), and they are in good agreement. The film thickness is not uniform along the fiber for a fixed cone angle, but increases with the cone radius R_f. The film thickness h_f increases by roughly one order of magnitude when the cone angle α is varied from 0.35° to 2.3°.

To further compare the theory to the experiments and numerical simulations, we rescale our measurements according to Eq. (1) and also plot the analytical prediction; see Fig. 3(b). Since the motion of the droplet is driven by capillarity, i.e., it is self-propelled, the droplet velocity is a function of the position on the cone. The deposited film thickness h_f rescaled by ℓ obtained from the experiments and the lubrication theory on a cone is shown as a function of Ca in Fig. 3(b). When comparing the results (1) predicted by the asymptotic matching, the experiments, and the numerical simulations, we observe that they are in close agreement, especially for the smallest cone angles. When α increases, there is a slight deviation from $2/3$ scaling observed in the numerical simulations with a slightly larger film thickness than predicted from Eq. (1), likely a consequence of the reduced separation of length scales between the film thickness h_f and the droplet size $V^{1/3}$.

We show that self-propelled droplets have a significant potential to create passively coated structures. By combining an asymptotic analysis, experiments, and numerical simulations of the lubrication equation, we have demonstrated that a droplet that moves on a fiber can deposit a film with a thickness h_f, controlled by the droplet's capillary number and the characteristic length ℓ. The quantity ℓ is a geometric factor that is linear with respect to the fiber radius R when $R/V^{1/3} \ll 1$, i.e., the droplet is much greater in size than the fiber radius. Otherwise, $\ell/V^{1/3}$ increases significantly with $R/V^{1/3}$ when $R/V^{1/3} \gtrsim 0.15$. Our finding has direct implications for control of film deposition during spreading, e.g., if we fix the fiber radius, decreasing the droplet size can increase the thickness of the deposited film by an order of magnitude or more at the same Ca. Coating by droplets introduces novel design features that do not exist in classical coating techniques where the substrate is connected to a liquid reservoir. For a droplet moving on a cylindrical fiber driven

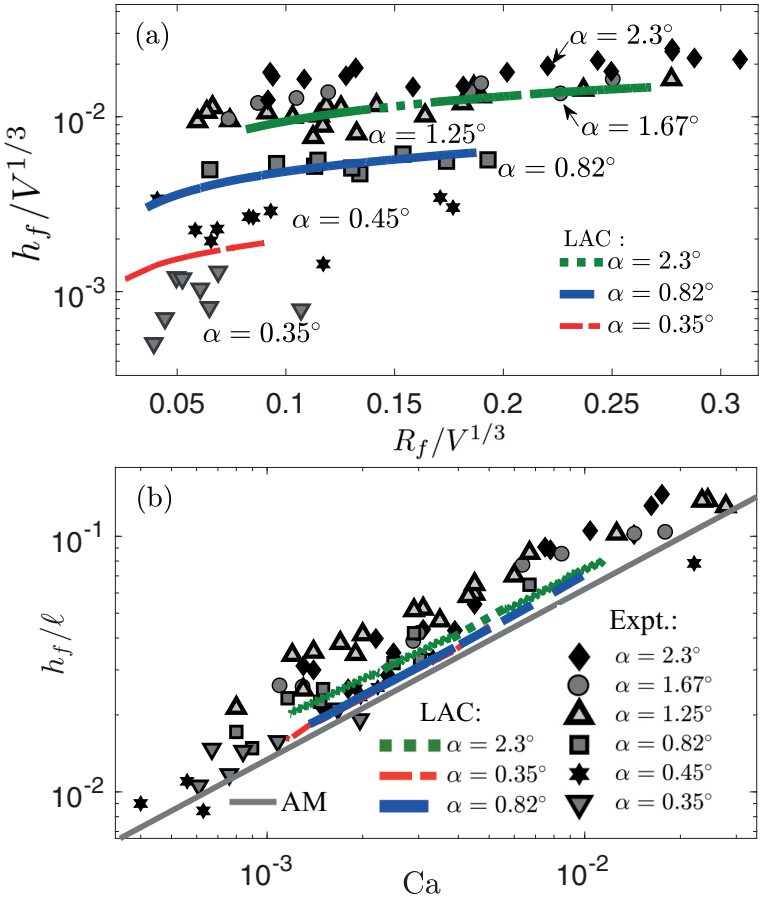

FIG. 3. (a) The deposited film thickness h_f as a function of the cone radius R_f and the cone angle α. Both axes are normalized by $V^{1/3}$. Symbols are experimental data and curves are numerical results from the lubrication theory on a cone (LAC). The prewet layer thickness ϵ in both the experiment and the theory is controlled within a range of 0.27-13.87 μm. (b) The film thickness h_f rescaled by ℓ as a function of the capillary number Ca. The solid line (AM) is the result of asymptotic matching given by Eq. (1).

by external forces, e.g., electric, magnetic, and gravitational, the deposited film thickness follows Eq. (1), whereas Ca depends on the magnitude of the driving force. Our findings are expected to be relevant for any droplet coating application involving a slender geometry, and they may help shed light on why slender conical structures have evolved in a diverse set of biological systems to facilitate efficient droplet transport.

ACKNOWLEDGMENTS

T.S.C. and A.C. gratefully acknowledge financial support from the Research Council of Norway (Project No. 301138) and the UiO:LifeScience initiative at the University of Oslo. C.L.L. and K.D.-V. acknowledge financial support from the Natural Science and Engineering Research Council of Canada.

[1] É. Lorenceau and D. Quéré, Drops on a conical wire, J. Fluid Mech. **510**, 29 (2004).

[2] E. Q. Li and S. T. Thoroddsen, The fastest drop climbing on a wet conical fibre, Phys. Fluids **25**, 052105 (2013).

[3] T. S. Chan, F. Yang, and A. Carlson, Directional spreading of a viscous droplet on a conical fibre, J. Fluid Mech. **894**, A26 (2020).

[4] T. S. Chan, C. Pedersen, J. Koplik, and A. Carlson, Film deposition and dynamics of a self-propelled wetting droplet on a conical fibre, J. Fluid Mech. **907**, A29 (2021).
[5] Y.-E. Liang, H.-K. Tsao, and Y.-J. Sheng, Drops on hydrophilic conical fibers: Gravity effect and coexistent states, Langmuir **31**, 1704 (2015).
[6] J. McCarthy, D. Vella, and A. A. Castrejón-Pita, Dynamics of droplets on cones: Self-propulsion due to curvature gradients, Soft Matter **15**, 9997 (2019).
[7] P. Renvoisé, J. W. M. Bush, M. Prakash, and D. Quéré, Drop propulsion in tapered tubes, Europhys. Lett. **86**, 64003 (2009).
[8] T.-H. Chou, S.-J. Hong, Y.-E. Liang, H.-K. Tsao, and Y.-J. Sheng, Equilibrium phase diagram of drop-on-fiber: Coexistent states and gravity effect, Langmuir **27**, 3685 (2011).
[9] J.-L. Liu, R. Xia, B.-W. Li, and X.-Q. Feng, Directional motion of droplets in a conical tube or on a conical fibre, Chin. Phys. Lett. **24**, 3210 (2007).
[10] X.-F. Wu and Y. A. Dzenis, Droplet on a fiber: Geometrical shape and contact angle, Acta Mech. **185**, 215 (2006).
[11] Y. Zheng, H. Bai, Z. Huang, X. Tian, F.-Q. Nie, Y. Zhao, J. Zhai, and L. Jiang, Directional water collection on wetted spider silk, Nature (London) **463**, 640 (2010).
[12] A. R. Parker and C. R. Lawrence, Water capture by a desert beetle, Nature (London) **414**, 33 (2001).
[13] H. Chen, T. Ran, Y. Gan, J. Zhou, Y. Zhang, L. Zhang, D. Zhang, and L. Jiang, Ultrafast water harvesting and transport in hierarchical microchannels, Nat. Mater. **17**, 935 (2018).
[14] L. Guo and G. H. Tang, Experimental study on directional motion of a single droplet on cactus spines, Int. J. Heat Mass Transf. **84**, 198 (2015).
[15] J. Ju, H. Bai, Y. Zheng, T. Zhao, R. Fang, and L. Jiang, A multi-structural and multi-functional integrated fog collection system in cactus, Nat. Commun. **3**, 1247 (2012).
[16] C. Luo, Theoretical exploration of barrel-shaped drops on cactus spines, Langmuir **31**, 11809 (2015).
[17] Z. Pan, W. G. Pitt, Y. Zhang, N. Wu, Y. Tao, and T. T. Truscott, The upside-down water collection system of syntrichia caninervis, Nat. Plants **2**, 16076 (2016).
[18] F. T. Malik, R. M. Clement, D. T. Gethin, D. Beysens, R. E. Cohen, W. Krawszik, and A. R. Parker, Dew harvesting efficiency of four species of cacti, Bioinspir. Biomim. **10**, 036005 (2015).
[19] M. E. R. Shanahan, On the behavior of dew drops, Langmuir **27**, 14919 (2011).
[20] X. Tan, T. Shi, Z. Tang, B. Sun, L. Du, Z. Peng, and G. Liao, Investigation of fog collection on cactus-inspired structures, J. Bionic Eng. **13**, 364 (2016).
[21] Y. Chen, L. Wang, Y. Xue, L. Jiang, and Y. Zheng, Bioinspired tilt-angle fabricated structure gradient fibers: Micro-drops fast transport in a long distance, Sci. Rep. **3**, 2927 (2013).
[22] H. Bai, X. Tian, Y. Zheng, J. Ju, Y. Zhao, and L. Jiang, Direction controlled driving of tiny water drops on bioinspired artificial spider silks, Adv. Mater. **22**, 5521 (2010).
[23] M. Cao, J. Ju, K. Li, S. Dou, K. Liu, and L. Jiang, Facile and large-scale fabrication of a cactus-inspired continuous fog collector, Adv. Funct. Mater. **24**, 3235 (2014).
[24] X. Heng, M. Xiang, Z. Lu, and C. Luo, Branched zno wire structures for water collection inspired by cacti, ACS Appl. Mater. Interfaces **6**, 8032 (2014).
[25] Y. Hou, L. Gao, S. Feng, Y. Chen, Y. Xue, L. Jiang, and Y. Zheng, Temperature-triggered directional motion of tiny water droplets on bioinspired fibers in humidity, Chem. Commun. **49**, 5253 (2013).
[26] J. Ju, K. Xiao, X. Yao, H. Bai, and L. Jiang, Bioinspired conical copper wire with gradient wettability for continuous and efficient fog collection, Adv. Mater. **25**, 5937 (2013).
[27] T. Xu, Y. Lin, M. Zhang, W. Shi, and Y. Zheng, High-efficiency fog collector: Water unidirectional transport on heterogeneous rough conical wires, ACS Nano **10**, 10681 (2016).
[28] T.-S. Wong, S. H. Kang, S. K. Y. Tang, E. J. Smythe, B. D. Hatton, A. Grinthal, and J. Aizenberg, Bioinspired self-repairing slippery surfaces with pressure-stable omniphobicity, Nature (London) **477**, 443 (2011).
[29] D. Dowson, *History of Tribology*, 2nd ed. (Wiley, London, 1998).
[30] K. J. Ruschak, Coating flows, Annu. Rev. Fluid Mech. **17**, 65 (1985).
[31] D. Quéré, Fluid coating on a fiber, Annu Rev. Fluid Mech. **31**, 347 (1999).
[32] S. J. Weinstein and K. J. Ruschak, Coating flows, Annu. Rev. Fluid Mech. **36**, 29 (2004).

[33] J. H. Snoeijer, J. Ziegler, B. Andreotti, M. Fermigier, and J. Eggers, Thick Films of Viscous Fluid Coating a Plate Withdrawn from a Liquid Reservoir, Phys. Rev. Lett. **100**, 244502 (2008).
[34] E. Rio and F. Boulogne, Withdrawing a solid from a bath: How much liquid is coated? Adv. Colloid Interface Sci. **247**, 100 (2017).
[35] P.-G. de Gennes, F. Brochart-Wyart, and D. Quéré, *Capillarity and Wetting Phenomena: Drops, Bubbles, Pearls, Waves* (Springer, New York, 2003).
[36] L. D. Landau and B. V. Levich, Dragging of a liquid by a moving plate, Acta Phys.-Chim. USSR **17**, 42 (1942).
[37] B. V. Derjaguin, On the thickness of a layer of liquid remaining on the walls of vessels after their emptying, and the theory of the application of photoemulsion after coating on the cine film, Acta Phys.-Chim. USSR **20**, 349 (1943).
[38] M. Maleki, M. Reyssat, F. Restagno, D. Quéré, and C. Clanet, Landau-Levich menisci, J. Colloid Interface Sci. **354**, 359 (2011).
[39] A. De Ryck and D. Quéré, Inertial coating of a fibre, J. Fluid Mech. **311**, 219 (1996).
[40] A. Q. Shen, B. Gleason, G. H. McKinley, and H. A. Stone, Fiber coating with surfactant solutions, Phys. Fluids **14**, 4055 (2002).
[41] F. P. Bretherton, The motion of long bubbles in tubes, J. Fluid Mech. **10**, 166 (1961).
[42] G. K. Batchelor, *An Introduction to Fluid Dynamics* (Cambridge University Press, Cambridge, 1967).
[43] A. Oron, S. H. Davis, and S. G. Bankoff, Long-scale evolution of thin liquid films, Rev. Mod. Phys. **69**, 931 (1997).
[44] A. Logg, K.-A. Mardal, and G. Wells, *Automated Solution of Differential Equations by the Finite Element Method: The FEniCS Book* (Springer Science & Business Media, Berlin, 2012), Vol. 84.